UNIVERSIDADE DE LISBOA
FACULDADE DE CIÊNCIAS
DEPARTAMENTO DE ENGENHARIA GEOGRÁFICA,
GEOFÍSICA E ENERGIA

DYNAMICS AND VARIABILITY OF THE ALONGSHORE FLOWS ON THE NORTHWESTERN IBERIAN MARGIN

Ana Margarida Silva Pereira Teles Machado

Doutoramento em Ciências Geofísicas e da Geoinformação
(Oceanografia)

2014

UNIVERSIDADE DE LISBOA
FACULDADE DE CIÊNCIAS
DEPARTAMENTO DE ENGENHARIA GEOGRÁFICA,
GEOFÍSICA E ENERGIA

DYNAMICS AND VARIABILITY OF THE ALONGSHORE FLOWS ON THE NORTHWESTERN IBERIAN MARGIN

Ana Margarida Silva Pereira Teles Machado

Tese orientada pelo Prof. Doutor Álvaro Peliz e pelo Prof. Doutor James C. McWilliams, especialmente elaborada para obtenção do grau de doutor em Ciências Geofísicas e da Geoinformação, especialidade de Oceanografia.

2014

Acknowledgements

First, I would like to acknowledge my doctoral advisors, Álvaro Peliz and James C. McWilliams, for their scientific advice during the course of this thesis. I would also like to thank Álvaro for all the opportunities given, all that he has taught me, and for his friendship. I would like to thank James McWilliams for welcoming me to his research group at UCLA, and for guiding me in the reading course of his book, which greatly improved my knowledge of GFD.

I would also like to acknowledge my professors in Aveiro: Jesús Dubert, who introduced me to Oceanography; João Dias, for some good advices; and Yamazaki, who introduced me to linux and shell scripting. Thank you to Professora Isabel Ambar, for her encouragement, enthusiasm, and inspiration.

I also want to thank all my friends and colleagues in CO. A special thanks to my colleagues from the satellites room, with whom I shared everyday frustrations and successes of research life; Ana Aguiar, Luisa Lamas, Filipe Neves, Dmitri Boutov. Thank you to Ana Aguiar, for reading this manuscript, and Filipe Neves for the helpful latex tips. Thank you to Sergio Abarca and Celestino Coelho for our memorable GFD discussions. I would also like to thank my colleagues at the Geology Building of UCLA, for receiving me so well during my visit, and Mafalda Mascarenhas for all the administrative support in CO.

Special thanks to my friends in Aveiro, for all the good moments we've shared; Ana Picado, Michele Martins, Canas, Mariana, Miguel Moutinho,

Cátia Almeida, Mariana Costa. I also want to thank Jennifer Noriega for the great weekends in Venice Beach, later in Lisbon, and for the beginning of a good friendship.

This work was supported by the Portuguese Foundation for Science and Technology (FCT) under the grant SFRH/BD/40142/2007 and the projects MedEx(MARINEIRA/MAR/0002/2008) and Sflux(PTDC/MAR/100677/2008).

Quero ainda agradecer a toda a minha família e especificamente ao meu avô Orlando, pelo seu interesse no meu trabalho, e à minha tia Ana Machado, que em tempos me levou imensas vezes à praia e me transmitiu uma grande parte do gosto que tenho pelo mar.

Os principais agradecimentos são para os meus pais e para o meu irmão por sempre me apoiarem e por tudo o mais. E finalmente para o Marco, por nós, por tudo o que partilhamos, e por ser quem mais de perto sofreu as alegrias e frustrações deste percurso que é uma tese.

Abstract

This dissertation focuses on the Northwestern Iberian Margin, its seasonal and interannual variability, the vertical structure of the alongshore currents and the characteristics of the mesoscale field. These topics were explored by analyzing a 20-year simulation of the Regional Ocean Modeling System (ROMS) at 2.3 km resolution, forced by a 27 km resolution Weather Research and Forecast (WRF) winds (downscaled from Era-Interim reanalysis) covering the whole Western Iberian Margin. The model includes an explicit representation of the inflow/outflow at the Strait of Gibraltar in a nested grid system, and the climatological inflow of the main rivers. The model results are compared with various data. We show that currents over the slope are divided in three different cores: the Iberian Poleward Current (IPC), occupying the top 250 m, a deeper core at Mediterranean Water levels and in between the two, an equatorward core centered beneath the IPC core. The IPC is present almost yearlong, including in summer months, when it is close to the shelf-break and capped by the equatorward upwelling jet. After September, the IPC intensifies and its core surfaces. The main forcing mechanism of the IPC is the "Joint Effect of Baroclinicity and Relief" (JEBAR), but there is an important contribution from southerly winds in December and January, when the current is stronger and surface intensified. Regarding the interannual variability, we verified that the intensity of the IPC depends on the intensity of the southerly winds, from October to January. In September the intensity of the poleward flows depend on the larger scale wind stress curl, which changes JEBAR. We also show that the IPC transport has a strong variability at the synoptic scales, most of it forced by the wind. Short periods of relaxation of southerly winds are usually followed by the destabilization of the IPC and the origin of various anticyclones along the slope.

Keywords: Iberian Poleward Current, Seasonal Variability, Interannual Variability, Swoddies, Ocean Modeling

Resumo

A margem ocidental da Península Ibérica é uma região de grande interesse do ponto de vista oceanográfico devido à variedade de processos que a caracterizam e que acontecem a diferentes escalas espaciais e temporais. Na literatura esta região é particularmente conhecida por se situar no limite norte do sistema de afloramento das Canárias e por ser a região onde a Água Mediterrânica se difunde pelo Oceano Atlântico.

Neste trabalho procurou-se contribuir para o conhecimento da circulação desta região, essencialmente através do desenvolvimento e análise de uma simulação numérica do oceano, de 20 anos, que cobre o período de 1989 a 2008. A simulação foi efectuada utilizando o modelo ROMS (Regional Ocean Modeling System) (Shchepetkin and McWilliams, 2005; Shchepetkin and McWilliams, 2003; Hedstrom, 2009), com uma resolução de 2.3 km e forçado por uma atmosfera que é uma saída do modelo atmosférico WRF, com 27 km de resolução e para o mesmo período. O modelo resolve explicitamente as trocas no Estreito de Gibraltar e inclui uma climatologia das descargas fluviais dos principais rios da região. A simulação abrange toda a Margem Ibérica Ocidental. Os resultados do modelo foram comparados com dados de temperatura da superfície do oceano e de altimetria obtidos por satélite, com uma compilação de dados de amarrações de correntómetros disponíveis para a região em estudo, e com dados de boias oceanográficas.

Assim como outras zonas limítrofes dos sistemas de afloramento, a margem ocidental da Península Ibérica apresenta uma variabilidade sazonal. O Anticiclone dos Açores é mais intenso no Verão e geralmente encontra-se posicionado mais para Norte, o que juntamente com uma depressão térmica que se desenvolve sobre a Península Ibérica, resulta na persistência de ventos de norte, ao longo da margem ocidental. Os ventos de norte são favoráveis à ocorrência de afloramento costeiro e em resposta a circulação é caracterizada

por correntes para sul sobre a plataforma, água mais fria junto à costa e presença de filamentos numa fase mais avançada do verão (Haynes et al., 1993; Relvas and Barton, 2002; Peliz et al., 2002). No Inverno, o Anticiclone dos Açores é geralmente menos intenso e a sua localização média situa-se mais a Sul, permitindo a passagem de vários centros de baixas pressões sobre a margem Ocidental Ibérica. Desta forma, os ventos no Inverno apresentam uma maior variabilidade à escala sinóptica, com ventos predominantes de Sul em Dezembro e Janeiro. A circulação no Inverno é dominada pela presença de uma corrente para Norte, denominada de Corrente Ibérica para o Pólo (IPC de "Iberian Poleward Current"), localizada sobre o topo da vertente e a plataforma e que transporta águas quentes e mais salgadas para Norte. Esta corrente foi descrita em vários estudos (Frouin et al., 1990; Pingree and Le Cann, 1990, 1992b; Martins et al., 2002; Peliz et al., 2005; Torres and Barton, 2006; Le Cann and Serpette, 2009). Em níveis mais profundos, a Água Mediterrânica também circula para Norte, sobre a vertente (Daniault et al., 1994). Apesar da existência de vários estudos sobre a circulação de Verão e de Inverno nesta região, ainda não é conhecido o seu ciclo sazonal, especialmente naquilo que diz respeito aos processos de transição entre Verão e Inverno e vice-versa. Um dos objectivos desta tese é fazer essa descrição.

No que diz respeito aos processos físicos que controlam a IPC, foi explorada em diferentes trabalhos a forma como um gradiente meridional de densidade (que está presente ao largo da Margem continental) interage com a vertente (um gradiente zonal de profundidade acentuado), induzindo a formação de uma corrente para norte sobre o topo da vertente, com características semelhantes à IPC (Dubert, 1998; Peliz et al., 2003b). Outros estudos também referem a importância de episódios de vento de sul, associados a eventos em que uma corrente superficial para norte é particularmente intensa (Le Cann and Serpette, 2009). Para compreender a importância relativa destes dois processos (vento e estrutura interna da densidade) é realizada uma análise da variação sazonal dos balanços de vorticidade sobre a vertente.

A IPC apresenta uma grande variabilidade inter-anual, como foi demons-

trado por vários estudos que a analisaram com base na temperatura da superfície do oceano obtida por satélite (Garcia-Soto et al., 2002; Peliz et al., 2005; Le Cann and Serpette, 2009; Garcia-Soto and Pingree, 2011). Neste trabalho é feita uma descrição da variação inter-anual da intensidade da IPC e dos seus efeitos nos campos de temperatura e salinidade. São também analisados os vários mecanismos que podem controlar a variabilidade inter-anual.

Na bibliografia são descritos vários episódios de formação de turbilhões, resultantes da destabilização da IPC. Estes vórtices têm polaridade anticiclónica e contêm no seu núcleo águas mais quentes e de maior salinidade do que as águas circundantes. Estes anticiclones, foram observados pela primeira vez na costa Norte da Península Ibérica por Pingree and Le Cann (1992b), que os denominaram de "Swoddies" – "Slope Water Oceanic Eddies". Estruturas semelhantes a estas também foram observadas na costa Oeste (Fiúza et al., 1998; Oliveira et al., 2004; Peliz et al., 2003b, 2005). Dubert (1998) and Peliz et al. (2003b) estudaram a formação de Swoddies em simulações numéricas idealizadas e demonstraram que a topografia tem um papel importante para o desenvolvimento das instabilidades que dão origem aos vórtices, e que estes geralmente se formam a seguir aos principais acidentes topográficos. Neste trabalho procurou-se perceber as suas condições de formação, bem como fazer uma estatística das características da sua população.

Os resultados confirmaram que a corrente sobre a vertente é composta por 3 estruturas distintas: a IPC ocupa os 250 m superficiais; as profundidades de ∼600-1200 m são ocupadas por uma corrente mais profunda também para norte, aos níveis da Água Mediterrânica; e entre as duas, sob o centro da IPC, desenvolve-se uma contra-corrente para sul. Verificou-se que a IPC está presente durante praticamente todo o ano, incluindo nos meses de Verão. No Verão a IPC é sub-superficial e o seu máximo de intensidade localiza-se junto ao bordo da plataforma, debaixo do jacto de afloramento que ocupa a região da plataforma. A partir de Setembro, a IPC intensifica-se e torna-se máxima à superfície.

Foi realizada uma análise dos balanços de vorticidade sobre a vertente,

a partir da qual se concluiu que o mecanismo forçador da IPC mais importante é o JEBAR (de "Joint Effect of Baroclinicity and Relief" ou "Efeito Conjunto de Baroclinicidade e Topografia"), associado à presença de gradientes meridionais de densidade. A IPC tem uma forte componente advectiva e transporta águas menos densas para norte, caracterizadas por temperaturas e salinidades mais elevadas, diminuindo os gradientes meridionais de densidade sobre a vertente, e desta forma, diminuindo a intensidade do JEBAR e a sua importância enquanto processo que acelera a corrente. Verificou-se que também existe uma contribuição importante dos ventos de sul, principalmente em Dezembro e em Janeiro, quando a corrente está mais intensa e intensificada junto à superfície.

O modelo reproduz os anos anómalos da IPC em fase com a realidade. Os resultados demonstraram que entre Outubro e Janeiro existe uma relação linear entre médias mensais da intensidade da IPC e as médias mensais da intensidade de ventos de sul. Em Setembro, a intensidade da corrente depende do campo do rotacional do vento sobre uma região maior, que ao alterar a estrutura do campo de densidades e o gradiente meridional de densidade, altera o valor do JEBAR que é o principal factor que controla a IPC em Setembro. Verificou-se também que em geral, quanto mais forte a corrente, mais intensas são as anomalias de temperatura e salinidade obtidas. No entanto, os fluxos de calor locais e os balanços de precipitação/evaporação, também são importantes, especialmente em alguns anos anómalos.

Por fim é demonstrado que a IPC tem uma forte variabilidade à escala sinóptica, maior parte da qual é forçada pela variabilidade do vento. A IPC destabiliza-se, principalmente, perto de variações topográficas acentuadas, dando origem à formação de anticiclones denominados de Swoddies. Estes formam-se constantemente, mas é em períodos de relaxamento de vento de sul que se verificam as maiores taxas de formação. Após o relaxamento dos ventos, a corrente apresenta sinais de instabilidades, que posteriormente crescem e dão origem aos anticiclones. Os Swoddies interagem com outros vórtices, particularmente com ciclones intensificados em profundidade, e a

interacção resulta numa propagação para o largo, e no transporte de águas mais quentes e mais salgadas da IPC para o oceano aberto.
Palavras-chave: Corrente Ibérica para o Pólo, Ciclo Sazonal, Variabilidade Inter-Anual, Turbilhões, Modelo Oceânico, Swoddies

Contents

List of Acronyms and Abbreviations

COADS Comprehensive Ocean-Atmosphere Data Set

CTD Conductivity, Temperature, and Depth sonde

EKE Eddy Kinetic Energy

ENACW Eastern North Atlantic Central Water

ENACWst Eastern North Atlantic Central Water of Sub-Tropical origin

GFD Geophysical Fluid Dynamics

GHRSST Group for High Resolution Sea Surface Temperature

IPC Iberian Poleward Current

IPSU Iberian Poleward Slope Undercurrent

JEBAR Joint Effect of Baroclinicity and Relief

Meddies Mediterranean Water eddies

NAO North Atlantic Oscilation

RMSe Root Mean Square Error

ROMS Regional Ocean Modeling System

SLA Sea Level Anomaly

SSH Sea Surface Height

$SSHa$ Sea Surface Height anomaly

SST Sea Surface Temperature

$Swoddies$ Slope Water Oceanic eDDIES

$USCC$ Upper Slope Countercurrent

WRF Weather Research and Forecast Model

WSC Wind Stress Curl

List of Figures

Introduction

The Western Iberian Margin is very interesting for the variety and complexity of the processes that take part simultaneously, at different temporal and spatial scales. It is famous for two main reasons. In one hand it is the northernmost limit of the Canary Upwelling System, and, on the other hand, it is the place where the Mediterranean Water overflows into the Atlantic. Near the surface, during the summer period, the circulation is upwelling-type, characterized by equatorward shelf flows, cold water fronts and filaments (Haynes et al., 1993; Relvas and Barton, 2002; Peliz et al., 2002). This happens because the Azores High Pressure Cell is stronger and displaced northwards in summer, resulting in persistent northerly and upwelling favorable winds. In winter, the Azores High Pressure Cell weakens and moves southwards, allowing the passage of various winter atmospheric cyclones over the Western Iberian Margin. This results in a more variable wind, predominantly southerly in December and January. The ocean circulation in the winter is dominated by the Iberian Poleward Current (IPC), flowing over the upper slope and outer shelf of the Western Iberian Margin and extending all along to the northern coast of the Iberian Peninsula. This current was described in various studies (Frouin et al., 1990; Pingree and Le Cann, 1990, 1992b; Martins et al., 2002; Peliz et al., 2005; Torres and Barton, 2006; Le Cann and Serpette, 2009).

Dubert (1998) and Peliz et al. (2003b), amongst others, showed that the presence of a meridional density gradient interacting with the slope, as happens in the Western Iberian Basin, can give origin to a surface intensified

poleward current over the slope, with similar characteristics to the observed IPC. Other authors believe southerly winds are also important for the development of surface intensified events of the IPC (Le Cann and Serpette, 2009).

Analysis of satellite SST data suggest that the IPC is subjected to a strong interannual variability. Various studies focused on these year-to-year changes in winter SST anomalies to infer about the interannual variability of the current (Garcia-Soto et al., 2002; Peliz et al., 2005; Le Cann and Serpette, 2009; Garcia-Soto and Pingree, 2011). However, it is not clear what forces the year-to-year variability of the IPC intensity and its response in terms of temperature and salinity anomalies.

The IPC is known to destabilize, and give origin to anticyclonic eddies that carry the warmer and saltier water offshore. These eddies were first identified on the northern coast by Pingree LeCann 1992a, who named them by 'Slope Water Oceanic eDDIES' (Swoddies). They were also observed on the western coast (Fiúza et al., 1998; Oliveira et al., 2004; Peliz et al., 2003b, 2005). Dubert (1998) and Peliz et al. (2003b) studied their formation using idealized model simulations, and showed that topography is important for the formation of the eddies, with their places of formation being usually located downstream of topographic accidents.

Despite the existence of many observational and modeling studies of this region, there are still many unanswered questions regarding the seasonal cycle of the IPC, its interannual variability, and its destabilization and formation of eddies. An extended introduction to each of these problems is included in the beginning of each chapter. We developed a regional ocean simulation, focusing on the period from 1989 to 2008, and used it together with the available in-situ and satellite observations, to study this region with further detail and address some of the open questions.

This thesis is organized as follows:

In Chapter 1, is presented a description of the model, of the simulations and an introduction to the various datasets used. Comparisons between the

model and observations are presented.

Chapter 2 provides a characterization of the vertical structure of the mean alongshore flow and its mean seasonal variability.

In Chapter 3, the main mechanisms forcing the IPC are investigated, and their seasonal variability is analyzed.

In Chapter 4, the interannual variability of the IPC is described, and the mechanisms driving its variability are investigated.

Chapter 5 presents a study of the formation of anticyclonic eddies (Swoddies) associated with the destabilization of the IPC. It makes a characterization of their population and analyses some events of formation.

Finally, a summary of main conclusions is presented along with newly raised questions.

Chapter 1

Model Configuration and Observed Data

1.1 Model configuration

1.1.1 Model

The Regional Ocean Modeling System (ROMS), is a primitive equation, hydrostatic, sigma coordinate, free-surface ocean model (Shchepetkin and McWilliams, 2005; Shchepetkin and McWilliams, 2003; Hedstrom, 2009). The need for solving processes at a wide range of horizontal spatial scales led us to choose the ROMS-AGRIF version ($http://www.romsagrif.org/$), because of its nesting capabilities [Penven et al. (2006) and Debreu et al. (2012)].

ROMS uses a third-order upstream momentum and tracers advection scheme, which is dissipative in nature, allowing a simulation without explicit viscosity or diffusivity. The subgrid-scale vertical mixing processes in the interior and in the boundary layers are parametrized with a K-profile parametrization scheme (Large et al., 1994).

This model configuration was developed in two phases. The first, was a large scale climatological simulation using the large domain represented in

Fig. 1.1 (grid C0), to produce equilibrium solutions for initialization and boundary conditions. The second phase consists of a high resolution 2-way nested realistic simulation (domains represented in Fig. 1.1 – grids A0 and A1), initialized and forced on the boundaries by the outputs of the climatological run.

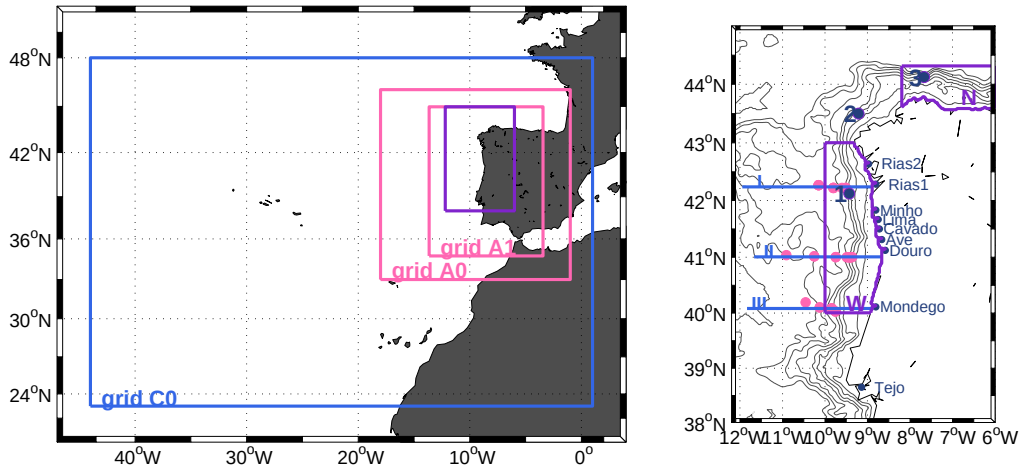

Figure 1.1: *On the left: Map showing the 3 spatial domains used in the model configuration (Grids C0, A0 and A1). On the right: a zoom on the coastal margin we are focusing on. The name of the rivers considered in the simulation are indicated. (1-3) blue dots represent the position of 3 moored buoys located at 9.43W 42.12N, 9.21W 43.50N and 7.67W 44.12N; (N,W) purple boxes represent 2 domains, on northern and western coasts; the pink dots represent the current meter observations; the black contours represent the isobaths of 100, 200, 500, 1000, 2000, 3000, 4000 and 5000 m.*

1.1.2 Climatological Simulation

For the domain C0, we made a 10 years simulation, with horizontal grid resolution of $1/10°$, which corresponds to approximately 7.5 km near the northern boundary and 10 km in the south. This results in an horizontal grid with 449x311 cells. In the vertical direction, the grid has 32 levels with enhanced resolution near the surface (the surface stretching parameter is $\theta_S = 6$ and

the bottom stretching parameter $\theta_B = 0$) to better resolve the boundary layer everywhere in the domain. The baroclinic time step is 1080 seconds. The model grid, forcing, initial and climatology files were built using the ROMSTOOLS package (Penven et al., 2008). The topography was derived from database ETOPO2 (National Geophysical Data Center – NDGC), smoothed and interpolated to the model grid. The model was initialized with Levitus climatology (WOA05 – Locarnini et al. (2006) and Antonov et al. (2006)) in January. Along the open boundaries it was used a modified radiation boundary condition together with a flow adaptive nudging to the Levitus climatology (Marchesiello et al., 2001; Locarnini et al., 2006; Antonov et al., 2006). The nudging is stronger in case of inflow in the open boundaries and weaker in case of outflow, respectively with time scales of 1 day and 1 year for tracers, and 10 days and 1 year for momentum. Regarding the external forcing, the momentum, heat and freshwater fluxes were extracted from the Comprehensive Ocean-Atmosphere Data Set (COADS) monthly climatology at $1/2°$ resolution (da Silva et al., 1994). The Mediterranean Water is forced in the model using a nudging term that prevents the divergence of the model solution from the Levitus climatology. The nudging condition implemented is described in Peliz et al. (2007). After a spin-up of around 2 years, the volume averaged kinetic energy of the simulation reaches an equilibrium (not shown). Years 4 to 7 of this simulation were used to create a monthly climatology for the high resolution domains A0 and A1 (see Fig. 1.1).

1.1.3 Two-way nesting simulation

This simulation uses a larger domain (represented as A0 in Fig. 1.1) and an embedded child domain (represented as A1 in Fig. 1.1), running simultaneously and exchanging information between each other at every model time-step. A0 spans from 33°N to 46°N and 18°W to 1°W, with an horizontal resolution within the range of 6.4 to 7.8 km (205x205 grid cells). A1 spans from 34.8°N to 45.0°N and 13.6°W to 3.4°W, with horizontal resolution from 2.2 to 2.5 km (368x482 grid cells). In the vertical, the grids have

40 levels with enhanced resolution near the surface ($\theta_S = 6$ and $\theta_B = 0$) to better resolve the boundary layer everywhere in the domain. The baroclinic time steps are 900 seconds and 300 seconds for grids A0 and A1, respectively. The model grids were also built using the ROMSTOOLS package (Penven et al., 2008). The topography was derived from Scripps Institution for Oceanography global topography (Smith and Sandwell, 1997) and from Spanish data for the Strait of Gibraltar (Sanz et al., 1991). The merged topography was smoothed to avoid pressure gradient errors, so that the slope parameter (Beckmann and Haidvogel, 1993) is everywhere lower than 0.19.

Radiation condition plus flow adaptive nudging towards a monthly climatology, were used along A0 open boundaries (Marchesiello et al., 2001). The monthly climatology was created from the outputs of the climatological simulation. No interannual variability is introduced to the domain from the open ocean, through the open boundaries.

Null viscosity and diffusivity were used everywhere, except in a sponge layer of 15 km width along the open boundaries of domain A0 (see Fig. 1.1). Increased values of viscosity and diffusivity were applied in the Gulf of Cadiz near the Strait of Gibraltar to produce a more realistic representation of the Mediterranean Undercurrent (Peliz et al., 2012) and near the mouth of river inputs, to represent more realistic water mass characteristics of the river plumes. In the sponge layer, the viscosity increases smoothly from zero in the interior to 300 m^2s^{-1} in the boundary.

1.1.4 Atmospheric Forcing

The atmospheric forcing was created using the outputs of a Weather Research and Forecast (WRF) model simulation, covering the period from 1989 to 2008 with hourly outputs and with horizontal resolution of 27 km (Soares et al., 2012). The variables used were the wind at 10 m, the temperature and the specific humidity at 2 m, the precipitation, the short wave net radiation and incident long wave radiation. The fluxes of momentum and sensible and latent heat, are computed internally in the ocean model at each time step,

using a bulk formulation [Fairall et al. (1996) and Liu et al. (1979)]. The upward long wave radiation is also computed internally in the model, using the Stefan-Boltzmann law with the computed sea surface temperature (SST).

1.1.5 Rivers and Mediterranean Outflow

The rivers that discharge a significant amount of fresh water to the coastal ocean are Tejo, Mondego, Douro, Ave, Cávado, Lima, Minho, together with smaller ones that discharge into the Galician Rias (Tambre, Ulla, Umia, Lérez and Verdugo) (subplot on the right in Fig. 1.1) and Guadalquivir. Due to recurrent and extensive gaps in river outflow data, we used climatologies of river discharges based on the adjusted seasonal cycle. We used the analytical adjustments to simulate the runoff in the model. For the northwestern Iberian rivers we used data from Otero et al. (2010) (Douro River was the southernmost one considered in this study). Runoff data for Mondego and Tejo Rivers were obtained from Chainho et al. (2006) and Neves (2010), respectively. Guadalquivir is not shown in Fig. 1.1 because it is out of the zoom area represented on the plot on the right, but it was considered in the simulation and introduced the same way as in Peliz et al. (2012).

To get realistic values for the salinity of the river plumes it was necessary to increase mixing near the river mouths. In nature, many of these rivers discharge in estuaries where the fresh water is strongly mixed with sea water, due to tide effects, strong currents and atmospheric heat forcing. All of these processes increase the mixing of the river plumes with the coastal ocean, modifying the salinity and density of the plumes. Because of their reduced size, the estuaries are not resolved with the horizontal resolutions used in this simulation. To represent the unresolved mixing processes, we used a constant velocity profile for the outflow of the rivers, instead of the exponential one (with velocity increasing to the surface). Using this type of profile, freshwater is introduced near the bottom, forcing vertical convection and consequently vertical mixing. We also introduced a circular region with increased horizontal diffusion near the mouth of all the rivers, whose radius

and intensity vary in time, proportionally to the intensity of the river outflow.

To guarantee a realistic Mediterranean outflow, we used the same procedure as in Peliz et al. (2012).

1.1.6 Spin-up

A spin-up of 2 years was done, already taking in consideration the rivers and mediterranean outflow as described. The atmospheric forcing, momentum, heat and freshwater fluxes were from the Comprehensive Ocean-Atmosphere Data Set (COADS).

After the spin-up, the model ran for 20 years, 1989 to 2008, which is the period analyzed in this paper.

1.2 Observed data

We compare the model results with currents, temperature and salinity time-series measured at 3m depth, at the buoys of the Spanish Public Agency of Marine Affairs, Puertos del Estado (`http://www.puertos.es/en`). Figure 1.1 shows the positions of the buoys Villano Sisargas, Estaca Bares and Cabo Silleiro, represented respectively as 1, 2 and 3.

We also used altimeter products, produced by Ssalto/*Duacs* and distributed by *Aviso*, with support from *Cnes* (`http://www.aviso.oceanobs.com/duacs/`). The maps have a spatial resolution around 28 km and a time resolution of one week.

To compare with the model sea surface temperature (SST), we used satellite AVHRR Pathfinder Version 5.2 (PFV5.2) data, obtained from the US National Oceanographic Data Center and GHRSST (`http://pathfinder.nodc.noaa.gov`) (Casey et al., 2010).

We also used data from a set of historical moored current meter data from 1984 to 1995. The data were collected in the frame of different projects (CORPAC, MORENA, Bord-Est1 and MEDPOR) and are described in Ambar (1985), Ambar and Fiúza (1994), Daniault et al. (1994) and Frouin et al.

(1990). Most of the available data was from one of the 3 sections represented in Fig. 1.1 (I, II and III). The pink dots in the same figure represent the distribution of the available current meter moorings. The depths of the current meters are shown in the first subplot of Figures 2.5, 2.6 and 2.7, respectively for sections I, II and III. The time/depth distribution of the data is represented in Fig. 1.2. Data from the different sections are represented in different colors. We have a total of 11000 days of observations distributed over the various sections, depths and times. There are a total of 2520 days of observations in section I, 4981 days in section II and 3498 days in section III. We use all the available data to compute monthly averages for each of the current meter locations. We present the comparisons between the average seasonal cycle of currentmeter data and the model in chapter 2.

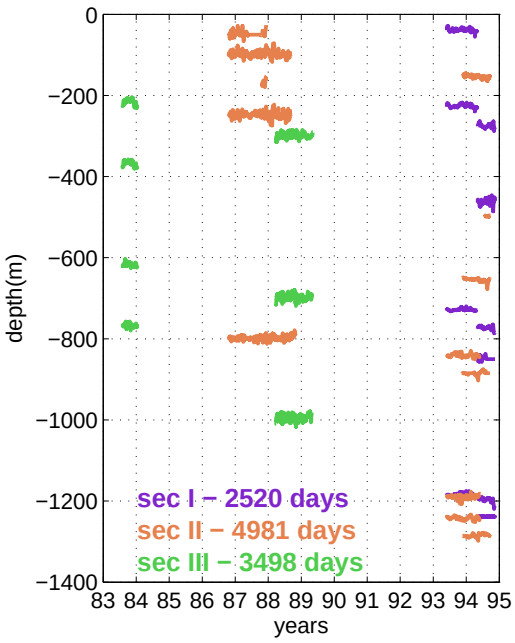

Figure 1.2: *Time-depth distribution of all the current meter data available. Data from the different sections (I, II, III) (represented in figure 1.1) is plotted with different colors. The inset shows the total number of days of data available in each section.*

1.3 Comparison of model results with observations

To compare the model results with the observations, we plot time series of monthly averages of different variables, for the model and the observations (Fig. 1.3). To summarize the model-observations comparisons the variables are plotted in a normalized Taylor diagram (Taylor, 2001) (Fig. 1.4). The Taylor Diagram shows the standard deviation of model and observations, the root mean square (RMS) error of the model, and the correlation coefficient between model and observations. The closer the model point is to the observations point, the better the model reproduces observations. To allow the comparison between the different quantities, model RMS and standard deviation of both model and observations were divided by the standard deviation of the observations.

The model velocity data were interpolated to the depth, latitude and longitude of each buoy. Figure 1.3 a, b and c, presents the comparisons for buoy 1, 2 and 3, respectively. The velocity components for locations of buoys 1 and 2 were rotated to the direction of maximum variance (approximately alongshore). In the case of buoy 3, the direction of maximum variance is coincident with the zonal component (less than 1° difference) and the zonal component is presented instead. The available time series start in 1998. There are discrepancies in some years, the clearest ones for buoy 1 in the end of 2003 and for buoy 3 in the end of 2001. We find a better comparison between the model and the velocity measured at buoy 2, with a correlation coefficient of about 0.75 (see Fig. 1.4). The model correlation with buoys 1 and 3 alongshore velocity is around 0.65. All the correlations are significant at 1% level. Despite these differences, the model reproduces the main observed variability with a high realism given the fact that no data assimilation is used.

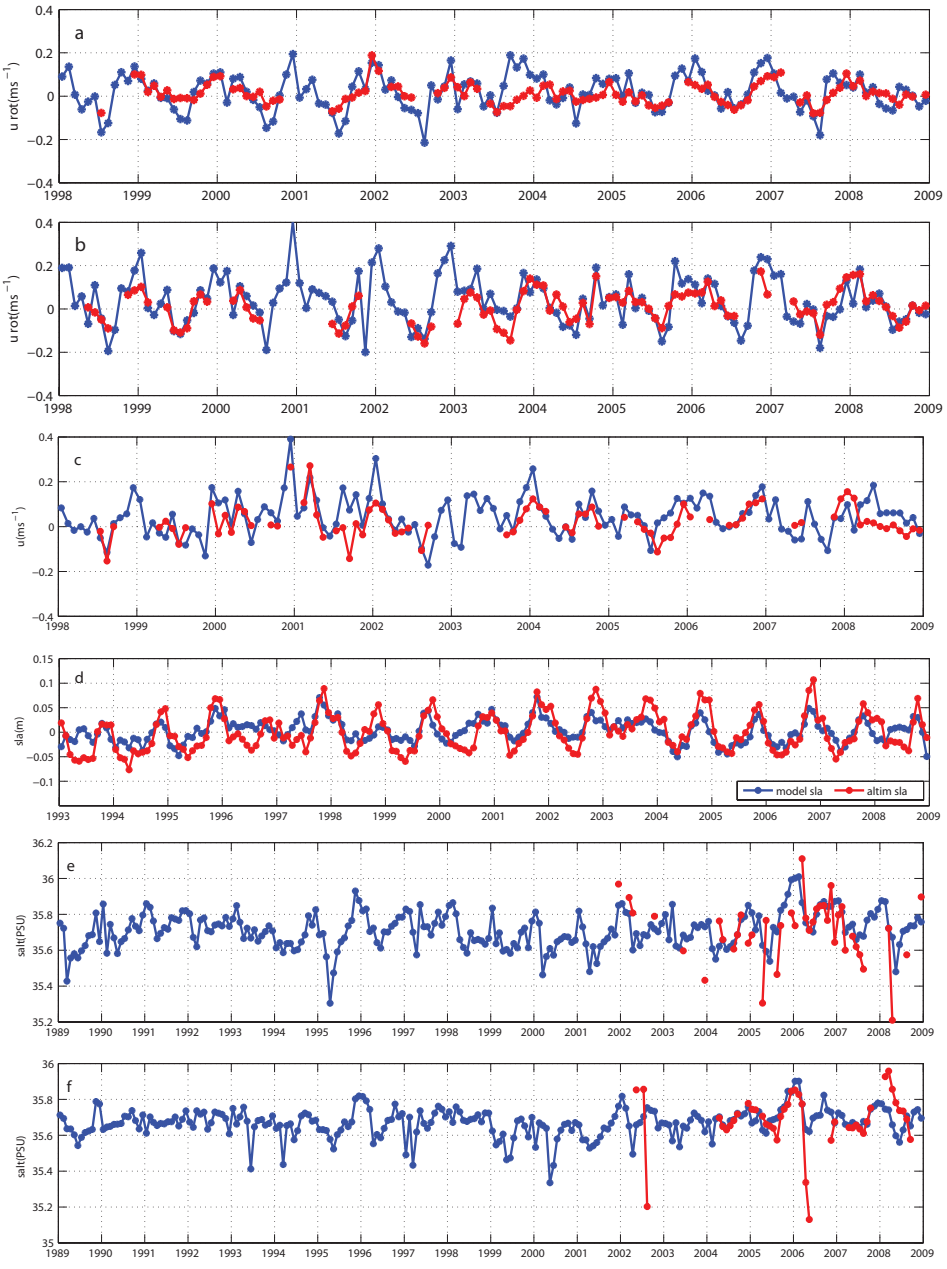

Figure 1.3: *Model (blue) – Data (red) comparisons. (a-c) alongshore velocity in buoys 1-3 (see buoys position in Fig. 1.1); (d) sea level anomalies, spatial averaged in domain W (see domain in Fig. 1.1); (e-f) salinity in buoys 1-2.*

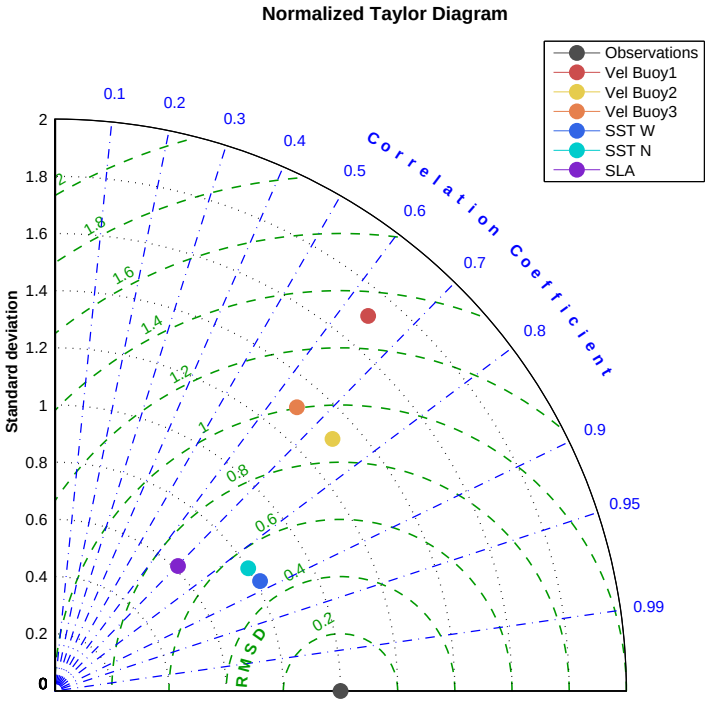

Figure 1.4: *Taylor diagram of model data comparisons. Comparison of all variables plotted in Fig 1.3 except salinity.*

The salinity comparisons are presented in Fig. 1.3 e and f, for buoys 1 and 2, respectively. Buoy 3 is not represented because there are few data available, very noisy and with many gaps. In some periods, there is a good comparison, as for example in buoy 1 from the beginning of 2006 till the middle of 2007, and in buoy 2 from beginning of 2004 till the beginning of 2006. But in other periods the comparison is bad. It seems that the model is not reproducing the low salinity anomalies, that might be associated with anomalous river discharges and intense river plume events not simulated because the model river discharge is climatological. Nevertheless, some failures and problems in the salinity sensors may not be excluded either, since these larger differences usually precede periods of missing data.

Model sea surface height is compared with altimetry data from AVISO (Fig. 1.3 d). Both model and AVISO data were horizontally averaged within

domain W (Fig. 1.1). The steric effect was added to the model solution (as in Peliz et al. (2013)), so that the comparison is possible. The model reproduces correctly the seasonal cycle and part of the interannual variability, but the covariance of both time series is not always good. The statistics of the comparison are represented in the Taylor Diagram (Fig. 1.4). The correlation between altimetry data and model is 0.7, significant at 5% level.

We also used satellite SST to compare with model SST for the northern and western coasts: we compare horizontal averages in domains N and W (Fig. 1.1), and will name it respectively, SSTN and SSTW. The model reproduces the average seasonal cycle (see Fig. 1.5 for SSTN and SSTW). In winter, the model SST is around 0.5°C higher than the observations, and in summer, it is around 0.5°C colder, on both the northern and the western coasts. This difference can be associated with a deficient parameterization of the mixing processes, or the surface heat fluxes. To compare the interannual variability of the SST anomalies, we computed the monthly means of the horizontal averaged SSTN and SSTW and removed the respective seasonal cycle. The interannual anomalies are well reproduced in the model (Fig. 1.6 for SSTN and SSTW). The statistics of these comparisons are represented in the Taylor Diagram (Fig. 1.4). In the case of the SST, we compare the time series after removing the seasonal cycle of both model and satellite data, since the seasonal cycle explains most of the variability of the SST. The correlation between model and satellite SST anomalies is between 0.8 and 0.9 (Fig. 1.4) for both the northern and western coasts (around 0.95 if the seasonal cycle is not removed). The correlations are significant at 1% level.

We plot the averaged December SST fields from model and satellite from 1989 to 2008 (Fig. 1.7), for comparison. The model fields were computed by averaging the entire month, while satellite images were computed by averaging the available cloud free data for each pixel, so they are not exactly same. The missing data in the satellite SST fields means that there was not any cloud free image on that month. Despite these differences, it is visible that the model captures the main observed interannual variability.

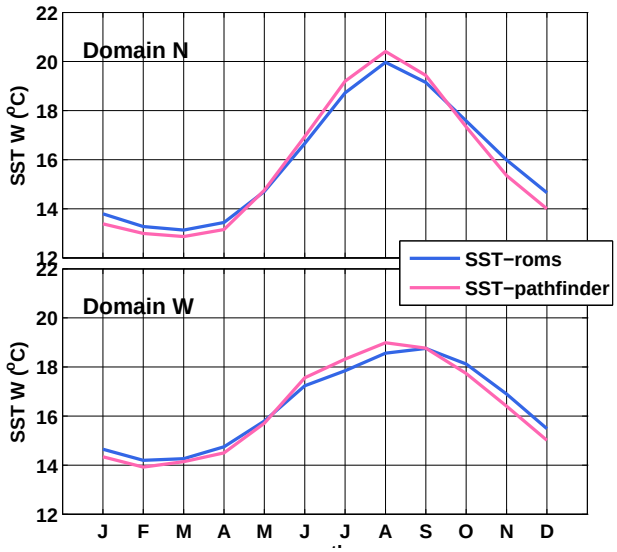

Figure 1.5: *Average seasonal cycle: (a) model and satellite SST averaged in domain N (see Fig. 1.1); (b) the same as (a), but for domain W.*

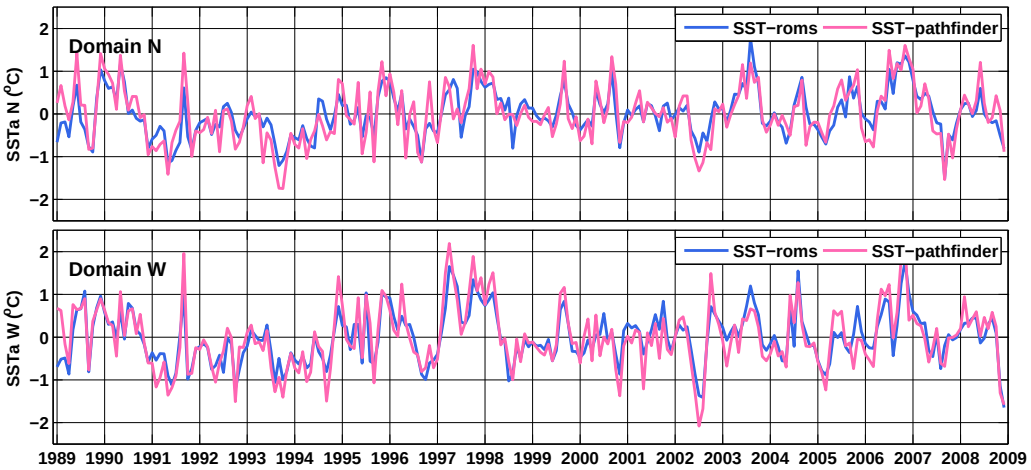

Figure 1.6: *Time series of anomalies, after removing the seasonal signal presented in Fig. 1.5. (a) model and satellite SST averaged in domain N (see Fig. 1.1); (b) the same as (a), but for domain W.*

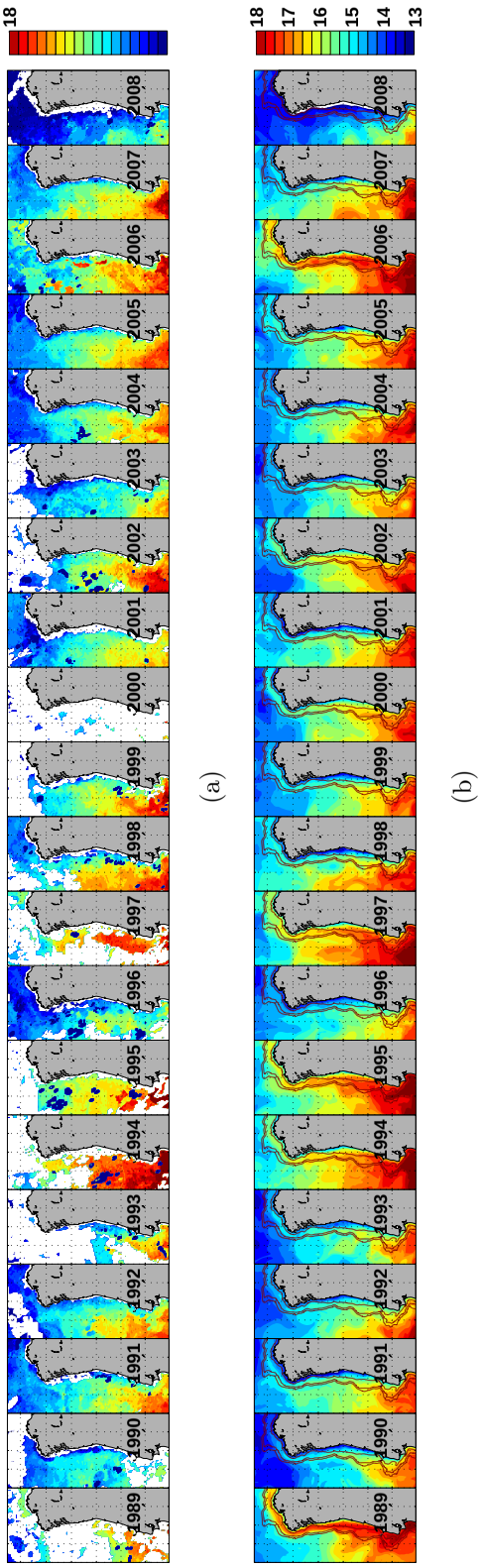

Figure 1.7: *December averaged SST fields (°C). top - satellite, bottom - model*

Chapter 2

Seasonal Cycle of the IPC and other Alongshore Flows

2.1 Introduction

The Western Iberian Margin is characterized by persistent, multicore seasonally varying flows. The summer is dominated by upwelling-type shelf circulation with associated equatorward currents, cold water fronts, filaments and eddies (Haynes et al., 1993; Relvas and Barton, 2002; Peliz et al., 2002). The Iberian Poleward Current (IPC) dominates the winter circulation over the upper slope and outer shelf. This current was described in observational and numerical studies (Frouin et al., 1990; Martins et al., 2002; Peliz et al., 2003a,b, 2005; Torres and Barton, 2006; Friocourt et al., 2007, 2008b,a). The IPC extends to the northern coast of the Iberian Peninsula, usually in December or January, as a narrow surface intensified current noticeable for its warm Sea Surface Temperature (SST) signature all along the northern Iberian Margin (Pingree and Le Cann, 1990, 1992b; Friocourt et al., 2008b; Le Cann and Serpette, 2009). Pingree and Le Cann (1992a) named this warm water intrusion in the north coast by *Navidad*, because it occurs near Christmas. At intermediate levels, the water also circulates poleward along the western Iberian slope, transporting the warm and saline Mediterranean

Water (Daniault et al., 1994; Ambar and Fiúza, 1994): in this study we will refer to it as the Iberian Poleward Slope Undercurrent (IPSU).

Llope et al. (2006) analyzed monthly series of CTD samplings from 1993 to 2003 and observed intrusions of Eastern North Atlantic Central Waters of subtropical origin (ENACWst) in the Northern Iberia almost every winter. This suggests that IPC has an important role in driving the average temperature and salinity seasonal cycles on the northern coast, but it was never quantified.

Despite the existence of many observational and modeling studies of this region, a systematic study of the mean structure and seasonal variability of the whole alongshore system was still missing. We use our simulation together with current meter observations, to make a characterization of the vertical structure of the mean alongshore flow and its mean seasonal variability. The main questions addressed in this chapter are: 1) How does the system evolve in the Spring and Autumn transitions? 2) What happens to the IPC in the summer, when the shelf is dominated by southward currents? 3) What is the importance of the IPC in the seasonal cycle of temperature and salinity?

2.2 Seasonal currents

We used the 20 years model outputs to compute monthly means of the velocity fields. In this section we will show the results of the horizontal and vertical velocity sections. All the results that will be presented are from the highest resolution domain (A1 in Fig. 1.1).

2.2.1 Horizontal circulation

In Fig. 2.2, we show the monthly mean fields of the depth-averaged velocities. The vertical average was done from the surface to the bottom, or to 500 m in the case of deep water columns. In January, the current over the slope and shelf flows to the north. From February to April the nearshore currents

evolve from a northward dominated flow to a southward flow. From April to July the southward upwelling jet over the shelf intensifies, reaching its maximum intensity in July. In August, the decay is visible and just offshore, over the slope, a weak northward flow is already detectable. In September, this northward flow intensifies, becoming dominant, although there is still some remnants of a weak southward flow in a few places close to the coast. In October, the flow is totally in the northward direction, over the shelf and slope. After a decrease in the velocity magnitude in November, the intensity increases in December.

During the transition months (February and March), north of 42°N, the time-averaged poleward flow appears to move offshore as the eastern flank of a slowly propagating time-averaged cyclonic cell, leaving the western limit of this plot by July (see C1 in the Fig. 2.2). South of this latitude, there is no sign of westward propagation of the flow. Instead, it is observed a steady cyclonic cell (C3 on Fig. 2.2), centered at about 41.5°N and 11.5°W, which seems to be associated with meandering onshore flow. From September to October, a second time-averaged cyclonic cell propagates offshore, along a latitude of around 42.5°N (C2 in the figure).

Associated with the seasonal cycle of the upper layer currents there is also a seasonal cycle of the Sea Surface Height anomaly (SSHa). Fig. 2.3 shows an Hovmoller plot of the SSHa meridionally averaged from 40° to 43°N and plotted as a function of longitude and months of the year (the latitude band can be seen in Fig. 2.1, green boxes Y and Z together - we did not compute separately for box Y and Z because of the low resolution of the altimetry product). The subplot a) represents altimetry data and subplot b) the model results. A negative anomaly establishes near the coast in the summer months, from April until the end of September, that is more intense in July and August (the months of maximum upwelling intensity). In October, the signal reverses and it is time for the onset of a positive anomaly near the coast, which is present till the end of March. Both summer and winter anomalies propagate offshore. We find a reasonable match between

the altimetry and the model results, in what concerns both the seasonal cycle of SSHa and the offshore propagation of the anomalies.

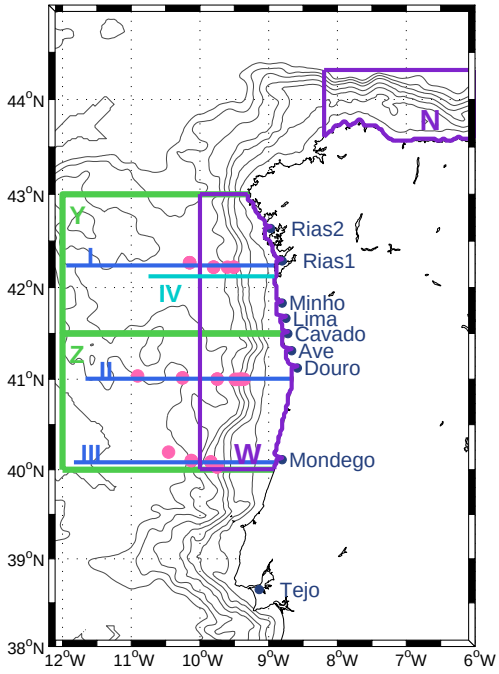

Figure 2.1: *Three 200-km wide sections (I, II and III, respectively at 42.2° N, 41° N and 40.1° N) will be referred in the text to show the vertical velocity structure. Section IV will be referred to show temperature and salinity vertical structure. The pink dots represent the current meter observations. The green boxes will be used to average eddy kinetic energy. The purple boxes represent 2 domains, on northern and western coasts. The gray contours represent the isobaths of 100, 200, 500, 1000, 2000, 3000, 4000 and 5000 m.*

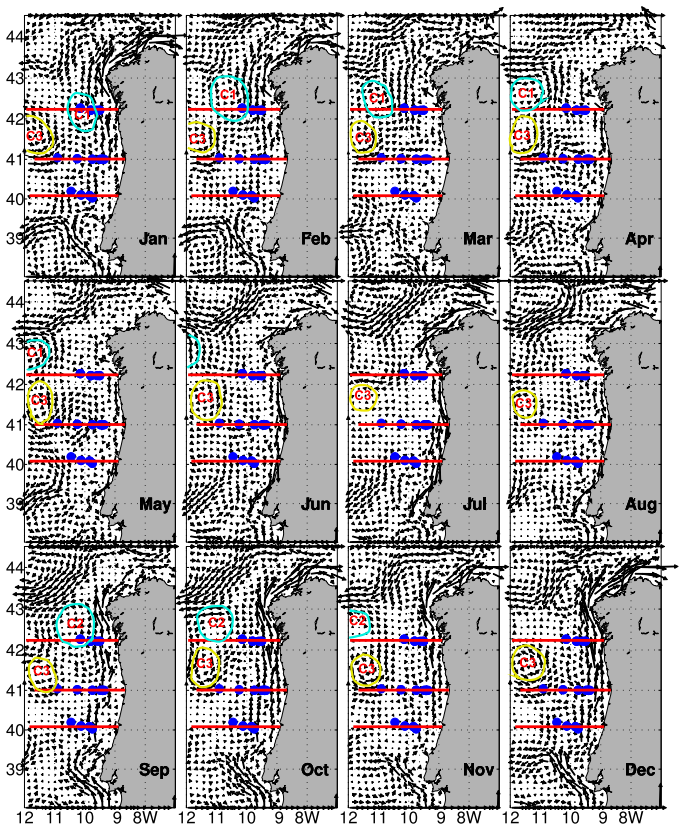

Figure 2.2: *Monthly mean fields of the depth-averaged velocity for the top 500 m (or down to the bottom in sites shallower than 500 m). The red lines and blue points correspond to the sections and current meters positions shown in Figure 2.1. C1, C2 and C3 are average cyclonic cells, described in the text.*

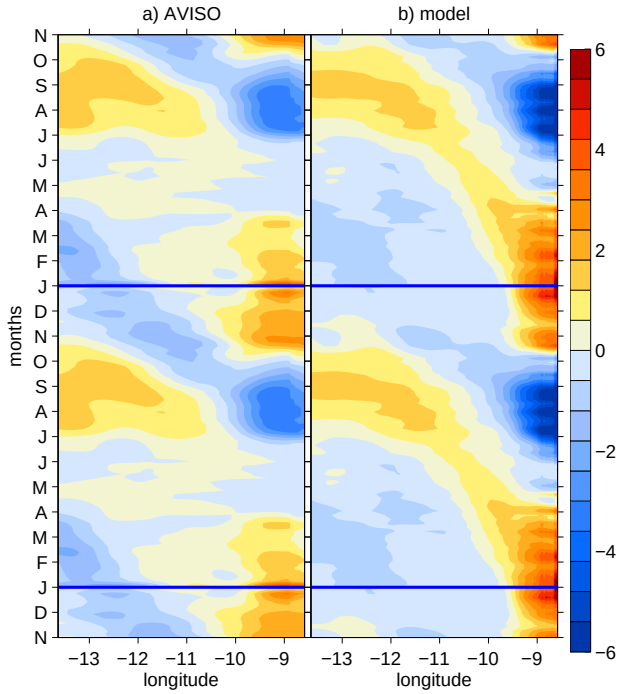

Figure 2.3: *Hovmoller diagrams of SSHa (cm). Meridionally averaged from 40° to 43°N (see Figure 2.1). a) SSHa from altimetry (AVISO). b) SSHa from model. Note that the parts above and below the blue lines replicate the monthly averages to facilitate the perception of the seasonal cycle.*

2.2.2 Vertical structure of the alongshore currents

In this section, we describe the seasonal variability of the alongshore currents (North-South component) for our 3 control sections (see Fig. 2.1 and 2.2). In order to evaluate what is the importance of the seasonal variability compared to the total variability of the currents, we calculated the best fit to the meridional velocity of one sinusoid with one-year period and another one with 6-months period, and computed the standard deviation of these adjusted curves. Then we divided each standard deviation by the total standard deviation to estimate the relative importance of these 2 components of variability. The results are plotted in Fig. 2.4. For all 3 sections, the seasonal frequency (first row) is more important over the shelf and over the slope, in

the upper 300 m of the water column, where more than 40% of the total variability is due to the seasonal cycle. In sections II and III, the seasonal cycle is also relevant at deeper levels near the slope, explaining around 20 to 30% of the total variability. Different cores are present on these sections, representing areas with different relative importance of the seasonal cycle: one on the shelf, other on the upper slope/shelf break and a third one over the slope at the Mediterranean Water levels (600-1200 m depth). Off the slope, the seasonal cycle contribution is low. Looking at the second row (variability due to the half-year component), it is visible that section I has higher values, with more than 25% of the variability explained by this component. This is related to the offshore propagation of the average cyclonic cells C1 and C2, shown in Fig. 2.2. In sections II and III, there are significant values at levels deeper than 600 m over the slope. The third row shows that the seasonal cycle and its first harmonic explain more than 40% of the variability of both the slope and shelf alongshore currents, justifying the study of the mean monthly evolution of the alongshore currents. Offshore of the slope zone these time frequencies of variability of the alongshore velocity are important in section I, explaining more than 40% of the variability, but not as much in sections II and III, where monthly (eddies) or interannual scales taken together are more important (not shown).

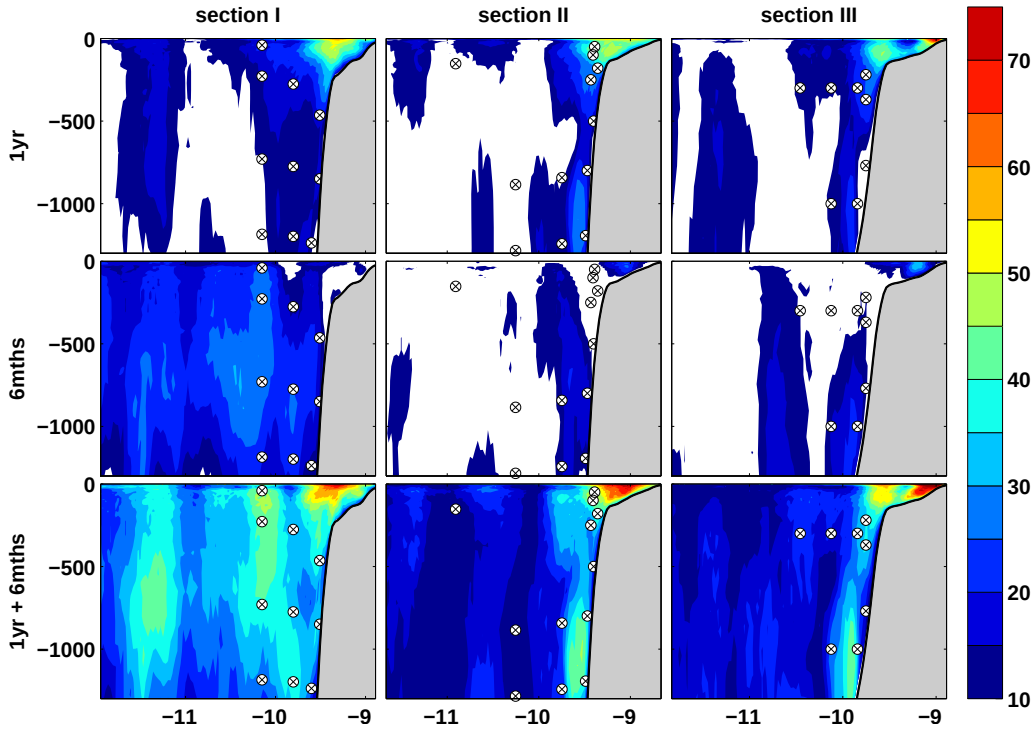

Figure 2.4: *Percentage (%) of standard deviation relative to seasonal and 6 month variability of alongshore currents. Sections I, II and III (Fig. 2.1) are represented in the different columns. First row - percentage of variability of the 1-year period adjusted sinusoid. Second row - percentage of variability of the half-year period adjusted sinusoid. Third row - sum of both, total variability explained by the seasonal frequency and its first harmonic. Areas in white - variability explained by that component <10%. The little circles with a cross show the positions of the current meters.*

2.2.2.1 Section I - 42.2°N

The monthly averages of the alongshore currents (north-south component of velocity) for section I are displayed in Fig. 2.5. In January, there is a deep northward flow over the slope, extending from the surface to 1200 m depth. The vertical structure shows the presence of two cores of northward velocity, respectively, the IPC, intensified in the upper 200 m of the water column with

maximum intensity at the surface, and the IPSU, closely confined to the slope and extending from 600 to 1200 m depth. Between the two cores, centered at around 400 m depth near the slope, a weak southward core is noticeable. We will name this southward flow as Upper Slope Countercurrent (USCC). Over the shelf, there is a coastal jet of positive velocity associated with southerly winds and winter river plumes. From February to April the IPC intensity decreases. The flow widens and seems to propagate offshore. The offshore propagation occurs at all depths, but seems to be stronger in the upper 800 m of the water column. This positive anomaly propagating westward corresponds to the eastern side of the average cyclonic cell C1, observed in the horizontal velocity fields of Fig. 2.2. Near the slope, at 400 m depth, USCC is visible from January to May (not clearly southward in February). From April to July, the shelf is dominated by increasing southward flow associated with the upwelling jet. However, just offshore of the upwelling jet, there is still the evidence of a poleward flow, as a thick structure extending from near the surface down to more than 1200 m deep. In August and September, the southward upwelling jet is weaker and shallower, hiding the IPC and the IPSU below the surface. The two cores of positive velocity become visible again - the IPC near the shelf break at around 200 m depth and the IPSU over the slope from 600 to 1200 m depth. From October to December, the flow is northward all over the slope and the shelf (although USCC emerged in November). The IPC intensifies near the surface reaching a maximum in December, after a decrease of the intensity in the whole water column in November. It looks like as IPC starts developing in August over the shelf break and reaches its fully developed stage in December.

2.2.2.2 Section II - 41°N

In section II (Fig. 2.6), the seasonal evolution of the slope and shelf currents is quite similar to the one described for section I. There are two main differences. In the first place the poleward flow is narrower. In the second place the signs of westward propagation of the poleward flow are much weaker than those

observed in section I. Nevertheless, in the upper 800 m of the water column the flow seems to widen and part of it migrates offshore in February and March. After April the structure of the offshore currents shows no further evolution. In fact, the offshore region shows weak seasonal variability. It is dominated yearlong by a southward velocity core centered at around 9.8°W, and a northward weak and wide current centered at around 10.8°W. This positive component corresponds to the eastern side of the average standing cyclonic cell C3, that appears in the horizontal average fields (Fig. 2.2).

2.2.2.3 Section III - 40.1°N

Fig. 2.7 represents the seasonal evolution of the alongshore flow in section III. The seasonal cycle is similar to the other 2 sections, although the alongshore flows are in general weaker and more barotropic. There seems to be a weak offshore propagation from February to April. The offshore region shows no relevant seasonal variability, but contrary to what is observed in section II, the main circulation is southward all year long. In this section (and in section II also), in September and October the slope poleward flows are vertically coherent and there is no distinction of the IPC and IPSU cores. This means that the current on these months is more barotropic in sections II and III than on section I, where the presence of two cores is visible along the entire year. The IPC maximum is also in December and January, but the maximum intensity is not at the surface but at around 100 m depth.

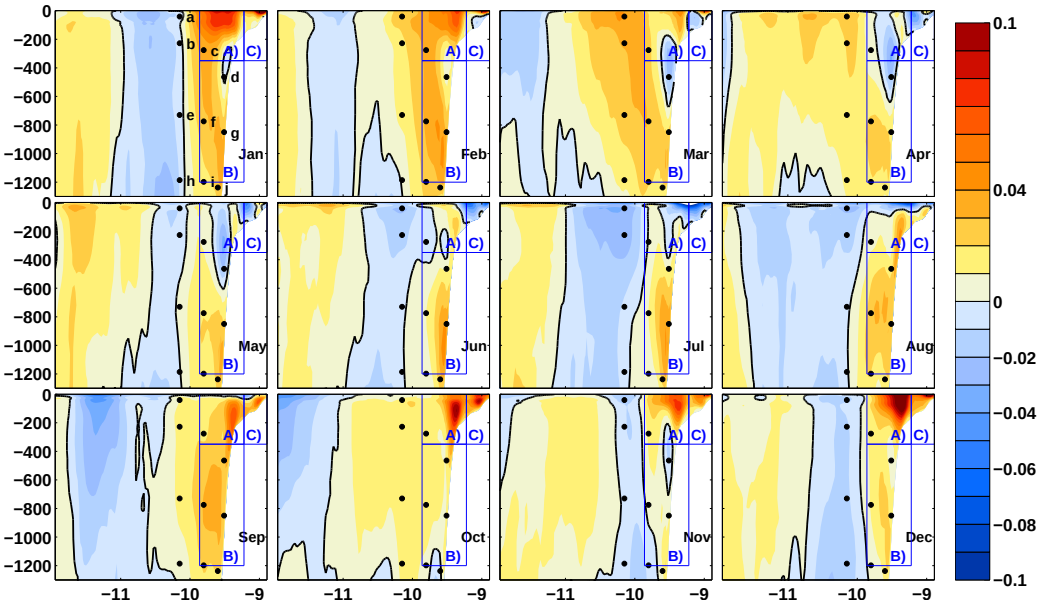

Figure 2.5: *Section I (see Fig. 2.1) - Vertical sections of the monthly averages of 20-years simulation of alongshore velocities (m s^{-1}) - positive values correspond to northward flow. The black dots represent the position of the current meters available for the section (labeled in the January field). The 3 areas represented with blue boxes (A, B, C) are used to compute integrated transport in section 2.2.2.5.*

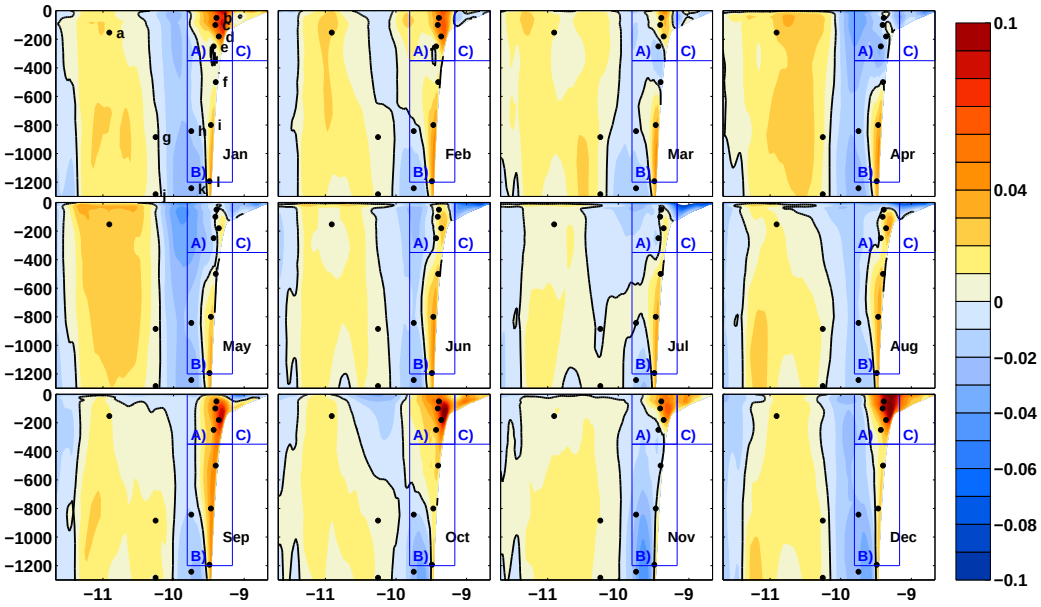

Figure 2.6: *The same as Fig. 2.5, for section II (see location on Fig. 2.1).*

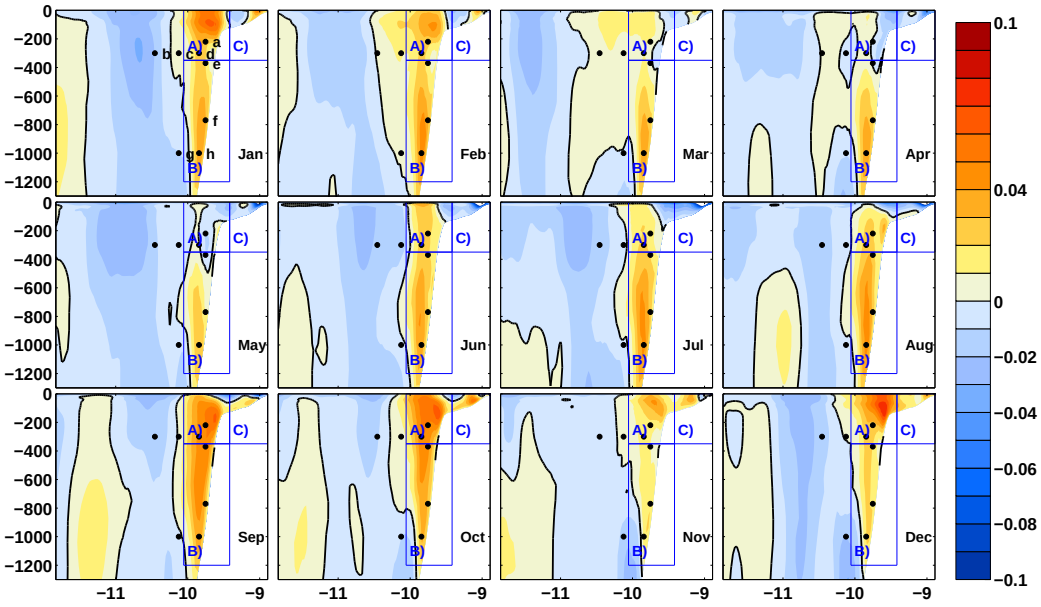

Figure 2.7: *The same as Fig. 2.5, for section III (see location on Fig. 2.1).*

2.2.2.4 Comparison with current meter data

Figures 2.8, 2.9 and 2.10 show a comparison between model and current meter time series statistics for the alongshore velocity component. Each subplot corresponds to a current meter location (see black dots in the velocity cross sections of Figures 2.5, 2.6 and 2.7, for section I, II and III, respectively) and the plots are aligned according to the position of the current meters: the left to the right corresponds to the offshore to the coast and top to the bottom corresponds to the depths of the current meters. We computed monthly averages of the current meter alongshore velocity whenever there were a minimum of 14 days of data per month (missing points correspond to values below that threshold). We also computed monthly averages of the model in the locations of the current meters.

In general, for all the 3 sections, the current meter averages lie inside the shaded area. There is a better correspondence between model and data for the time series closer to the coast, as compared to those offshore (see the values of root mean square error RMSe on the plots, as a measure of correspondence between model and observations). This makes sense, because there is a stronger signal of the seasonal cycle closer to the coast (as shown in Fig. 2.4). In these areas where seasonal variability is small compared to interannual or eddy induced variability, we should not expect a good agreement between the seasonal cycle of the model and that of the observations.

In section I (Fig. 2.8) the match between the model and the observations is reasonable, even offshore, unlike what happens in the other sections. This is because in this section the 6-month period sinusoid explains a significant part of the variability, associated with the offshore propagation of the average cyclonic cells C1 and C2, described in section 2.2.1. Since this signal is observed in the current meter data at the same locations, it provides further evidence that the offshore propagation of these anomalies is something recurrent and realistic in a seasonal cycle.

Fig. 2.9 shows the comparisons for section II. In the offshore locations (current meters a), g), h), j) and k) - see positions on Fig. 2.6) there is

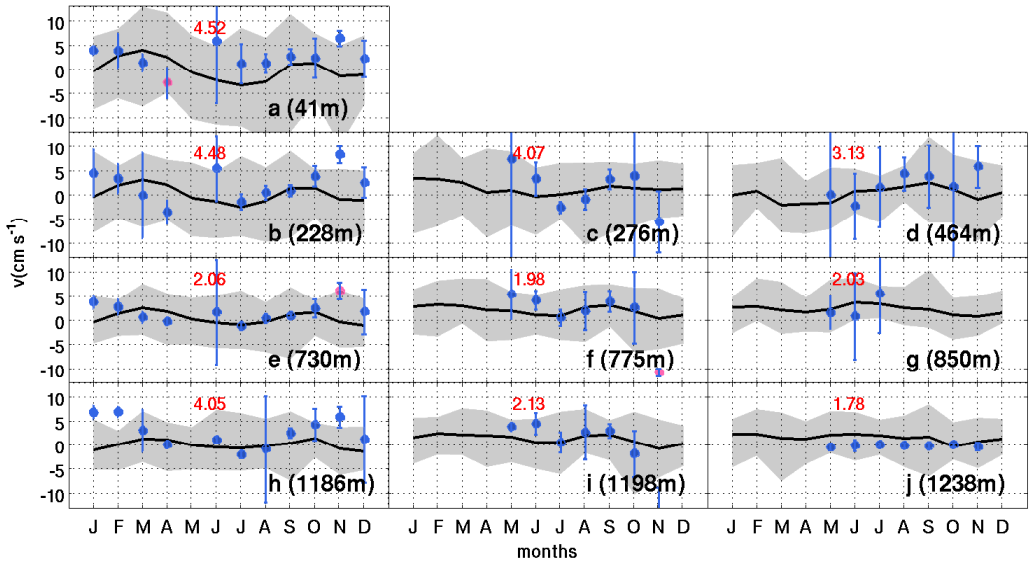

Figure 2.8: *Section I (see Fig. 2.1) - Comparison of alongshore currents from current meter monthly averages and model results (cm s^{-1}). Each subplot corresponds to a current meter location. Lowercase letters in the cross sections from Figure 2.5 correspond to the subplots. Black line - monthly averages of the model. Grey shading - maximum and minimum monthly averages from the entire 20-year model run. Dots - monthly averages obtained from the current meters. Blue bars - uncertainty in the estimation of current meter mean, following a t-student distribution. The number in red represents the root mean square error as a measure of the difference between observations and model (the pink dots were not considered to compute the RMSe because their values were more than 2 standard deviations away from the current meter mean for each plot)*

not a clear seasonal cycle and the average alongshore current in the model results is close to zero in all months. The current meter alongshore velocity values also do not show any sign of a seasonal cycle. It is thus not expected that the values compare well. Over the slope (subplots b), c), d), e), f), i) and l)) the comparison is better, since the seasonal component of variability is important here (see Fig. 2.4 - section II). This is the section with more observations in the slope zone. Some of the most important features obtained in the model results are also present in the observations statistics. Subplot

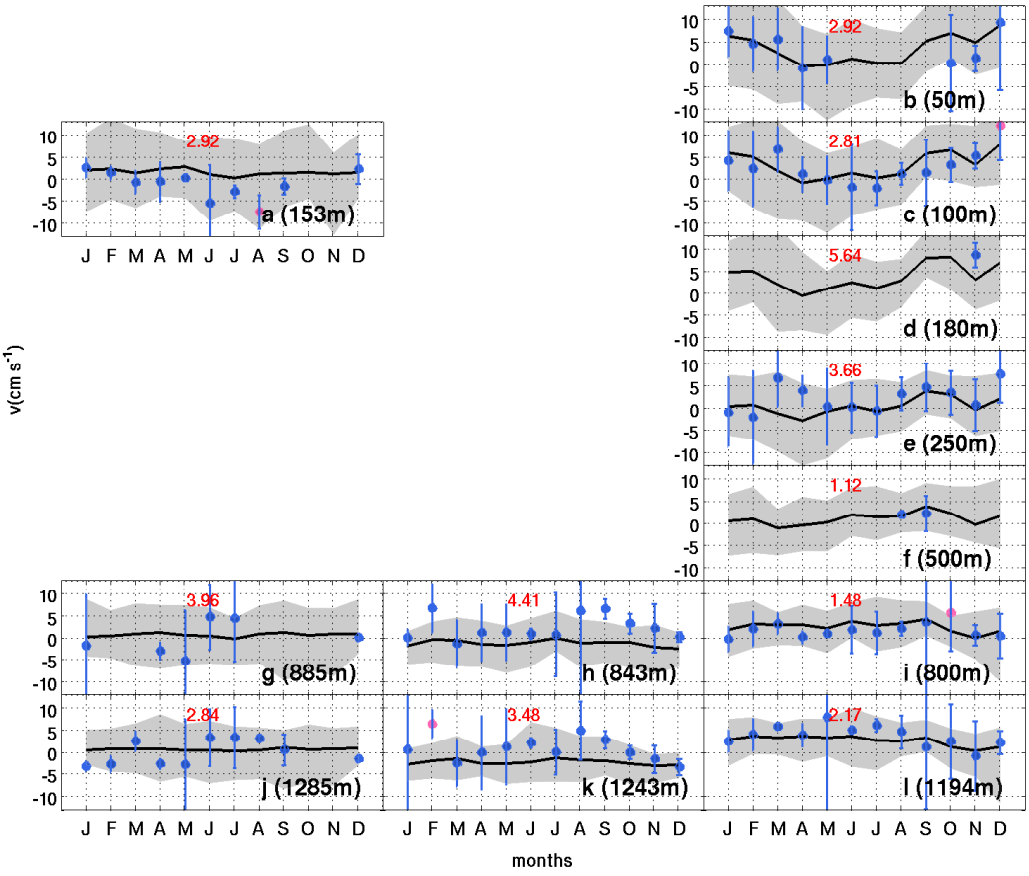

Figure 2.9: *The same as Fig. 2.8, for section II (see location on Fig. 2.1). Lowercase letters in the cross section from Figure 2.6 correspond to the subplots.*

c) shows that at 100 meters depth, the flow is already northward in August, confirming the presence of poleward velocities over the upper slope / shelf break, as obtained in the model (see Fig. 2.6 - August). At 250 meters depth (subplot e) there is a good match between data and model (except for March, April and December). The poleward flow at this depth intensifies from July to September, and then decreases till November, unlikely what happens at 100 m depth (subplot c) where poleward flow intensifies from July to December - confirming that after September the IPC starts to intensify near the surface and to weaken at deeper levels. Looking into the series at the Mediterranean Water levels (subplots i) and l) - at 800 and 1194 meters

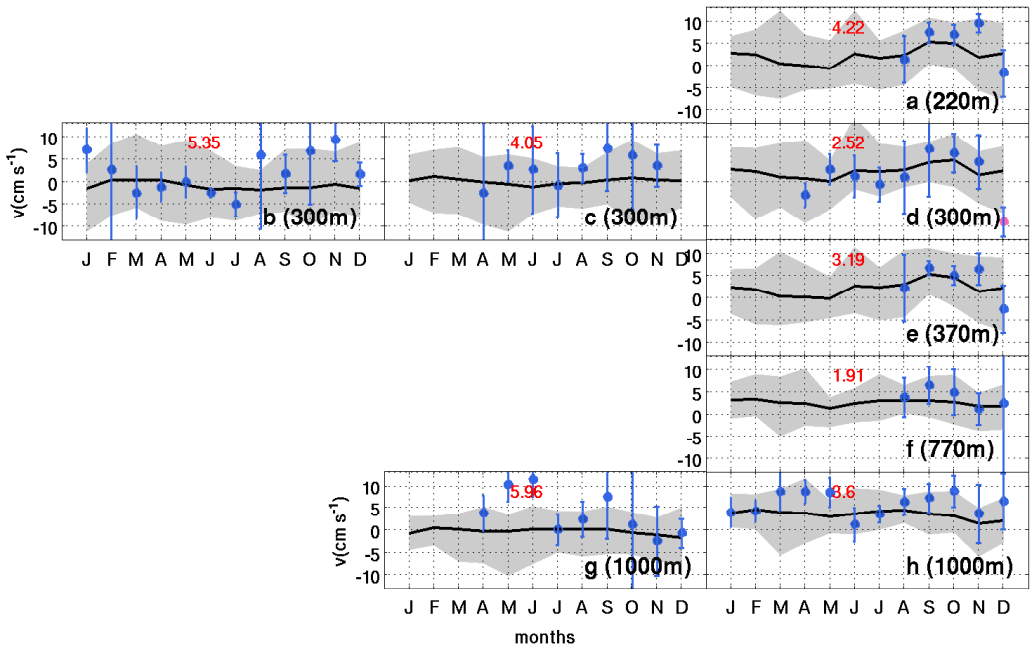

Figure 2.10: *The same as Fig. 2.8, for section III (see location on Fig. 2.1). Lowercase letters in the cross section from Figure 2.7 correspond to the subplots.*

depth, respectively), the data confirm that the current is northward almost all year long, decreasing or even changing sign in November.

The comparisons for section III are represented in Fig. 2.10. They are bad for the offshore locations (subplots b), c) and g) - see positions on Fig. 2.7), as can be seen by the high RMSe. This is expected, since the seasonal signal in these locations is rather weak. For the current meters located over the slope (a), d), e) f) and h)), there is not much data, but again it is visible that after August for all depths, the flow is northward, both in the model and in the observations.

All the observations confirm that in the upper slope / shelf break the flow in August is already poleward, and from September to December it intensifies near the surface, reaching the maximum surface velocities in December. This supports our idea that the IPC starts developing over the shelf break and then intensifies near the surface. At Mediterranean Water levels, over the

slope, the observations confirm the presence of poleward flow almost all year long (the IPSU), and also that IPSU is subjected to seasonal variability, with minimum intensity in November.

2.2.2.5 Meridional transports

To summarize the information about the alongshore flows, we computed the meridional transport for the 3 different sections. We divided each section in 3 areas according to their dynamical properties (these areas are shown in Figures 2.5, 2.6 and 2.7, for sections I, II and III, respectively). The areas are named: Surface Slope (A) - that corresponds to the region over the slope from the surface to 350 meters deep, enclosing the IPC core; the Deep Slope (B) - that is the region over the slope, from 350 to 1200 meters deep, containing the IPSU core; and the Shelf (C) - that contains all the water column over the shelf. The transports for each area and section are presented in Fig. 2.11. Since the areas where the transports were computed are different for the different sections (because the bathymetry is different), the absolute values are not directly comparable between each other. The idea is to systematize the results for each section and compare the seasonal cycles of the 3 sections. The continuous lines represent northward transport and the dashed ones southward transport (computed using northward and southward velocities across the areas).

Fig. 2.11 (A) shows northward and southward transports across the Surface Slope area. It encloses the IPC, both the surface intensified December-January core and the shelf break core, present by the end of the upwelling season. The seasonal cycle of the northward transport shows two maxima: one in December-January and the other in September-October. The seasonal cycle is quite similar for sections II and III. In section I (northernmost one) there is a greater intensification of the northward transport in the period from December to February.

Fig. 2.11 (B) shows the transports across the Deep Slope area. Again, like in A (Surface Slope), the northward transports for the 3 sections present

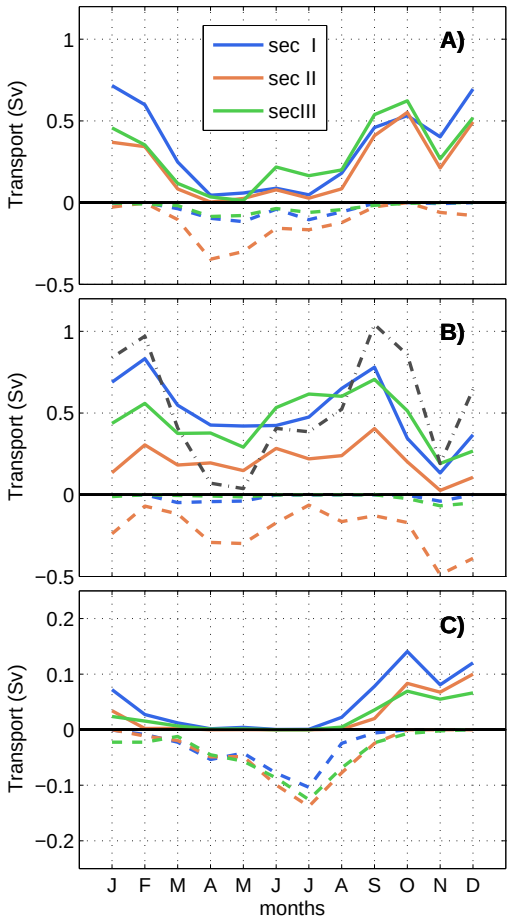

Figure 2.11: *Seasonal cycle of the meridional transport across different areas and for sections I, II, III (Fig. 2.1). The areas A(surface slope), B(deep slope) and C(shelf) are represented for section I, II and III in the figures 2.5, 2.6 and 2.7, respectively. Colors correspond to the different sections. Continuous lines represent northward transport and dashed lines represent southward transport. The dashed-dotted gray line in the middle subplot represents the total net transport (north+south) of the slope area (A+B) averaged between the 3 sections.*

2 maxima along the year. The maxima are in February and in September for all the sections, not totally in phase with the surface ones, lagging the winter peak in one month and anticipating the autumn peak in one month. The net transport is northward all year long for all sections. The only months when

southward transport values are comparable to northward ones, are April, May, November and December, for section II.

The total net transport (sum of deep slope transport with surface slope transport) averaged between the 3 sections, is represented in Fig. 2.11 (B). It shows 2 maxima along the year: one in September, with an average transport of 1.1 Sv and the other in February, with an average of 1 Sv. The lowest transport values are observed in April, May and November.

Finally, the shelf area is represented in Fig. 2.11 (C). The dominant transport during the summer is to the south, coincident with summer upwelling and associated southward jet. The southward transport is significant from March to September and reaches a maximum in July, of about 0.12 Sv. There are no significant differences between the 3 sections. From September to January the net transport over the shelf is to the north. There are several processes contributing to the northward transport over the shelf: currents induced by the river plumes (which are more frequent in winter times), southerly wind episodes and the penetration of the slope northward current into the outer shelf.

2.3 Surface eddy kinetic energy

It is expected that this strong seasonality in the mean alongshore currents may drive a seasonal signal in the Eddy Kinetic Energy (EKE). An Hovmoller's diagram of the meridional average of EKE computed at 20 m depth is represented in Fig. 2.12. The plot on the left is a meridional average of the values from 41.5°N to 43°N (region Y in green - Fig. 2.1) and the one on the right is a meridional average between 40°N and 41.5°N (region Z in green - Fig. 2.1). The plots are separated because of the significantly different EKE absolute values in the two areas. Although there are not many differences in the seasonal cycle, it is clear that the northern part has much larger eddy activity (high values of EKE) than the southern one. Concerning the seasonal cycle, there are two maxima of EKE near the coast along the

year. The first maximum is observed from December to March: it seems to propagate offshore but only till 10.5°W, west of this longitude the signal is much weaker. The second EKE maximum near the coast is observed from August to October: it propagates offshore as far as 12°W, without much loss in intensity. These two maxima of EKE near the coast are coincident with the surface intensified poleward current and its dissipation (December to March) and with the end of the upwelling season (August to October). The presence of eddies and filaments in this area have been described in previous studies, both for the winter and summer high EKE periods. High mesoscale activity during the winter period has been described by Pingree and Le Cann (1992b), Garcia-Soto et al. (2002) and Peliz et al. (2003b). It is mostly associated with the formation of long lived anticyclonic eddies, by processes of destabilization of the IPC and named "Swoddies" (for "Slope Water Oceanic eDDIES"). Most of the Swoddies observed and described previously, are detached from the slope in December/January, mainly in years of strong IPC. This is in agreement with our results. For the summer period, the mesoscale is first of all associated with the presence of filaments and eddy shedding at the end of the upwelling season (Haynes et al., 1993; Relvas and Barton, 2002; Peliz et al., 2002).

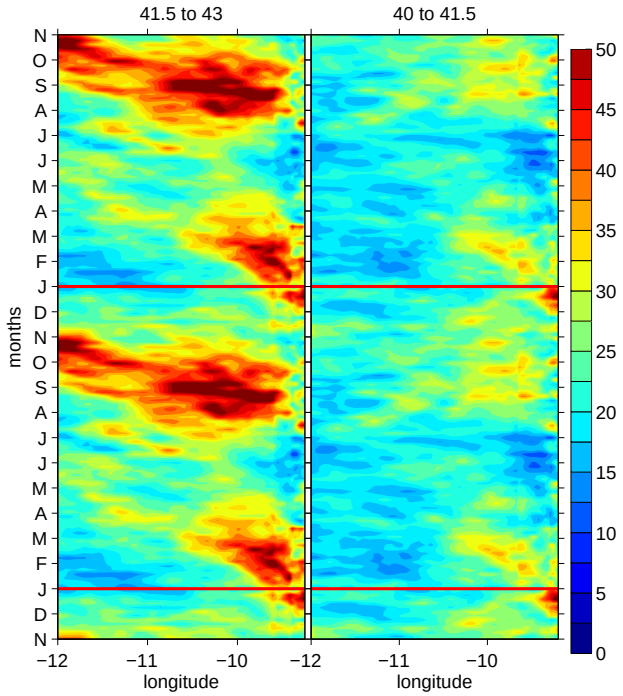

Figure 2.12: *Hovmoller diagrams of EKE (cm^2s^{-2}) at 20 m depth. Plot on the left - meridional average of the values from 41.5°N to 43°N (region Y in green - Fig. 2.1). Plot on the right - meridional average of the values from 40°N to 41.5°N (region Z in green - Figure 2.1). Note that part of the plot is replicated to facilitate the visualization of the seasonal cycle.*

2.4 Temperature and Salinity

To study the average seasonal cycle of temperature and salinity in the slope and shelf regions, we computed the monthly means of temperature and salinity volume averaged in the top 200 m of domains N and W (Fig. 2.1). Hereinafter we refer to these quantities as TW200 and SW200 for domain W, and TN200 and SN200 for domain N. We also present the variability of the mean northward transport in the upper 200 m of domain W (VW200). The mean northward transport was computed across various zonal sections inside domain W and then averaged, to avoid the influence of local eddies or fila-

ments. We chose to average all the quantities in the top 200 m in order to include the main core of the IPC, even when it is not surface intensified.

The seasonal cycle of the northward transport (VW200) on the west coast is plotted in Fig. 2.13 e). The phase is comparable with Fig. 2.11 a): it is stronger from September to February reaching a first peak in October and the maximum in December.

The SST seasonal cycle amplitude is higher on the northern coast (SSTN; Fig. 2.13 a) than on the western coast (SSTW; Fig. 2.13 c), with colder values in winter and warmer in summer. On the west coast, the summer maximum is lower than that on the northern coast because there is more intense upwelling.

On the northern coast, the seasonal cycle of TN200 (Fig. 2.13 a) lags that of SSTN, reaching its maximum only in October. SN200 (Fig. 2.13 b) is highest from November to January, suggesting a contribution of the IPC in transporting salty waters to the north (Llope et al. (2006) also observed maximum salinities from November to February in the north coast, at 200 and 300 m depth).

There is a large difference between the SSTW and TW200 seasonal evolution in the west coast (Fig. 2.13 c). The summer warming is compensated by the upwelling of colder waters in July and August. TW200 reaches maximum intensity in October, suggesting a contribution from IPC. SW200 seasonal cycle is similar to that of VW200 indicating that the IPC is important in driving the salinity variability. Figure 2.14 shows the average vertical sections (section IV on Fig. 2.1) of alongshore velocities together with, respectively, temperature (top) and salinity (bottom), for the main months of the IPC season (September to January). The latitude of the section was chosen to be coincident with the position of buoy I. The presence of the salinity maximum over the upper slope, and approximately coincident with the IPC core (Fig.2.14 - bottom row), further suggests the importance of the IPC in transporting salinity northwards from September to January. The same is true for the temperature sections (Fig. 2.14 - top row) as can be seen by the

downward tilting of the isotherms towards the upper slope.

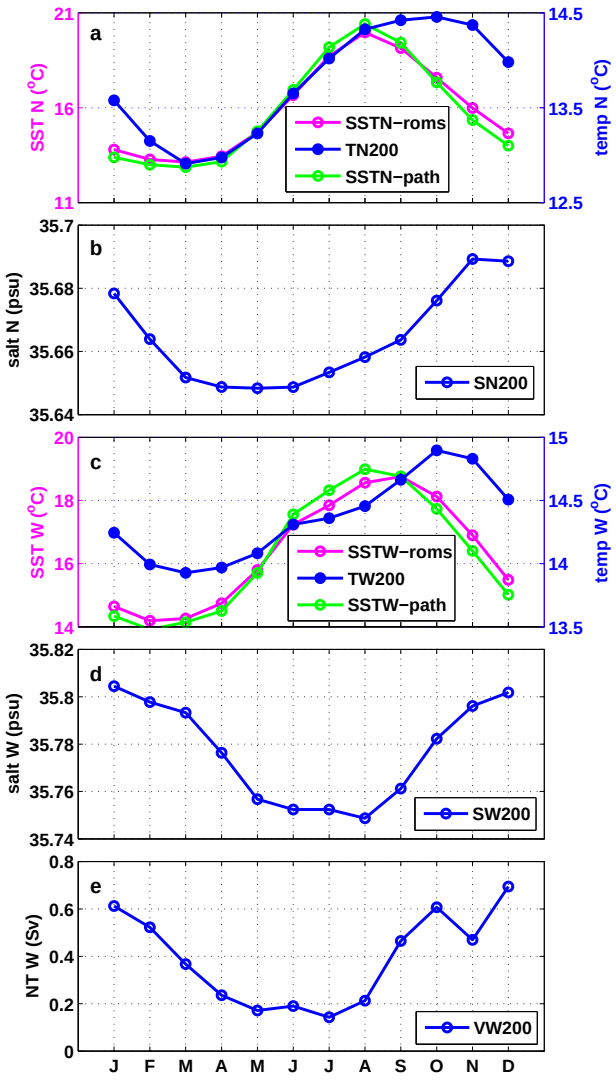

Figure 2.13: *Average seasonal cycle: (a) volume averaged temperature (°C) in the upper 200 m (TN200) (model) and SST (model and satellite), all averaged in domain N (see Fig. 2.1); (b) volume averaged salinity in the upper 200 m (SN200) (domain N); (c) TW200, the same as a, but for domain W; (d) SW200, the same as b, but for domain W; (e) average northward transport in the upper 200 m and in domain W (VW200).*

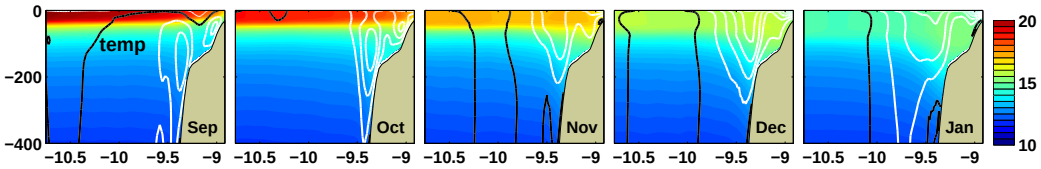

(a)

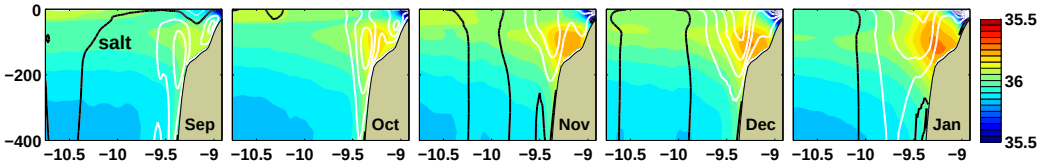

(b)

Figure 2.14: *Monthly average vertical sections (section IV on Fig. 2.1) of meridional velocities (contours) together with: top) temperature (°C); bottom) salinity (psu) in colors . The various columns correspond to different months. The velocity contours have an interval of 0.03 m s^{-1}; positive values are displayed on a thick white line, negative on a thin white line, and zero is in black.*

2.4.1 Heat and Salt Budgets

In order to understand the different factors forcing the seasonal cycle of salinity and temperature, we computed the heat and salt budgets in the top 200 m of the water column, using the equations 2.1 and 2.2:

$$\begin{aligned} \int_{z_0}^{\eta} \rho_0 C_p \frac{\partial T}{\partial t} dz &= -\int_{z_0}^{\eta} \rho_0 C_p \vec{v}.\vec{\nabla} T dz + Q_{atm} + \int_{z_0}^{\eta} \rho_0 C_p D h_T dz - \rho_0 C_p \kappa_v \frac{\partial T}{\partial z}\Big|_{z_0} \\ Q_{atm} &= HFsen + HFlat + radSW - radLW \end{aligned} \tag{2.1}$$

$$\begin{aligned} \int_{z_0}^{\eta} \frac{\partial S}{\partial t} dz &= -\int_{z_0}^{\eta} \vec{v}.\vec{\nabla} S dz + S_{forc} + \int_{z_0}^{\eta} D h_S dz - \kappa_v \frac{\partial S}{\partial z}\Big|_{z_0} \\ S_{forc} &= S(E-P) \end{aligned} \tag{2.2}$$

In both equations, the term on the left side refers to the time rate; the first term on the right represents advection of both heat and salt; the second term on the right represents the atmospheric forcing (Qatm, Sforc); and the third

and fourth terms represent the horizontal and vertical mixing, respectively. Horizontal mixing is null everywhere but near the mouth of the rivers, where it is used to improve the representation of river plumes. Vertical mixing is significant only sporadically, when the mixed layer is deeper than 200 m. Most of the time, the mixing terms are negligible when compared to other terms, and the equations simplify to Eq. 2.3:

$$\begin{aligned} \frac{\partial Q}{\partial t} &= -adv(Q) + Q_{atm} \\ \frac{\partial S}{\partial t} &= -adv(S) + S_{forc} \end{aligned} \tag{2.3}$$

Qatm is the total atmospheric forcing that includes: the sensible heat flux (HFsen); the latent heat flux of evaporation (HFlat), the shortwave incident radiation (radSW) including the penetrating short wave radiation; and the outgoing long wave radiation (radLW). Sforc is the atmospheric fresh water forcing, that is evaporation minus precipitation, multiplied by the surface salinity. A similar procedure was followed in Wilkin (2006) and Colas et al. (2012).

Figure 2.15 shows the horizontal fields of the budgets, averaged for specific months (over the entire period of 1989 to 2008), and integrated in the top 200 m of the water column. The figure shows time rate, advection and atmospheric forcing for the months of April, July, October and December, for both heat and salt budgets. These months were chosen to represent the most important phases of the average seasonal cycle. In April, the layer is warming almost everywhere (dQ/dt>0) in response to atmospheric heat fluxes (Qatm). In July, the offshore is warming while the coastal zone is cooling. The average temperature decrease along the coast is forced by vertical and/or horizontal advection; either by the upwelling of subsurface colder waters, or by the southward flowing cold jet. The atmosphere warms the entire domain especially near the coast, due to higher air-sea temperature differences that drive stronger sensible heat fluxes. In October, the situation is the opposite: the atmosphere cools the entire domain (Qatm<0) while

advection of warmer waters from the south by the IPC contributes to a temperature increase of the shelf/slope. In December, the situation is similar but with lower advection, and stronger heat loss, contributing to a warming of the slope waters but at a slower rate.

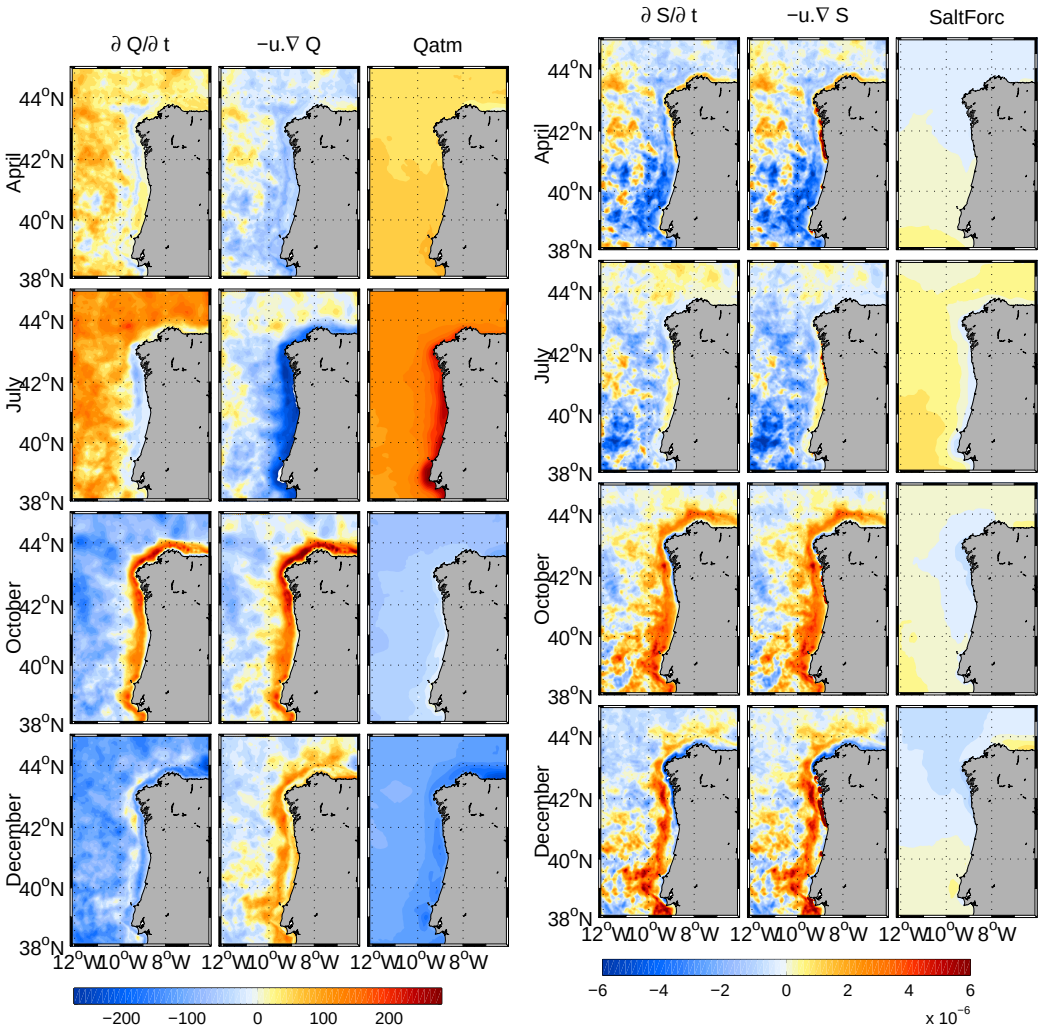

Figure 2.15: *Block on the left: global averaged heat fluxes (W m^{-2}) for April, July, October and December. The columns represent average time rate, advection and atmospheric forcing. Block on the right: the same, for salt fluxes(psu m s^{-1}).*

To compare the seasonal evolution of the heat budgets with the volume averaged temperature TW200 and TN200 presented in Fig. 2.13 (a,c), we integrated the heat budgets in the same domains N and W and represent the quantities in Fig. 2.16 a and c. The plot shows the time rate, advection and forcing and also, the sum of advection and forcing. The sum of advection and forcing is almost always coincident with the average heat rate, confirming that the sum of these contributions drives the seasonal cycle of the heat rate and that the mixing terms are negligible. The seasonal cycle of the heat budgets on the northern coast (domain N Fig 2.1) is displayed in Fig. 2.16 a). The time rate is positive from April to October, which means that the top 200 m of domain N warm during these months. This is in agreement with the TN200 seasonal cycle (Fig. 2.13 a) that reaches the annual maximum in October. The most important term is the atmospheric forcing since the time rate approximately follows its signal, but advection is not negligible. It compensates in part the warming of the atmospheric forcing in the summer and delays the autumn cooling by advecting warmer waters to the region (see Fig. 2.16 a - positive advection from September to December). On the west coast (Domain W), the seasonal cycle is less controlled by the atmospheric forcing (Fig. 2.16 c). In summer, the warming induced by the atmospheric fluxes is partly compensated by advection, and in July, advection balances the atmospheric heat input, explaining the curvature change obtained in TW200 seasonal cycle (Fig. 2.13 c). After September, the IPC brings warmer waters to the domain W (positive advection), compensating the otherwise cooling tendency. The interplay between advection and atmospheric fluxes explains the TW200 seasonal cycle on the west coast (Fig. 2.13 c), and its difference from the SST cycle, which approximately follows the atmospheric fluxes.

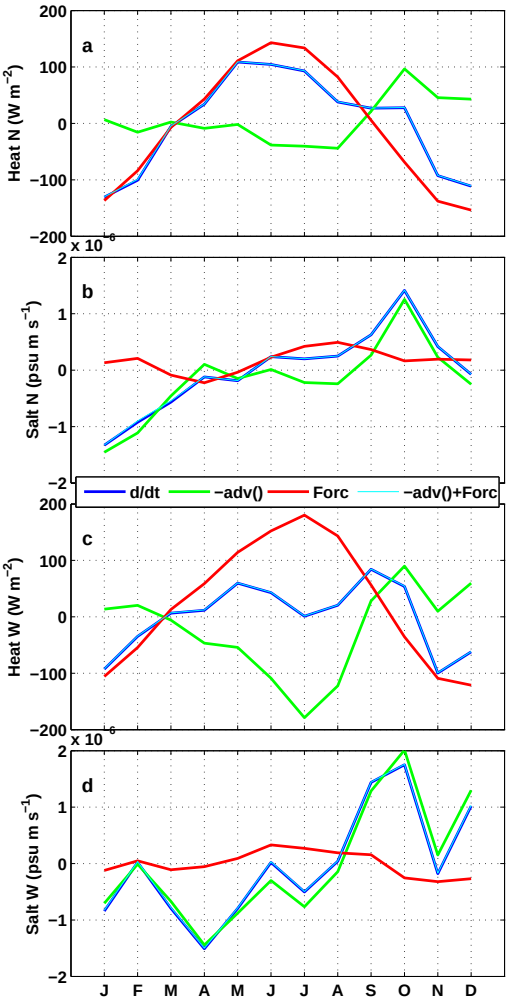

Figure 2.16: *Average seasonal cycle of volume averaged (top 200 m) heat and salt budgets for northern and western coast. (a) volume averaged heat equation terms (domain N); (b) volume averaged salt equation terms (domain N); (c) same as a, but for domain W; (d) same as b, but for domain W. In each subplot it is represented the time rate, advection, atmospheric forcing and sum of advection and atmospheric forcing.*

In the salinity budgets, advection controls the spatial structure of the salt rate for the various months (Fig. 2.15 b). In October and December, the salinity increases over the slope by advection. The seasonal cycle for the domains N and W are summarized in Fig. 2.16 b and d, respectively. On

domain N, the maximum salinity increase occurs in October, forced by advection (Fig. 2.16 b). On domain W, advection also dominates the seasonal cycle, increasing salinity in September, October and December, and decreasing it from January to July (Fig. 2.16 d). For both domains, in the northern and western coasts, it is confirmed that the winter circulation, dominated by the IPC, is of major importance in transporting salinity northwards.

2.5 Discussion and Conclusions

Our results present new information regarding the alongshore flows, their seasonal cycle, vertical structure, and importance in driving temperature and salinity seasonal variability. Poleward flows are present yearlong, but the vertical structure evolves, mainly by intensification and relaxation at different depths. To help with the discussion we present a scheme of the seasonal cycle of the alongshore flows in Fig. 2.17. The figure summarizes the main features of the sections I, II and III (Figures 2.5, 2.6 and 2.7). The IPC starts developing near the shelf break at around 200 m depth (Fig. 2.17 - August). After September, the IPC core becomes a surface intensified jet north of 41°N (Fig. 2.17 September-November). South of that latitude, the maximum is never shallower than 100 m depth yearlong. In December and January, the IPC reaches its maximum expression as a narrow and intense poleward flow, in the upper 250 m of the water column. At deeper levels, the IPSU core extends on average from 600 to 1200 m depth, and is present almost yearlong, with a small decrease in November. Over the slope, at about 400 m depth, the flow is weaker or equatorward from January to April (USCC). Over the shelf the current reverses seasonally. Under upwelling conditions it flows to the south (after April). In the winter, the combined effect of southerly wind episodes and river plumes, forces northward mean flow. The comparison with current meter data confirms the existence of these different cores. The data also confirms that the IPC intensifies near the surface from September to December and that the IPSU is minimum in

November. Our description of the vertical structure and seasonal cycle is in agreement with previous studies:

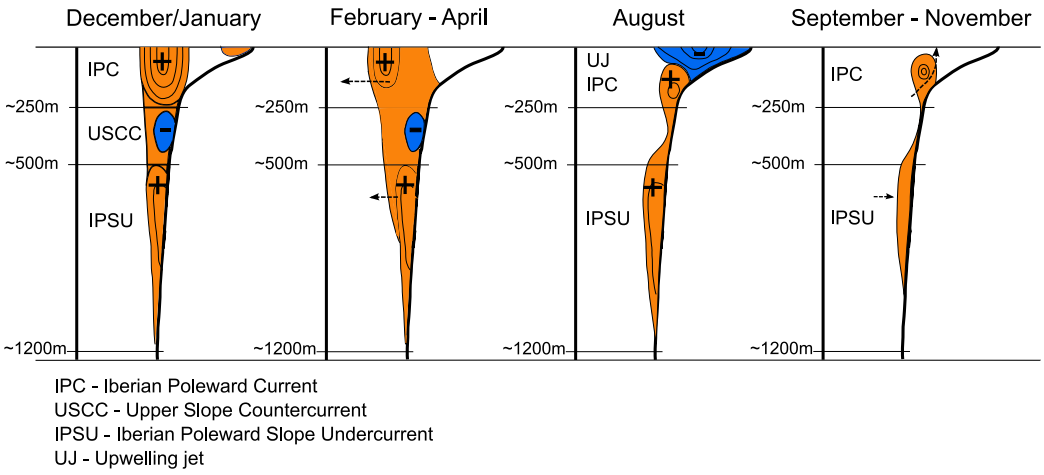

Figure 2.17: *Schematic representation of the seasonal cycle of the alongshore currents. Positive values (orange) correspond to northward flow, negative values (blue) to southward flow.*

1. The existence of two cores of poleward flow (IPC and IPSU - Fig. 2.17) was first suggested in Ambar and Fiúza (1994), that analyzed part of the current meter data set used in this paper. IPSU is described in Daniault et al. (1994).

2. The surface intensified core (IPC) in the winter months (see Fig. 2.17 - December/January) was first observed by Frouin et al. (1990) and was further studied for its conspicuous SST signature (Pingree and Le Cann, 1990, 1992b; Peliz et al., 2005; Garcia-Soto and Pingree, 2011).

3. The IPC intensification near the shelf break, at around 200 m depth, during the upwelling season (see Fig. 2.17 - August), was observed by Peliz et al. (2002), who presented hydrology observations from a section at 41°N (our section II) in September 1998. Under upwelling conditions over the shelf, they observed the presence of a higher salinity anomaly over the upper slope, with a subsurface maximum of salinity at around

80 m depth, indicating a poleward flow located just offshore/below the upwelling jet, similar to the near surface vertical structure we see in our results (Fig. 2.17 - August). Llope et al. (2006) also observed a double-core vertical structure of salinity in the Bay of Biscay, in January of 1999 and 2002, with two maxima of water intruding from the west coast. The deeper core is at the depths of the shelf break, suggesting that an intensified poleward current was present at or just before the observations. Le Cann and Serpette (2009) in a study of the Bay of Biscay (northern margin) in the autumn of 2006, also observed the presence of saline waters (originated off the western Iberia margin) confined to the upper slope (shelf break), not reaching the surface. They seeded drifters over the slope (with drogues at 200 m) and over the shelf (with drogues at 75 m) and observed that the former followed eastward trajectories, while the latter followed westward paths. Our results show a similar structure in the alongshore velocity sections on the west coast, as summarized in Fig. 2.17 - August.

4. The presence of the USCC at around 400 m depth (see Fig. 2.17 - December to April), was observed by Oliveira et al. (2004), in geostrophic velocity sections computed from temperature and salinity field observations at 41.3°N, on February 2000. The equatorward flow also appears in other numerical modeling studies (Peliz et al., 2003b; Friocourt et al., 2007, 2008b).

5. The weakening of IPSU in the wintertime (with minimum alongshore velocity in November) is consistent with the results from Prieto et al. (2013). They collected semiannual hydrological data from a section at 43°N from 2003 to 2010 and concluded that the Mediterranean Water vein is stronger and attached to the slope in the summer, while in winter it spreads offshore.

6. In what concerns the offshore zone, Fiúza et al. (1998) analyzed hydrological data from May 1993 at 41°N and 42°N, and showed the presence

of an offshore poleward current, centered at around 10.25°W. Section II (Fig. 2.6) shows positive velocities at these longitudes in May, corresponding to the eastern side of the average standing cyclonic cell C3. Section I (Fig. 2.5) also shows positive velocities (that correspond to the eastern side of the propagating cyclonic cell C1), but not exactly at the same longitude as those reported in Fiúza et al. (1998). In the model, the northward flow is displaced to the west 0.5°. Finally, Peliz et al. (2005) also observed a salinity maximum centered at around 11.5°W, in a section at 41.5°N in May of 1998 (see their figure 12). From the density field we can estimate that there is a poleward flow centered at around 11°W, that matches the eastern side of the standing cyclonic cell C3 (Fig. 2.2 - May).

To conclude, we show that there is an almost permanent average alongshore current over the slope, that is divided in 3 different cores. The Iberian Poleward Current (IPC), occupying the top 250 m, the Upper Slope Countercurrent (USCC), equatorward and centered at around 400 m depth and the Iberian Poleward Slope Undercurrent (IPSU), that extends from 600 m to 1200 m depth. The IPC starts developing near the shelf break at around 200 m depth, still during the summer months, when the shelf and upper slope is occupied by southward flow associated with the upwelling. At the end of the year (December and January), the IPC core migrates vertically, from the shelf break depths to the surface, becoming a surface intensified jet. From February to May, the current weakens and part of it propagates offshore. We also showed that the seasonal cycle of salinity, in the upper 200 m of the water column, is mainly controlled by the IPC on both northern and western coasts. The seasonal cycle of the temperature is forced by both the circulation (IPC and upwelling) and the local air-sea fluxes, which are more relevant on the northern coast.

Chapter 3

Seasonal Forcing of the Slope Currents

3.1 Introduction

The mechanisms that force the IPC are still not completely clarified. Peliz et al. (2003b) use idealized numerical experiments to show that forcing the slope zone with a surface intensified meridional density gradient characteristic of the region, results in the development of a surface intensified poleward current over the slope, in the upper 350 m of the water column, with a weak equatorward current developing just beneath. Friocourt et al. (2008b) use both analytical and numerical model approaches, of a 4-layer system, with meridional density gradients of alternating signs in depth, and reproduce a baroclinic system of slope currents with alternating directions, the surface one flowing poleward. The "Joint Effect of Baroclinicity and Relief" (JEBAR) (Huthnance, 1984) is the main driving mechanism in these two studies. On the other hand, Frouin et al. (1990), Le Cann and Serpette (2009) and Garcia-Soto and Pingree (2011) argue that southerly winds are important for the development of surface intensified events of the IPC.

The main questions addressed in this chapter are: 1) What are the important forcings of the IPC and how do they vary seasonally? 2) What is

the mechanism of formation of the USCC, the countercurrent that develops below the IPC?

3.2 Depth-averaged vorticity equation

In order to understand what mechanisms force the Iberian Poleward Current and what are the processes driving its seasonal variability, we computed the vorticity balances in the slope zone. Starting from the horizontal momentum equations with the Boussinesq approximation, the equations for the zonal and meridional velocities (u,v) are:

$$\begin{aligned} \frac{Du}{Dt} &= fv - \frac{1}{\rho_0}\frac{\partial p}{\partial x} + \frac{1}{\rho_0}\frac{\partial \tau^x}{\partial z} \\ \frac{Dv}{Dt} &= -fu - \frac{1}{\rho_0}\frac{\partial p}{\partial y} + \frac{1}{\rho_0}\frac{\partial \tau^y}{\partial z} \end{aligned} \tag{3.1}$$

Taking the depth average of the set of equations 3.1 and then cross differentiating, we obtain a vorticity equation of the depth-averaged flow ($\hat{\xi}$):

$$\begin{aligned} \hat{\xi}_t \;+\; \vec{\nabla}_h \times \overline{adv} = & -\beta\overline{v} + \frac{f}{H}\left[\overline{u}\frac{\partial H}{\partial x} + \overline{v}\frac{\partial H}{\partial y}\right] + J(\chi, H^{-1}) \\ & + \frac{1}{\rho_0 H}\vec{\nabla}_h \times \tau^w + \frac{1}{\rho_0 H}\left[\frac{1}{H}\left(\frac{\partial H}{\partial y}\tau_x^w - \frac{\partial H}{\partial x}\tau_y^w\right)\right] \\ & - \frac{1}{\rho_0 H}\vec{\nabla}_h \times \tau^b - \frac{1}{\rho_0 H}\left[\frac{1}{H}\left(\frac{\partial H}{\partial y}\tau_x^b - \frac{\partial H}{\partial x}\tau_y^b\right)\right] \end{aligned} \tag{3.2}$$

where ($\vec{\nabla}_h\times$) is the vertical component of the curl ($\hat{k}.\vec{\nabla}\times$), adv are the advective terms, J is the Jacobian operator, τ^w is the wind stress, τ^b the bottom stress, the overbars represent vertical average, the subscript t (e.g. $\hat{\xi}_t$) stands for time derivative, η is the surface elevation, H is bottom depth,

$$\hat{\xi} = \frac{\partial \overline{v}}{\partial x} - \frac{\partial \overline{u}}{\partial y}$$

$$(\overline{u}, \overline{v}) = \int_{-H}^{\eta} (u, v) dz$$

$$\chi = \frac{g}{\rho_0}\int_{-H}^{\eta} z\rho dz$$

$$\begin{aligned}\vec{\nabla}_h \times \overline{adv} &= \frac{\partial}{\partial x}\left[\frac{1}{H}\int_{-H}^{\eta}\left(u\frac{\partial v}{\partial x}+v\frac{\partial v}{\partial y}\right)dz\right] \\ &\quad -\frac{\partial}{\partial y}\left[\frac{1}{H}\int_{-H}^{\eta}\left(u\frac{\partial u}{\partial x}+v\frac{\partial u}{\partial y}\right)dz\right]\end{aligned}$$

Just rearranging the terms, we get:

$$\begin{aligned}\beta\overline{v} &= -\hat{\xi}_t + \frac{f}{H}\left[\overline{u}\frac{\partial H}{\partial x}+\overline{v}\frac{\partial H}{\partial y}\right] + J(\chi, H^{-1}) \\ &\quad +\frac{1}{\rho_0 H}\left[\frac{1}{H}\left(\frac{\partial H}{\partial y}\tau_x^w - \frac{\partial H}{\partial x}\tau_y^w\right)\right] \\ &\quad +\frac{1}{\rho_0 H}\vec{\nabla}_h \times \tau^w - \vec{\nabla}_h \times \overline{adv} \\ &\quad -\left[\frac{1}{\rho_0 H}\vec{\nabla}_h \times \tau^b + \left[\frac{1}{H}\left(\frac{\partial H}{\partial y}\tau_x^b - \frac{\partial H}{\partial x}\tau_y^b\right)\right]\right]\end{aligned} \tag{3.3}$$

The same procedure was followed in Guo et al. (2003), Mertz and Wright (1992), Huthnance (1984) and Lee et al. (2001). Couvelard et al. (2008) and Holland (1973) obtained the vorticity equation by taking the curl of the depth-integrated instead of the depth-averaged momentum equations. Following this alternative procedure, different terms are obtained, but the results are compatible as demonstrated in Mertz and Wright (1992).

Although we used equation 3.3, to facilitate the interpretation of the various terms and to understand how they interplay to force a meridional ($\beta\overline{v}$) depth averaged slope flow, we assume an idealized situation of a meridionally oriented slope $\left(\frac{\partial H}{\partial y}\right) = 0$ with a meridionally oriented wind stress ($\tau_x^w = 0$). The equation reduces to:

$$\begin{aligned}\beta\overline{v} &= -\hat{\xi}_t + \frac{f}{H}\left[\overline{u}\frac{\partial H}{\partial x}\right] + \frac{g}{\rho_0 H^2}\frac{\partial H}{\partial x}\frac{\partial}{\partial y}\left[\int_{-H}^{\eta} z\rho dz\right] \\ &\quad -\frac{1}{\rho_0 H^2}\left(\frac{\partial H}{\partial x}\tau_y^w\right) \\ &\quad +\frac{1}{\rho_0 H}\frac{\partial \tau_y^w}{\partial x} - \vec{\nabla}_h \times \overline{adv} \\ &\quad -\left[\frac{1}{\rho_0 H}\vec{\nabla}_h \times \tau^b - \left[\frac{1}{H}\left(\frac{\partial H}{\partial x}\tau_y^b\right)\right]\right]\end{aligned} \tag{3.4}$$

The terms in equations 3.3 and 3.4 represent:

1. the planetary vorticity advection (VBeta);
2. the rate of change of relative vorticity of the depth-averaged flow (Vrate);
3. the topographic vortex Stretching (Stretching). For the idealized situation (equation 3.4), since $\partial H/\partial x < 0$, the sign of the stretching term depends on the sign of the depth-averaged cross isobath flow $\overline{u}$. For example in the case of an inviscid barotropic flow, an eastward cross-isobath flow would cause water column compression and reduction of total vorticity;
4. the Joint Effect of Baroclinicity and Relief (JEBAR) (Huthnance, 1984) represents the effect of the density field in the depth-averaged current. In the idealized case, in the presence of a positive meridional density gradient, JEBAR will act as a positive contribution to the planetary vorticity term (note that z is negative), resulting in northward flow in a stationary state;
5. the wind slope induced torque (WindSIT) is related to the different responses experienced by different thickness water columns when subjected to a constant wind stress. In our idealized case, the variability of this term is only dependent on the alongshore component of the wind stress. A positive τ_y^w (southerly winds) will result in WindSIT giving a positive contribution to the poleward flow;
6. the wind stress curl (WSCurl);
7. the curl of the depth-averaged advection terms (TAdvec);
8. the total effect of bottom friction (BottomS), that includes the bottom stress curl and the bottom slope induced torque (the bottom slope induced torque was introduced by Lee et al. (2001)) and is related to the effect that a constant bottom stress will exert on different thickness water columns.

The momentum terms of the set of equations 3.1 were computed and stored during the model simulation so that the vorticity equation is balanced. We computed the vorticity budgets and then horizontally integrated over the slope area between 40-43°N and the isobaths of 200 and 1200 meters (area is shown in cyan blue in Fig. 3.1).

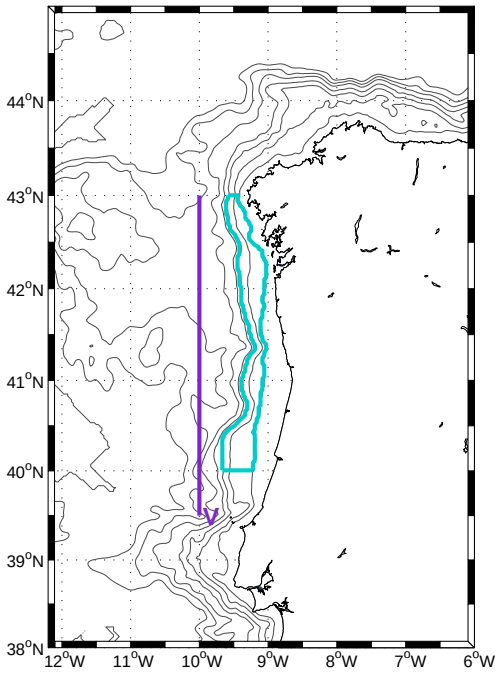

Figure 3.1: *The cyan blue zone over the slope is used to compute area integrated vorticity budgets. Section V will be referred in the text. The gray contours represent the isobaths of 100, 200, 500, 1000, 2000, 3000, 4000 and 5000 m.*

3.3 Time-mean balance

Table 3.1 presents the area-integrated and time-averaged terms of the vorticity equation. Vrate is negligible due to the long averaging period. The terms on the right side of the vorticity equation 3.3 can be evaluated for their contribution to the mean meridional transport (VBeta). VBeta is positive since the depth-averaged meridional velocity is poleward almost all year long.

VTERM	GlobAVG
$VBeta =$	0.33
$-Vrate$	0.002
$+Stretching$	-6.00
$+JEBAR$	9.94
$+WindSIT$	-2.75
$+WSCurl$	0.84
$+TAdvec$	0.94
$+BottomS$	-2.64

Table 3.1: *Global time average of area-integrated values of all terms in equation 3.3 (m^2s^{-2}) - terms are multiplied by 10^{12}. The area of integration is shown in figure 3.1 (cyan line)*

JEBAR is by far the dominant forcing term and together with WSCurl and TAdvec, these are the only terms that give average positive contributions to the poleward flow (although the latter two are much smaller). The other terms compensate this positive contribution (essentially of JEBAR): Stretching, WindSIT and BottomS. Although these terms differ in magnitude, none of them is negligible, suggesting a complex interaction between the various forcings on the slope.

3.4 Seasonal cycle of integrated vorticity terms

The seasonal evolution of the area integrated (the slope area in Fig. 3.1) monthly-averaged terms of the vorticity equation (3.3) is presented in Fig. 3.2. A similar procedure was taken by Guo et al. (2003). VBeta and the Net transport are shown in a separate plot (the net transport is the average of sections I, II and III slope transport, across areas A and B, in Fig. 2.5, 2.6 and 2.7 - the same as represented in dashed-dotted line on Fig. 2.11).

Vbeta is high in January and February, then decreases to nearly zero from April to July (with a weak inversion to southward flow in April and July).

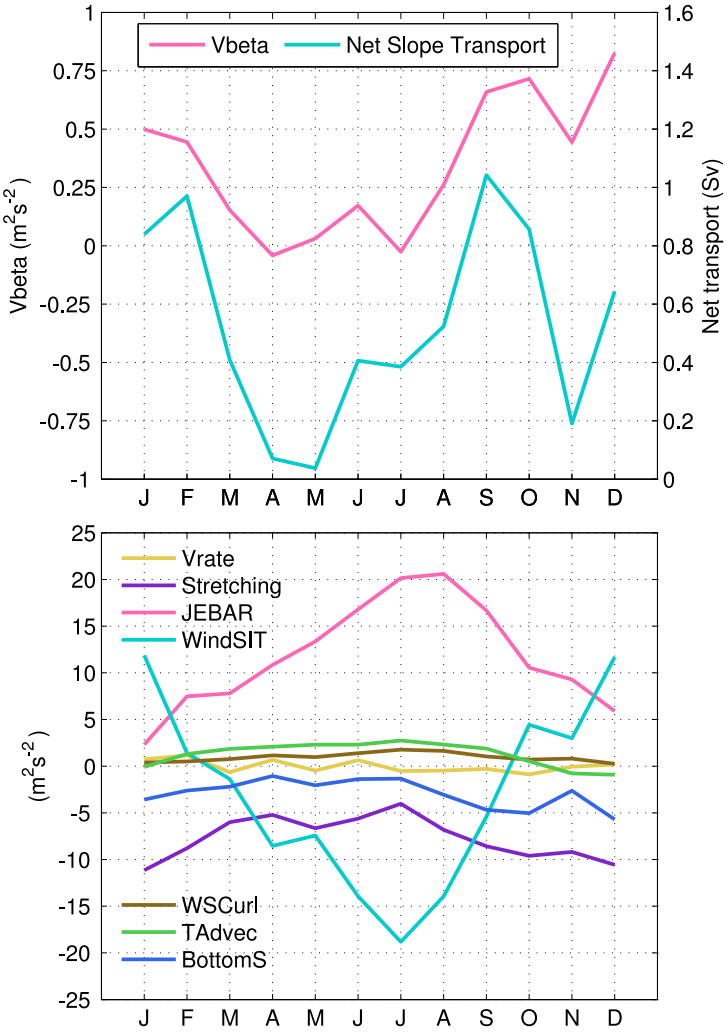

Figure 3.2: *Seasonal cycle of area-integrated values of all terms in Equation 3.3 ($m^2 s^{-2}$) - monthly averages (terms are multiplied by 10^{12}). The area of integration is shown in figure 3.1 (cyan line). The plot on the top represents Vbeta and the net slope transport (the same as the dashed-dotted line on Figure 2.11). The plot on the bottom presents the terms from the right side of the equation - Vrate, Stretching, JEBAR, WindSIT, WSCurl, TAdvec and BottomS. Note that the scales of the vertical axes are different.*

The seasonal cycle is similar to that of the net transport. In July, it starts increasing reaching a first peak in September/October and the maximum in December, after a small decrease in November. The contribution of the different terms to the monthly balance has been analyzed in search for the main contributors to the seasonal cycle of the Vbeta term. It is not possible to establish cause-effect relationships between VBeta and changes in the forcings (JEBAR, WindSIT, Stretching, BottomS, WSCurl), because Vrate and TAdvec are not negligible. Nevertheless, the latter terms are much smaller than the large amplitude forcing terms, making it possible to analyze the relative role of the forcing terms. JEBAR is on average the strongest term almost year long (bottom subplot in Fig. 3.2), reaching a maximum in the summer and decreasing in winter, when the poleward flow reaches its maximum intensity. During the period from August to January, the poleward flow changes to a surface intensified current (see Figures 2.5-2.7 and discussion in subsection 2.2.2). The main contribution in August is from JEBAR. WindSIT, Stretching and BottomS are negative, but do not balance the positive contribution of JEBAR suggesting that the deep poleward flow in that month is mainly driven by JEBAR. In September, despite the decrease in JEBAR, WindSIT increases (although still negative) compensating to a less degree the positive contribution from JEBAR and resulting in an intensification of the poleward flow. In October, JEBAR decreases markedly, but the WindSIT becomes positive and almost half the magnitude of JEBAR. The contributions of both terms maintain the poleward flow in October, when it reaches a first maximum. In November, Vbeta decreases, following a decrease of WindSIT and JEBAR. December corresponds to the month of maximum poleward flow intensity and it is also the time when the jet is strongly intensified near the surface (Fig. 2.5-2.6). In what concerns the vorticity terms, WindSIT increases again, reaching a value close to its yearly maximum (that happens in January), and JEBAR continues decreasing. This means that the main positive contribution in December is of WindSIT, suggesting that it is the term responsible for the December-January surface intensified max-

imum. In January, JEBAR is close to zero, and WindSIT becomes the main contribution to poleward flow. The small decrease in intensity of VBeta from December to January may be associated with the decrease of JEBAR. Note, however, that during these months, the contribution of stretching and TAdvec cannot be ruled out (BottomS co-varies with the velocity).

To summarize, the relative role of each term in the vorticity balance varies from month to month. Nevertheless, JEBAR guarantees the major contribution to the poleward flow and explains its existence almost all year long, including the summer months. The surface intensification of the poleward flow during the months of December-January, seems to be a response to the intensification of WindSIT. WindSIT variability depends on the alongshore component of the wind stress, which is on average positive (southerly) from October to January, reaching a maximum of intensity in December-January.

3.5 Flow structure

It was shown in chapter 2 that the alongshore flow presents a clear vertical structure that also varies from month to month. The vorticity balances are applied to vertically integrated flow and therefore cannot explain the vertical structure. However, together with the vertical structure, the flow also displays a clear cross-shore variability. The cross-shore structure of vorticity equation terms was obtained in order to search for relations with the main cores of the alongshore flows: IPC, IPSU and USCC. We calculated the vorticity terms along each isobath from 40 to 43°N and then averaged (along the isobath). The terms are plotted as function of depth together with the alongshore velocity sections (as function of depth too) in Fig. 3.3. We focus on the months of August to December, the period of intensification of the IPC.

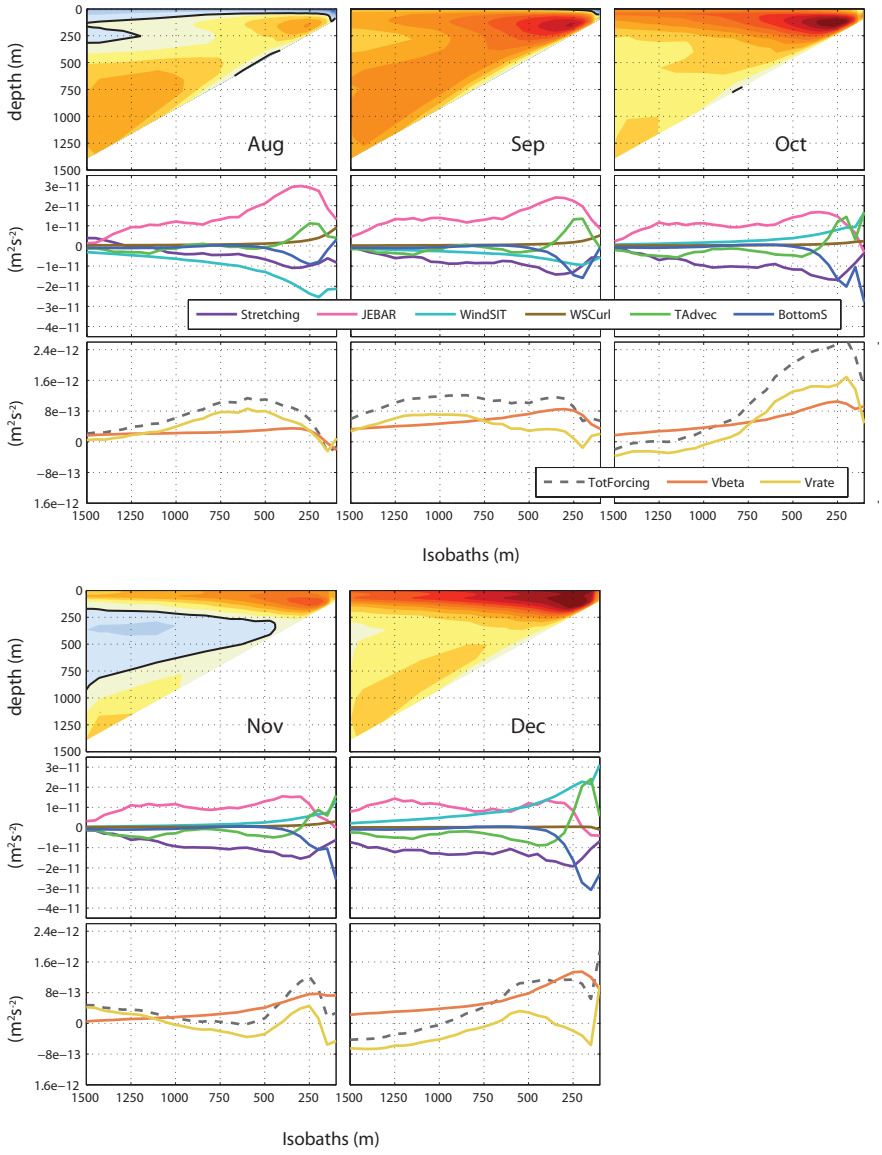

Figure 3.3: *August to December cross-structure monthly means. First row: alongshore velocities at 41°N (same as Figure 2.6 but in function of depth - the color scales are similar to Figure 2.6). Second row: along-isobath average (40 to 43°N) of Stretching, JEBAR, WindSIT, WSCurl, TAdvec and BottomS. Third row: along isobaths average of Vbeta, Vrate and the total forcing (sum of all terms from the second row).*

The IPC is located in the upper 250 m of the water column, approximately

between the isobaths of 100 and 500 m (see velocity sections on the 1^{st} row of Fig. 3.3). In August, JEBAR is maximum and is the main term forcing the IPC, compensated in part by WindSIT, stretching and BottomS (see 2^{nd} row of Fig. 3.3). Advection terms are important at the core of the IPC with a maximum over the 250-m isobath. Note that WSCurl starts becoming more important over the shelf. From August to October, WindSIT changes from negative to positive, explaining the intensification of the IPC. The total forcing over the upper slope reaches a maximum in October (Fig. 3.3 3^{rd} row). In November, the total forcing decreases substantially (due to a decrease in both JEBAR and WindSIT) resulting in a relative weakening of the IPC. In December, the IPC reaches the maximum intensity in response to WindSIT and Advection terms (that are maximum at the core while JEBAR becomes negative).

The IPSU is the deeper current at the Mediterranean Water levels and is located approximately between the isobaths 500 and 1200 m. In general JEBAR is weaker at these depths, due to its dependence on $1/H^2$ (see equation 3.4) but it is still the dominant positive term, suggesting that it may be the forcing mechanism for the IPSU. It increases in September timely with the intensification of the IPSU, followed by a decrease in October and November, when IPSU reaches a minimum. In December, JEBAR increases slightly again and WindSIT becomes positive, coincident with an increase in IPSU intensity.

The JEBAR minimum in December/January discussed in the previous section, is limited to the upper 500 m of the slope, since over the deeper slope the changes are much weaker and the JEBAR is not minimum in December (Fig. 3.3 - 2^{nd} row).

The cross-shelf analysis of the terms does not help in explaining the USCC because it is located under the IPC that is much more intense. To understand its seasonality we computed the geostrophic flow structure from the density average field using the thermal wind equation. The velocity field was integrated from the surface and the surface velocity was obtained from the

sea surface height gradient. This estimate is shown in Fig. 3.4 2^{nd} row, for section I (Fig. 2.1). There is a good match between the geostrophic velocity sections and the mean absolute velocity sections (Fig. 3.4 - 1^{st} row), confirming that the currents are mostly in geostrophic balance and that the mean vertical velocity structure seasonality can be explained by the evolution of the internal density field. The USCC is visible in November and January, both in the mean meridional velocity section and in the velocity fields obtained from the density structure (the core of USCC extends vertically from approximately 250 m to 500 m depth). On the top 350 m of the water column, the cross-shore density gradient $\partial\rho/\partial x$ is mainly negative (eg. 4^{th} row January plot on Fig. 3.4), because the IPC advects less dense water northwards over the slope. This density gradient forces a decrease of the meridional geostrophic velocity in depth, that eventually becomes negative. This is probably the reason why a southward current (the USCC) develops below the IPC core.

In November there is a decrease of intensity of the alongshore velocity in the whole water column and even an inversion with the emergence of the USCC. This follows a decrease in the total forcing from October to November, due to a decrease in both JEBAR and WindSIT (Fig. 3.3). Although the vertical structure of the alongshore currents seems so different in November, this decrease is only in the barotropic velocity intensity. The baroclinic structure does not change much from October to January (see Fig. 3.4 - 3^{rd} row, where the vertical average was removed at each point). This suggests that the anomaly in November and the development of the USCC is an answer to the decrease in the barotropic forcing. Also between December and January the density gradient stays nearly the same, but there is a decrease in intensity in the whole water column allowing the USCC to emerge.

At deeper levels, the cross-shore density gradient becomes positive (from around 400 m to 1000 m depth - Fig. 3.4 - 4^{th} row). From the thermal wind equation, meridional velocity will increase with depth in agreement with the core of the IPSU. The change of sign of the cross-shelf density gradient

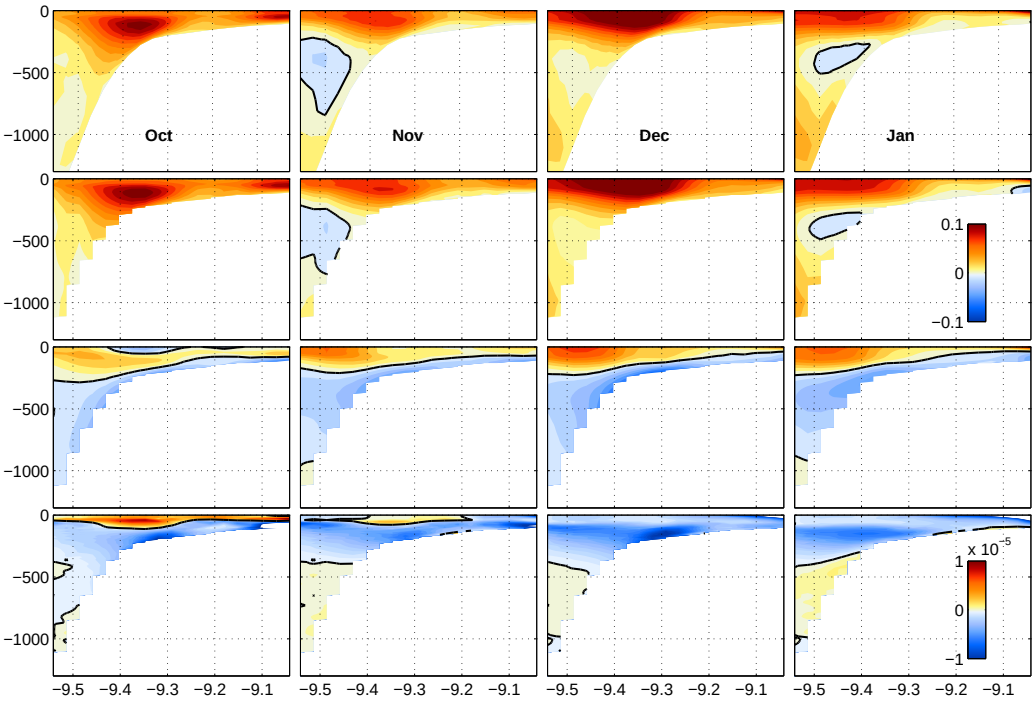

Figure 3.4: *August to January monthly means vertical sections at 42.2° N (latitude of section I on Figure 2.1). First row: meridional velocity (same as Figure 2.5, but zoomed only in the slope - m s^{-1}). Second row: meridional velocity obtained by the thermal wind equation (density field). Third row: baroclinic meridional velocity structure (the vertical average was removed at each point from the fields in the second row). Fourth row: zonal density gradient $\partial\rho/\partial x$ (kg m^{-4}) (negative values mean ρ decreases to the coast).*

with depth may be explained by the existence of an inversion in the large scale meridional density gradient. Fig. 3.5 shows the time-mean meridional density gradient for section V (see map in Fig. 3.1), averaged in time for the whole time period of the simulation. The figure shows that the mean meridional density gradient is positive in the top 400 m of the water column and negative from 400 to 900 m depth.

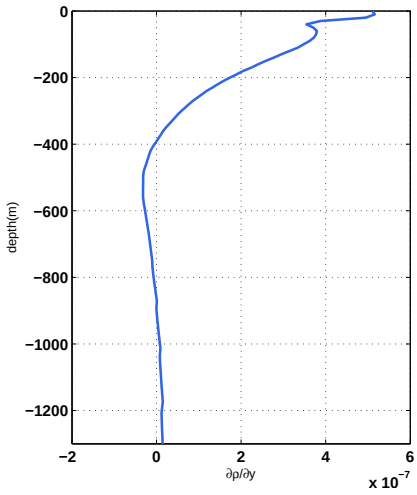

Figure 3.5: *Mean meridional density gradient (kg m^{-4}) obtained in section V (see location in Figure 3.1)*

3.6 Discussion and Conclusions

The vorticity balances over the slope confirm the importance of JEBAR in the forcing of the IPC. Its contribution is higher in summer than in winter, but the cross-shore analysis shows that JEBAR decreases substantially at the core of the IPC, where the advection terms become relevant. This suggests that it is the northward density advection that diminishes JEBAR by eroding the meridional density gradients. Offshore, the meridional density gradients at the IPC depths are more intense in winter, reaching a maximum in December/January (not shown) as already suggested in Peliz et al. (2005). In December and January, the IPC receives a major contribution from the southerly wind forcing (windSIT), which is in agreement with the studies of Le Cann and Serpette (2009) and Garcia-Soto and Pingree (2011). The former describes a surface intensified IPC event (with strong thermal signal) in the autumn-winter 2006-2007, that happened during intense southerly winds. The latter shows that events of anomalous high sea surface temperature in winter, on the west coast at 42°N, occur under the presence of southerly winds. In August, the IPC core is intensified near the shelf break (and not

at the surface) because of the presence of opposing northerly winds (negative WindSIT in Fig. 3.2), that drive the southward upwelling jet. After September, the meridional wind stress becomes positive allowing the IPC core to surface. Peliz et al. (2003a) present an idealized experiment to study the response of a slope density-driven poleward current to wind forcing. They verified that a well established poleward surface current under the action of northerly winds, diminishes its intensity and its core is displaced offshore, but it does not become an undercurrent. In our results the northerly winds are already set, when the JEBAR term becomes significant. For that reason the IPC starts developing as an undercurrent, near the shelf break.

At the IPC core, the advection of vorticity becomes important, suggesting that temperature and salinity advection, and consequently density advection, may become important too, in the presence of meridional density gradients. It is known that the IPC advects temperature and salinity northward along the western Iberian Coast, as was shown in chapter 2. As shown in Fig. 3.5, there is a strong large scale positive meridional density gradient, in the upper 400 m of the water column. This means that advection of less dense waters from the south to the north over the slope, will result in the onset of a negative cross-shore density gradient, that by thermal wind produces a positive vertical shear of the meridional velocity. Consequently, the IPC will decrease with depth and eventually become negative. This process should explain the existence of a negative current, the USCC, under the IPC core. Peliz et al. (2003b) and Peliz et al. (2003a), force a slope current with a meridional density gradient (JEBAR) in a two layer density structure and also obtain an equatorward flow under the surface poleward current.

The large scale meridional density gradient becomes negative from 400 m to around 900 m depth (Fig. 3.5). The presence of a positive cross-shore density gradient at these depths (see Fig. 3.4 last row) indicate that IPSU advects this anomaly northward, along the Iberian slope. These meridional gradients of alternating signs were already described by Friocourt et al. (2008b). They impose these meridional density gradients in a four layer density struc-

ture in analytical and idealized numerical studies and obtain a four-layer slope current system, with alternating positive and negative velocities between consecutive layers.

To conclude, we confirm that JEBAR is the most important forcing mechanism of the slope current, but as advection terms become important, the northward density flux diminishes the meridional density gradients, resulting in a decrease of JEBAR at the core of the IPC. In December and January, there is an important contribution for the IPC from the positive wind stress (southerly winds) over the slope.

Chapter 4

Interannual Variability of the Iberian Poleward Current

4.1 Introduction

As was discussed in chapter 2, the IPC starts developing near the shelf break during the summer and intensifies after September reaching a maximum in December/January when it becomes a surface intensified jet. This jet is typically associated with a sharp warm SST signature, characterized either by a thin patch along the slope, or by a broader unstable flow. In some years the SST signature seems to be absent.

These year-to-year changes in winter SST anomaly (usually taken as an index for the IPC strength) motivated numerous studies (Garcia-Soto et al., 2002; Garcia-Soto, 2004; Llope et al., 2006; Peliz et al., 2005; Le Cann and Serpette, 2009; Le Hénaff et al., 2011; Garcia-Soto and Pingree, 2011). Most of these studies focused on identifying anomalously intense IPC winters by analyzing satellite sea surface temperature (SST) (Garcia-Soto et al., 2002; Garcia-Soto, 2004; Peliz et al., 2005). Other studies analyzed monthly CTD samplings of temperature and salinity (Llope et al., 2006) and coastal altimetry products, which provide information of the geostrophic alongshore velocities on the northern coast (Le Hénaff et al., 2011). However, the mech-

anisms behind the interannual variability of the IPC and of its thermohaline signature, are still not fully understood. In some years, anomalous temperatures coexist with anomalous salinities, which is an expected behavior, since stronger IPC events should transport warm and salty waters northward. However, this is not always true, and warm anomalies were reported to co-occur with fresh water anomalies (Llope et al., 2006; Le Cann and Serpette, 2009). It is also not clear what forces the year-to-year variability of the IPC intensity and its response in terms of temperature and salinity anomalies. Garcia-Soto et al. (2002); Garcia-Soto and Pingree (2011) found that the winter warming off the northern Iberian Coast is negatively correlated with NAO index of the preceding months. On the other hand, Llope et al. (2006) found no significant correlation between salinity anomalies in the northern coast and the NAO index.

The objectives of this chapter are to better understand the variability of the IPC and its role in the heat and salt fluxes along the Iberian margin. The main questions are: 1) What forces the interannual variability of the IPC transport? 2) How does the variability of the IPC intensity affect temperature and salinity anomalies in the western and northern coasts? 3) Why are temperature and salinity anomalies in anti-phase, on the northern coast, in some winters?

4.2 Comparison of model results with previous studies

Most of the previous studies on the interannual variability of the IPC were based on the analysis of satellite SST data and our model reproduces the main events described. Garcia-Soto et al. (2002); Garcia-Soto (2004) identified the anomalous IPC winters in the northern coast, by increasing order of SST amplitude: 2000-2001, 2002-2003, 1989-1990, 1997-1998 and 1995-1996. Le Cann and Serpette (2009) added to this sequence the winter of 2006-2007. The years identified in literature as having temperature anomalies

are represented in Fig. 4.1 a) with red or blue squares, for warm and cold anomalies. We represent the SSTN and SSTW interannual anomalies (the same as in Fig. 1.6) in Fig. 4.1 (a and c). In our results, on the northern coast, the 4 winters with strongest positive anomalies are 1989-1990, 1995-1996, 1997-1998 and 2006-2007 (see Fig. 4.1 a), in agreement with these studies. There are also positive anomalies, although weaker, in 2000-2001, 2002-2003 and 1994-1995, both in model results and satellite SST, although the latter has not been referred. In Fig. 4.1 a), we show the years we have with temperature anomalies in the model with a "T" in red or blue, respectively for warm or cold anomalies. The winter 1994-1995 was not described as anomalous in previous studies, but we obtain a warm positive anomaly in the monthly averages of both model and satellite SSTs, so the reason for this difference may be methodological. On the west coast, Peliz et al. (2005) classify as strong IPC winters: 1989/1990, 1995/1996, 1996-1997, 1997/1998 and 2000/2001, that are identified with red squares in Fig. 4.1 c) (their analysis finishes in 2001). These years are coincident with the ones we identify as anomalously warm, with the exception of 1996/1997, when we obtain negative anomalies both for model and satellite SST. This is because they analyzed January and February 2-month average, and in February 1997 there is the development of a positive anomaly in both northern and western coasts (Fig. 4.1 a,c). We did not consider this winter as anomalous, because we are focusing on the period of September to January.

4.3 Description of the Interannual variability

To analyze the interannual variability we computed time series of monthly averages of SSTN, TN200, SN200, SSTW, TW200, SW200 (SST and upper 200 m volume averaged temperature and salinity, for both domains W and N represented in Fig. 2.1). We also computed VW200 (northward transport in the top 200 m of the water column, in domain W). For a better visualization of the interannual variability we describe the anomalies (Fig. 4.1) instead of

the absolute monthly averages. The monthly anomalies are computed by removing the average seasonal cycle of each variable (represented in Fig. 2.13). On the average seasonal cycle, the IPC starts during the summer months and persists till January/February (as described in chapter 2). Consequently, a negative anomaly in Fig. 4.1, does not necessarily mean that there was no IPC on that year, it just indicates that it was weaker than the average.

The co-variation of the different variables is not straightforward (Fig. 4.1). The anomalies in the area averaged SST show similar signals to the anomalies in the volume-averaged temperature, although the amplitudes of the former are higher (Fig. 4.1 a, c). The SSTN anomalies have a correlation of 0.77 with TN200 anomalies (statistically significant at 5% level) (see the time series of both in Fig. 4.1 a). On the west coast, the correlation between SSTW and TW200 is 0.76 (statistically significant at 5% level).

There is no clear relation between years with strong transport and years with high temperature or salinity anomalies. The anomalies of VW200 (average northward transport in the top 200 m along the west coast - Fig. 4.1 e) are significantly but weakly correlated with the time series SSTW, TW200 and SW200 (0.29, 0.25 and 0.21, respectively, statistically significant at 5% level). The correlations between VW200 and temperature and salinity on the northern coast (TN200, SN200), are not significant. On the other hand, there is a stronger correlation between temperature and salinity on the northern coast and on the western coast. The correlation between SSTW and SSTN anomalies is 0.72. TN200 and TW200 (Fig. 4.1 a and c) present a correlation of 0.82. SN200 (Fig. 4.1 b) is significantly correlated only with SW200 (0.64; Fig. 4.1 d). However, SW200 is also correlated with TW200 (0.63).

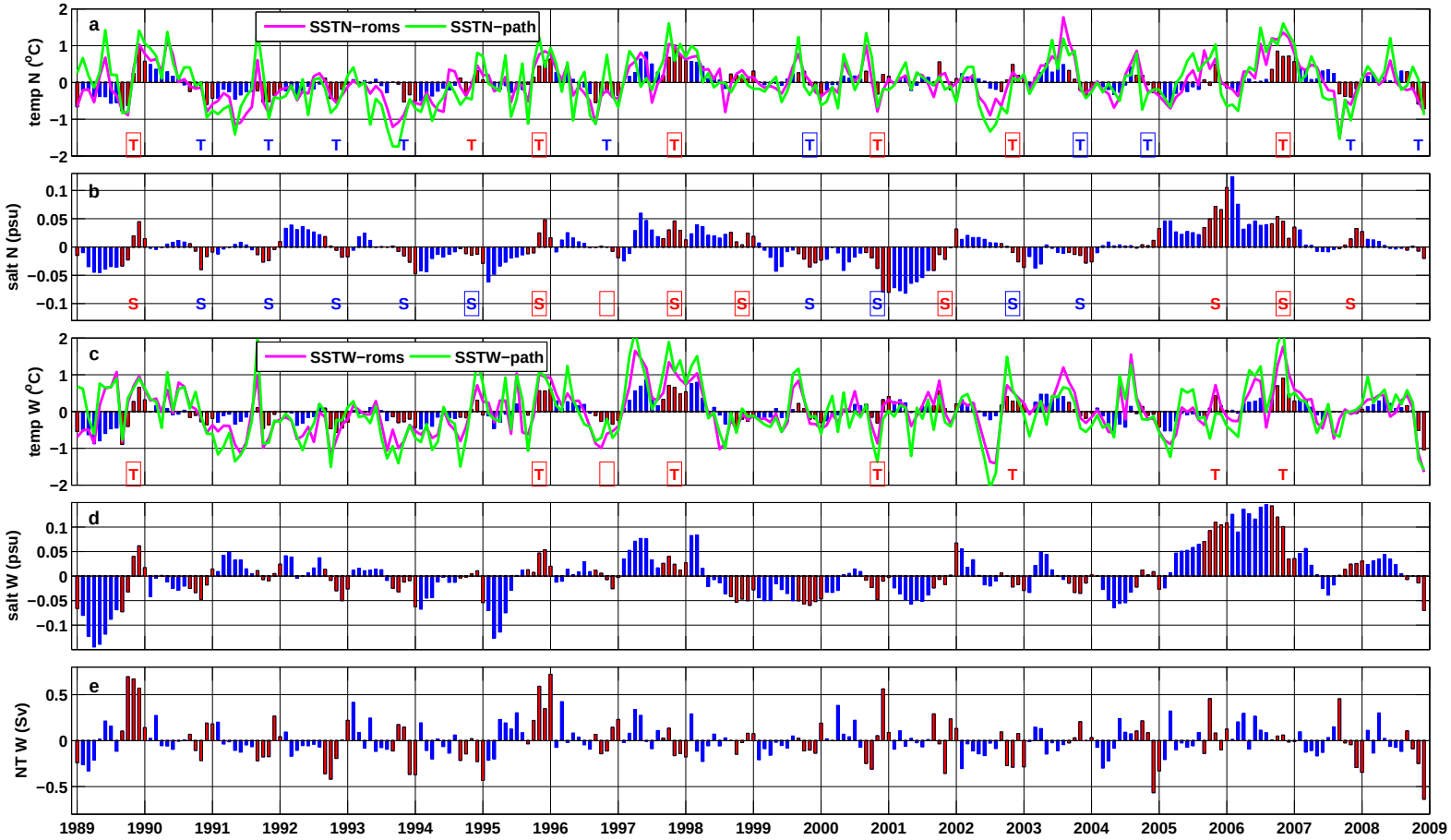

Figure 4.1: *Time series of anomalies, after removing the seasonal signal presented in Fig. 2.13. (a) volume averaged temperature in the upper 200 m (TN200) (model) and SST (model and satellite), averaged in domain N (see Fig. 2.1); (b) volume averaged salinity in the upper 200 m (SN200) (domain N); (c) TW200, the same as a, but for domain W; (d) SW200, the same as b, but for domain W; (e) average northward transport in the upper 200 m and in domain W (VW200). "T", "S" and the "squares" represent temperature and salinity anomalies, positive in red and negative in blue; the letters are model results, the "squares" descriptions from previous studies.*

For example, the positive anomaly in the end of 1989 in temperature and salinity seems to be associated with a strong northward transport on the west coast. The same seems to happen in the end of 1995. In the winter 2000-2001, from November to January, the transport is above the average and there is a positive temperature anomaly, but the salinity anomaly is negative. In the end of 2005, outstanding positive salinity anomalies are observed, but the northward transport is around the average. A similar case happens in the end of 2006 when positive anomalies in temperature and salinity are recorded, but the transport is within the average values. In the next section, we will explore the nature of these differences.

4.3.1 Year-to-year IPC changes

To illustrate the complex relations between anomalies of northward transport, temperature and salinity, we focus on four different winters (1995/1996, 2000/2001, 2005/2006 and 2006/2007), due to their different characteristics. Figures 4.2 and 4.3 show vertical sections (section IV on Fig. 2.1) of alongshore velocities together with, respectively, temperature and salinity. The interannual differences are easier to observe in the salinity vertical sections; temperature anomalies are more difficult to identify because of the strong vertical structure and seasonal cycle.

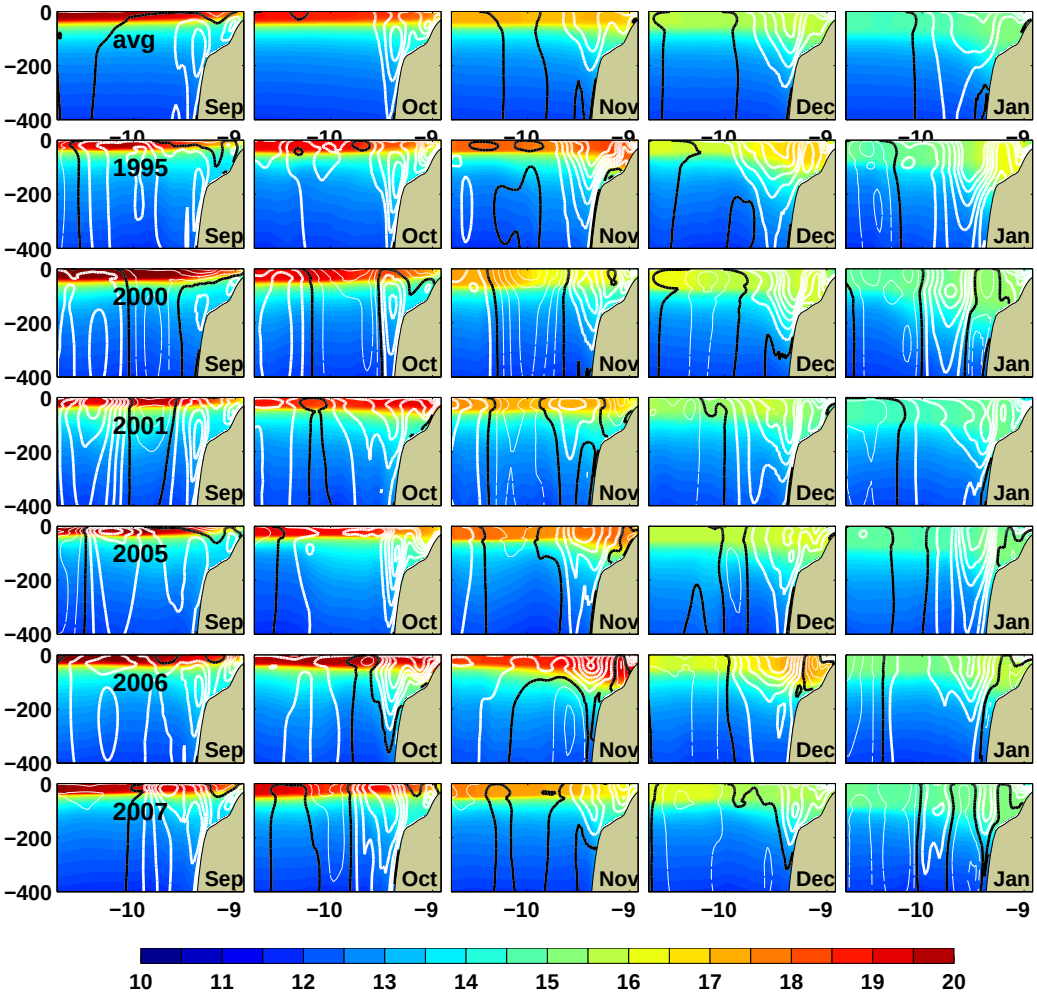

Figure 4.2: *Vertical sections of meridional velocities (m s^{-1}) in contours and temperature (°C) in colors. The various columns correspond to different months. The first row is the average of all the 20 years of simulation (same as Fig. 2.14), the following rows correspond to anomalous years, indicated in the figure. The velocity contours have an interval of 0.03 m s^{-1}; positive values are displayed on a thick white line, negative on a thin white line, and zero is in black.*

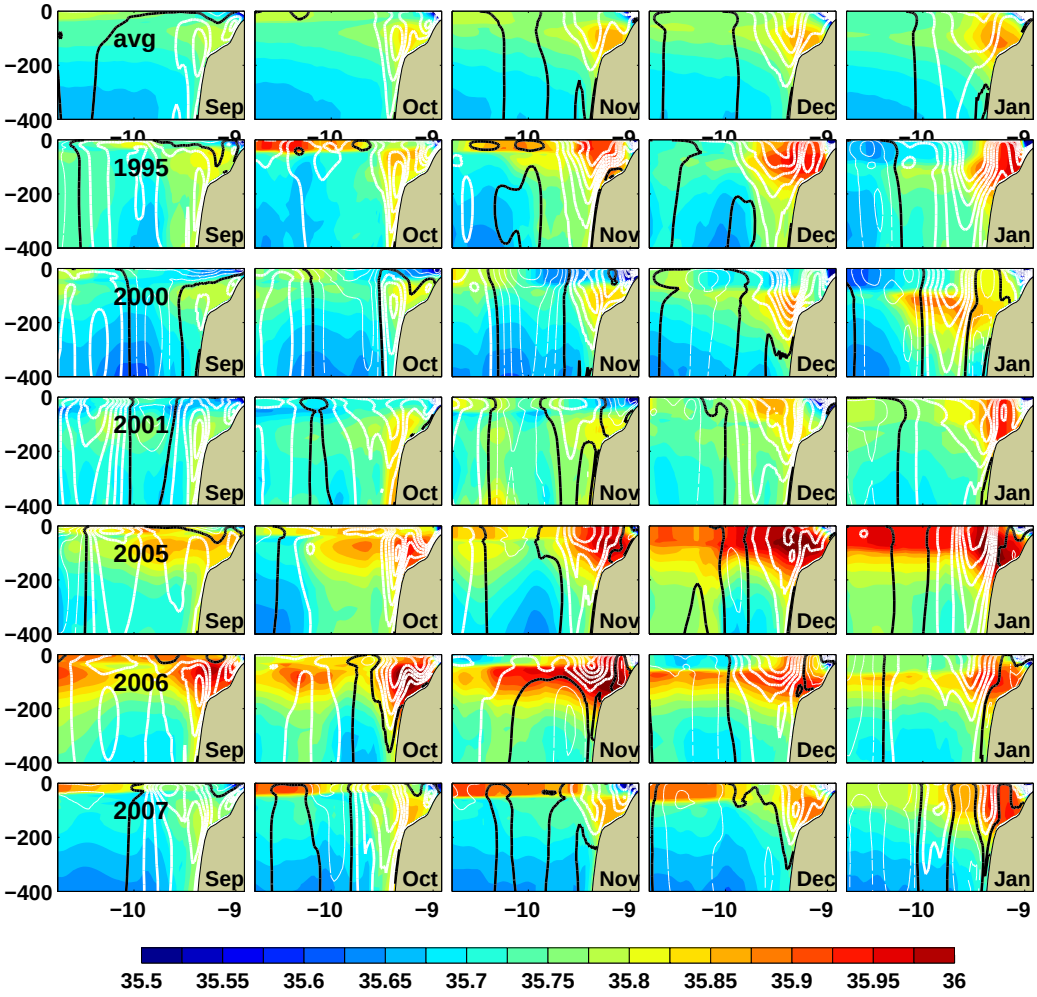

Figure 4.3: *Vertical sections of meridional velocities (m s^{-1}) in contours and salinity (psu) in colors. The various columns correspond to different months. The first row is the average of all the 20 years of simulation, the following rows correspond to anomalous years, indicated in the figure. The velocity contours have an interval of 0.03 m s^{-1}; positive values are displayed on a thick white line, negative on a thin white line, and zero is in black.*

To help explaining the temperature and salinity interannual variability and to split the local from the remotely forced contributions, we computed the time evolution of the anomalies of the terms in the heat and salt budgets equations (equations 2.3 presented in chapter 2), volume averaged in

the top 200 m of domains W and N (Fig. 2.1). The anomalies were obtained by computing the monthly averages and removing the seasonal cycle (represented in Fig. 2.16). To better visualize the importance of each of the terms we plot the cumulative of the anomalies, since the beginning of 1989 till the end of 2008 (Fig. 4.4). The figure shows the cumulative of the heat and salt budgets anomalies, for the domains N and W (Fig. 2.1). The time rate curve for each of the plots in Fig. 4.4 is approximately coincident with the curve representing advection plus the atmospheric forcing, showing that these two terms control the interannual variability. The two curves show a small divergence in the northern coast (Fig. 4.4 b) after 1998, and converge again in the end of 2005, suggesting the mixing terms were important at these moments. The cumulative of the rate of change of heat and salt (blue line in Fig. 4.4) approximately reconstructs the TN200, SN200, TW200 and TN200 evolution, shown in Fig. 4.1. The cumulative of the advection and atmospheric forcing terms give an idea of how the temperature and salinity evolution would be in case there was only the contribution of the advection or of the atmospheric forcing separately. By analyzing their signals we see the separated contribution of each term for the evolution of the volume averaged temperature and salinity in both domains.

4.3.1.1 1995/1996

The winter of 1995/1996 had particularly strong northward transport, much above the average from October to January (see Fig. 4.1 e). There were also strong positive temperature and salinity anomalies on both the western and northern coasts (see Fig. 4.1 a-d). It has been described in literature as a strong IPC winter on both coasts, due to its strong signal in the SST (see SST on Fig. 4.1 a,c).

As it can be seen in the salinity section (Fig. 4.3) in October 1995 the IPC is transporting salinity northwards, since the IPC core and the salinity maximum overlap. IPC is also transporting heat northward (see Fig. 4.2) as can be seen by the downward tilting of the isotherms toward the slope.

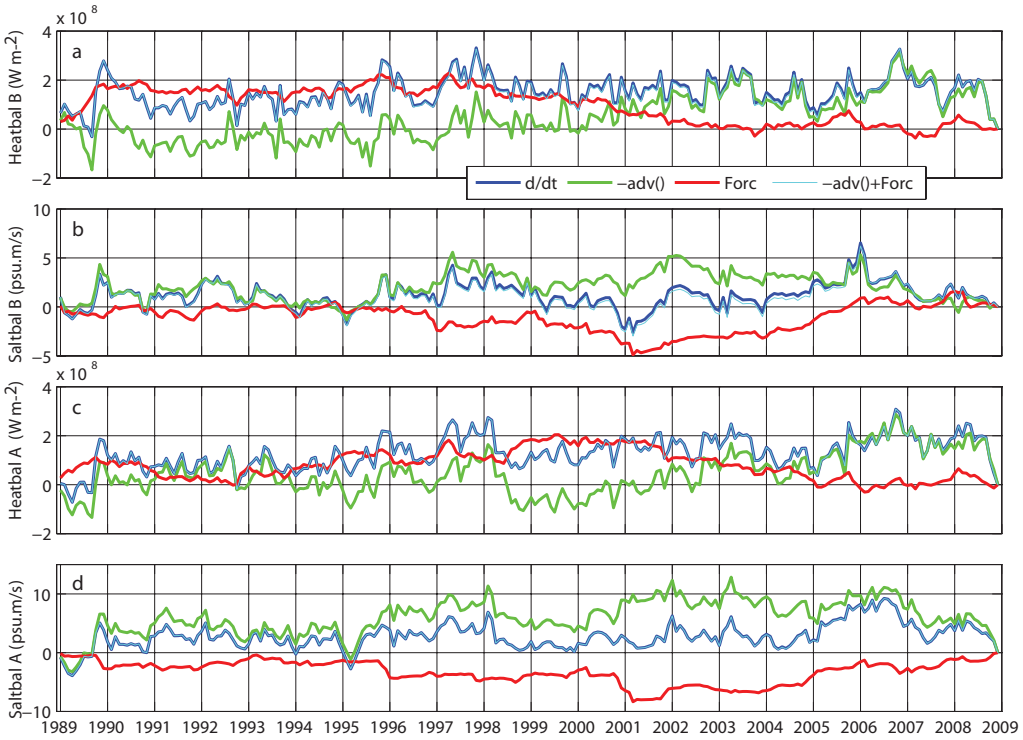

Figure 4.4: *Cumulative time integral of the anomalies of volume averaged (top 200 m) heat and salt budgets for northern and western coast. (a) volume averaged heat equation terms (domain N); (b) volume averaged salt equation terms (domain N); (c) same as a, but for domain W; (d) same as b, but for domain W. In each subplot it is represented the time rate, advection, atmospheric forcing and the sum of advection and atmospheric forcing.*

After October, the IPC core surfaces and continues transporting heat and salt northward along the slope, from more than 200 m depth to the surface. Besides this salinity maximum transported by the IPC it seems that a local surface maximum is developing offshore in October and November, probably forced by local air-sea fluxes.

The temperature and salinity positive anomalies are visible in the cumulative of the rate of change of heat and salt for both domains N and W, in the end of 1995 (Fig. 4.4 a-d). For both domains, it is confirmed that the positive anomalies of temperature and salinity are mainly forced by advection

(blue and green lines on Fig. 4.4 a-d). Regarding the heat budgets, there is also some contribution to the warming from the atmospheric fluxes, stronger in the northern domain (see positive tendency in cumulative forcing in red in Fig. 4.4 a).

4.3.1.2 2000/2001

In 2000/2001, VW200 is below the average in September and October and above the average from November to January (see Fig. 4.1 e). A positive anomaly of TN200 and TW200 also develops in December 2000 and January 2001 (Fig. 4.1 a,c), associated to the positive anomaly in the northern transport. Peliz et al. (2005) and Garcia-Soto (2004) had already identified this winter as having a strong IPC, due to the observed positive anomaly in the SST (Fig. 4.1 a,c). However, there is a negative anomaly in both SN200 and SW200 during all the IPC season (Fig. 4.1 b,d), that was also observed by Llope et al. (2006) in the northern coast.

The vertical sections of alongshore velocity and temperature (Fig. 4.2 2000) suggest that in December and January the IPC is transporting heat northwards, since there is a downward tilting of the isotherms toward the slope coincident with the position of the IPC core. The IPC also seems to be transporting salinity northward, since there is a salinity maximum coincident with the IPC core (Fig. 4.3 2000 - September to January). However, a salinity minimum is developing near the surface through all the IPC season, probably forced by local anomalous air-sea fluxes. This is confirmed by the analysis of the heat and salt budgets time series (Fig. 4.4). The positive anomaly in TN200 and TW200, observed in December and January of this winter, was forced by advection (Fig. 4.4 a,c): in both domains, the heat time rate of change increases in December 2000 (blue line), following an increase in the advection terms (green line), and suggesting the importance of the anomalously strong IPC in advecting heat northwards. Regarding the salinity evolution, advection is also contributing to increase the salinity anomaly in the western coast (Fig. 4.4 d, green line, in the end of 2000). However,

the atmospheric forcing is strongly negative (Fig. 4.4 b,d, red line, in the end of 2000) and is responsible for the negative salinity anomalies obtained in this winter (Fig. 4.4 b,d, blue line, or Fig. 4.1 b,d). The anomalous negative atmospheric forcing on salinity is a result of strong precipitation that occurred in the autumn of 2000 over Europe (Marsh and Dale, 2002).

4.3.1.3 2005/2006

In the winter of 2005/2006, northward transport anomalies oscillate around the average (Fig. 4.1 e). In October, the VW200 anomaly is high; in September and December it is slightly below the average, and in November and January it is slightly above the average. Temperature is above the average till December and below the average after January (especially the SST and TN200 - Fig. 4.1 a,c). This winter is peculiar because of the outstanding positive salinity anomalies (SN200 and SW200), which stand out as the higher values of the study period. They exceed 0.1 above the average in December and January, on both the northern and western coasts (Fig. 4.1 b,d). These intense salinity anomalies were already reported in Somavilla et al. (2009) for the northern coast. These authors argue that the high salinity anomalies resulted from a precipitation deficit in the winter of 2005.

In our simulations, the salinity anomaly is clear in the vertical sections of Fig. 4.3 2005. Although there is a maximum associated to the IPC core from October to January, the anomaly spans throughout the whole section and is stronger near the surface, suggesting that part of it is forced locally. This is confirmed by the salt budgets analysis, shown on Fig. 4.4 b,d. Although advection is important to the local increase of salinity in the end of 2005 (especially in the northern coast (domain N) - Fig. 4.4 b), there is also a strong contribution from the local atmospheric forcing that is very intense (positive) during the whole year of 2005 and even more intense at the end of the year (see the positive slope of the atmospheric forcing curve in 2005 Fig. 4.4 b,d in red). In fact, the winter of 2005-2006 marks the end of a period of approximately 5 years of intense atmospheric forcing in the salt budgets

(strong evaporation and/or weak precipitation), increasing the salinity to unprecedented values in the 20 years covered by this study (Fig. 4.1 b,d - end of 2005).

4.3.1.4 2006/2007

In the winter of 2006/2007, VW200 is also around the average. The time series of transport anomalies show values slightly above the average in October and November and very close to the average on the other months (Fig. 4.1 e). However, there are strong positive anomalies in temperature and salinity (Fig. 4.1 a-d), already reported in Le Cann and Serpette (2009).

On the northern coast, TN200 was atypically low in the beginning of 2006 (Fig. 4.1 a). A strong positive anomaly develops from September 2006 to January 2007, forced by advection (Fig. 4.4 a). The anomalies in the intensity of the IPC in September and October were not high enough to explain the strong anomalies in temperature; what explains the reached temperature values was the anomalously intense advection during the whole year of 2006 (see positive slope in Fig. 4.4 a,c) that is related to anomalously intense northward flow (Fig. 4.1 e). SN200 was high in the beginning of 2006. The anomaly decreases in March/April, and then decreases again in December. The strong decrease of the anomaly in March/April is mostly forced by advection (Fig. 4.4 b), although there is also a contribution from the atmospheric forcing and from the vertical mixing (the vertical mixing term is not shown but this is one of the few months when vertical mixing is of the same order of magnitude as the atmospheric forcing). An anomalous event of mixed layer deepening in this winter was already described by Somavilla et al. (2009) and Cabrillo et al. (2011). As our model vertical mixing term is important in March/April 2006, it means that the model mixed layer reached deeper than 200 m. This event of anomalous mixed layer deepening in the northern coast is discussed below.

On the western coast, the TW200 anomaly was high after April 2006 (Fig. 4.1 c). The anomaly decreases in August 2006, and increases again after

September, reaching its maximum value in November, but remaining positive throughout the season. This variability was mainly forced by advection (Fig. 4.4 c), resulting from the intense poleward flow during the whole year of 2006 (Fig. 4.1 e). There was also a small contribution from atmospheric forcing in October/November. SW200 presents a strong anomaly that is still reminiscent of the previous winter (Fig. 4.1 d). The salinity anomaly reaches maximum intensity in August/September 2006. After September it starts decreasing, and in December/January it is still positive, but only about a third of the September value. In the northern coast, as described in the previous paragraph, the salinity anomaly decreased, forced by advection in March/April (was advected away of domain N). In the western coast there was no significant decrease of the salinity anomaly, because the anomaly was not advected away. Figure 4.4 d confirms that advection and atmospheric forcing gave a small contribution to the August/September salinity anomaly maximum, but mostly the anomaly is still there from the previous year.

The salinity sections presented in Fig. 4.3 2006 illustrate these processes. The salinity maximum extends offshore till the offshore limit of the section as early as in September. In September, when SW200 reaches a maximum one can observe several patterns: an area of high salinities near the surface forced locally by air-sea fluxes; a maximum coincident with the IPC core related to IPC advection; and a maximum offshore that is still reminiscent of the strong 2005 convection event.

4.3.2 Variability of the Forcing of the IPC

In the previous subsection we showed that the interannual variability of temperature and salinity depend on the intensity of the IPC, and on the local air-sea heat and salt fluxes that become important especially during anomalous years. In this section, we analyze the interannual variability of the northward transport (or of the intensity of the IPC) and investigate what drives its year-to-year variability from September to January (the months of intense IPC). Monthly averages of northward transport (VW200) are com-

pared with: monthly averages of the meridional (N-S) component of the wind horizontally averaged in the domain W (Fig. 2.1); monthly averages of large scale wind stress curl, averaged in the blue area represented over the wind and wind stress curl fields on Fig. 4.6 (top row); and finally with JEBAR, averaged between the latitudes of domain W and between the isobaths of 200 and 1200 m depth (as in chapter 3, Fig. 3.1 (cyan line)). The comparisons are displayed in Fig. 4.5.

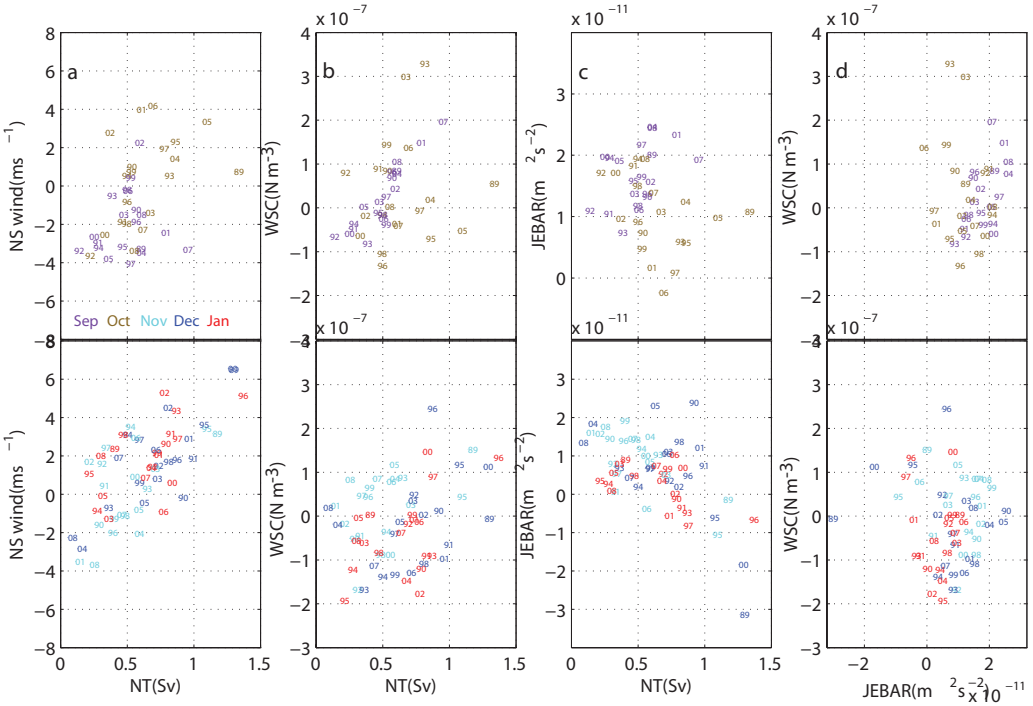

Figure 4.5: *Diagrams of monthly averages of various quantities. On the top, September and October. On the bottom, November, December and January. (a) VW200 (northward transport) versus meridional wind (averaged in domain W - Fig. 2.1); (b) VW200 versus wind stress curl (averaged in blue domain - Fig. 4.6 a-c); (c) VW200 versus JEBAR (averaged between the latitudes of domain W and between the isobaths of 200 and 1200); (d) JEBAR (same as in c) versus wind stress curl (same as in b).*

Figure 4.5 (a) compares the monthly averages of VW200 with the meridional wind. From November to January there is a clear relation between VW200 and north-south winds. On these months, the stronger the southerly winds, the stronger the northward transport of the IPC. These results reinforce the idea presented in chapter 3 that wind forces the northward flow on these months. The correlation coefficients between meridional wind and VW200 are statistically significant at 5% level in November, December and January, with values of 0.54, 0.80 and 0.59, respectively. In October, there is no significant correlation between the intensity of southerly winds and VW200. However, there seems to be some relation between both (Fig. 4.5 a), if the years of 2001, 2002 and 2006 are excluded.

For the months of November to January (Fig. 4.5 c) there is an inverse relationship between VW200 and JEBAR, and stronger transport values correspond to small values of JEBAR. This is in agreement with our results from chapter 3. It is shown that during these months, the wind is the main forcing of poleward flow, and that the northward density advection reduces the meridional density gradient decreasing the JEBAR.

4.3.2.1 September

In September, the variability of VW200 is not correlated with the variability of meridional component of the wind. Instead, there is a correlation of 0.89 (statistically significant at 5% level) between VW200 and the wind stress curl averaged on a larger domain (blue box on Fig. 4.6 a). Fig. 4.5 (b) compares the monthly averages of VW200 with the wind stress curl. By analyzing wind stress fields, we verified that the stronger events of northward flow in September were associated with strong winds and strong wind-curl in the northern part of the western Iberian coast. The average September wind and wind stress curl fields are plotted together with the Septembers of 2001 and 2007 in Fig. 4.6 (top). The years of 2001 and 2007 are the ones with stronger VW200 in September.

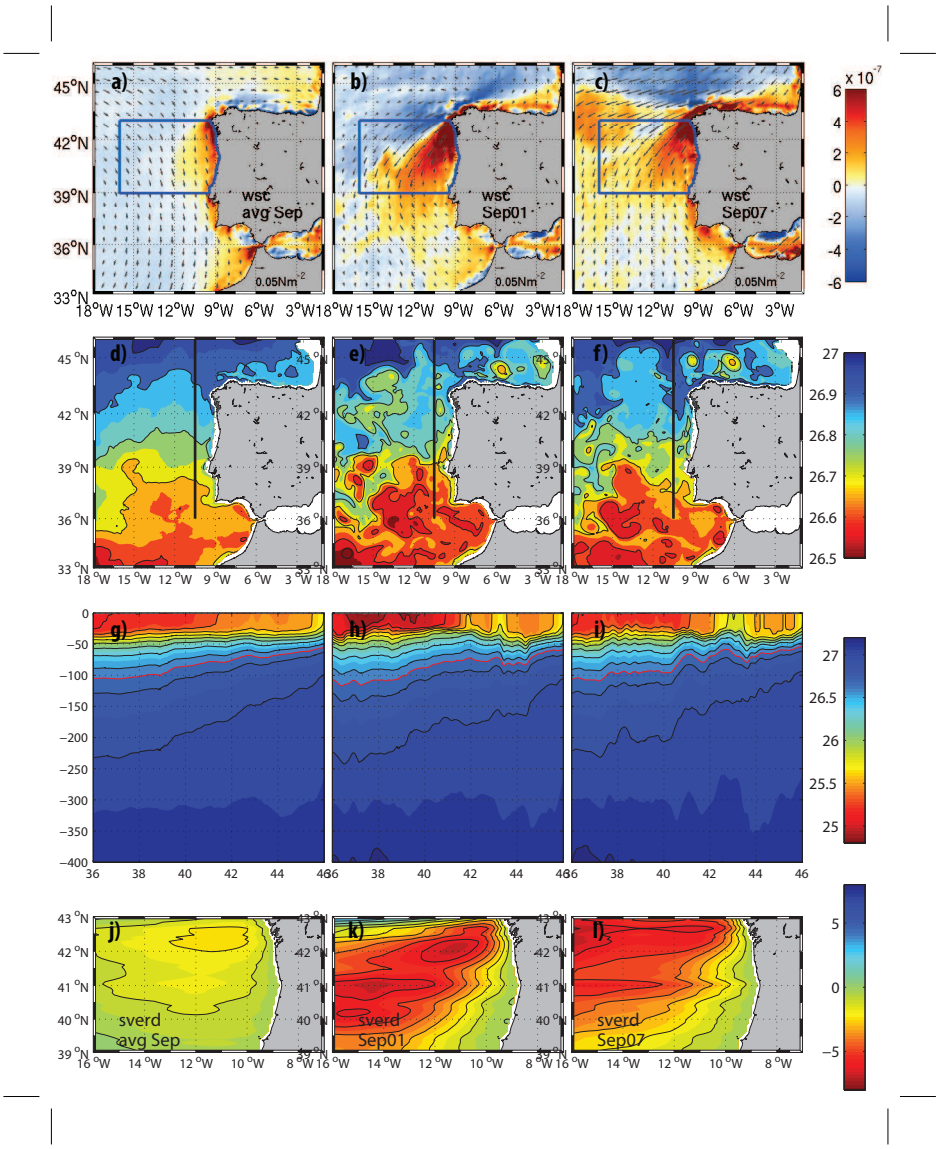

Figure 4.6: *September mean fields. Left: global average of all Septembers (1989 to 2008). Middle column: average September 2001. Right: average September 2007. (a-c): wind stress field (N m^{-2}) and wind stress curl (WSC) (N m^{-3}), the domain in blue is used to average the WSC. (d-f): potential density at 100 m depth (kg m^{-3}). (g-i): potential density section (in black in the second row), with the isopycnal 26.7 in red. (j-l): Sverdrup Stream function (Sv), the transport between contours is 0.5 Sv.*

The average wind field in September is dominated by northerlies (upwelling favorable), with a positive wind stress curl extending offshore till around 12°W (Fig. 4.6 a). The positive wind stress curl forces a divergence at the surface that induces a shallowing of the isopycnals by Ekman pumping. Figure 4.6 (g) shows a vertical meridional section of potential density (see location of the section as a black line in Fig. 4.6 d-f). It is observed an uplift of the isopycnals from 39 to 43°N, associated to the local positive wind stress curl (easy to see in the reference isopycnal 26.7 in red). The uplift of the isopycnals increases the meridional density gradient ($\mathrm{d}\rho/\mathrm{dy}$) on the upper thermocline near 39°N, increasing the local JEBAR where the thermocline intercepts the topography.

Away from the slope, the Sverdrup dynamics become relevant. We computed the average September Sverdrup stream function using the Sverdrup relation:

$$\beta \frac{\partial \psi}{\partial x} = \hat{k} \cdot \nabla \times \frac{\vec{\tau}}{\rho_0} \tag{4.1}$$

and integrated westward, considering a kinematic boundary condition at the coast. The average stream function is represented in Fig. 4.6 (j): this wind stress curl spatial structure forces an extra-coastal cyclonic circulation, transporting waters northward on the eastern part. Since waters in the south are less dense than in the north at the same depths, the Sverdrup circulation enhances the meridional density gradients along Iberian west coast, by bringing subtropical waters northwards. Fig. 4.6 (d) shows September average density field at 100 m depth, and it is visible that from around 10°W to 15°W there is a northward displacement of the isopycnals, probably associated with this offshore cyclonic circulation (although the spatial structure is not exactly the same of the stream function).

By inducing strong meridional density gradients, the events of strong wind stress curl magnify JEBAR, which is the main forcing of the IPC in September (chapter 3). Fig. 4.5 (d) show the existence of a correlation between wind stress curl and JEBAR in September, the correlation coefficient is 0.58 (statistically significant at 5% level).

On Fig. 4.6, we also plot the same fields for the two years of strongest northward transport in September (2001 and 2007), that also correspond to periods of high average wind stress curl (Fig. 4.5 b). In the case of 2001, the strong wind stress curl area extends further to the south than that in 2007 (Fig. 4.6 b,c). The effects of this difference are seen in the other fields. Comparing the Sverdrup stream functions of both years (Fig. 4.6 k,l) it is clear that both have stronger northward transport than average, and it extends further south in 2001. The effect of the offshore circulation is visible on the density fields at 100 m depth (Fig. 4.6 e,f). In 2001, the northward advection starts from further south, resulting in a strong density front at around 39°N (Fig. 4.6 e). In 2007 the same situation is verified though in a smaller area. In this case, the effect did not extend so far to the south and the stronger density front is centered at about 41°N. This is also visible in the vertical sections of Fig. 4.6 (h,i), by the local uplifting of the isopycnals, coincident with the areas of strong wind stress curl. In 2001, this process happens approximately from 39 to 43°N whereas in 2007 it happens from 40 to 44°N.

These results suggest that, at least in September, JEBAR changes can be localized and forced by local wind forcing. It seems that wind stress curl influences JEBAR both by locally uplifting the isopycnals (Ekman pumping) and by meridionally displacing the zonal density fronts (extra-coastal Sverdrup dynamics). On Fig. 4.5 c) we plotted JEBAR against transport (VW200). There is no significant correlation between both, although, excluding 1994, 2000, 2005 and 2007, it seems that higher VW200 values are associated to stronger JEBAR in September. The weak correlation might be because in some years there are other factors involved. VW200 is the average northward transport in the domain W (Fig. 2.1) that extends offshore till 10°W, further than the slope limit. It is possible that the local effect of wind stress curl, which is negligible over the slope (as shown in chapter 3), becomes important offshore and directly contributes to the increase in transport, by Sverdrup dynamics, as represented in Fig. 4.6 (j-l). On Fig. 4.3 we added

the meridional velocity sections of 2001 and 2007. It is visible that there are strong northward velocities, in September, on both years, but the structure is quite different. In September 2001 the IPC core structure is similar to the Septembers average (top Fig. 4.3), but much more intense. In September 2007 there is a second northward velocity structure, located offshore, that is also contributing to the northward transport and that might be associated to the Sverdrup transport.

This analysis shows that on average the intensity of the IPC, from November to January, is dependent on the intensity of the southerly winds. In September, on the other hand, it is the extra-coastal wind stress curl that matters. Amongst other effects, this larger scale wind stress curl bears an indirect effect on JEBAR, and its intensity will influence the magnitude of the northward transport. In October, VW200 is mainly controlled by the intensity of southerly winds, although this is not true for all years, indicating that October may be a transition month.

4.4 Discussion and Conclusions

Our results confirmed that the IPC undergoes a strong interannual variability. Most of the studies referred so far could not explain the observed variability because of spatial and temporal sampling limitations and our model simulation helped in understanding some of the questions that remained. Most of the previous studies inferred the intensity of the IPC by the intensity of the SST anomalies, which is not always correct since the IPC can be intensified below the surface and the local air-sea fluxes also affect the SST. Our model reproduces the events of strong SST anomalies described in the literature for the northern coast: 1989/1990, 1995/1996, 1997/1998, 2000/2001, 2002/2003 and 2006/2007 (Garcia-Soto et al., 2002; Garcia-Soto, 2004; Le Cann and Serpette, 2009; Le Hénaff et al., 2011; Garcia-Soto and Pingree, 2011); and for the western coast: 1989/1990, 1995/1996, 1996/1997, 1997/1998 and 2000/2001 (Peliz et al., 2005).

From November to January, the IPC magnitude depends mostly on the intensity of the southerly winds (meaning that the current is locally forced on the west coast and the flow latter turns to the north coast). This supports the argument of Garcia-Soto and Pingree (2011), that the strongest IPC events (based of SST satellite signal) happen under the presence of strong atmospheric cyclones. We also verified that this is not true in September when the intensity of the northward transport is related to larger scale wind stress curl. The latter affects the meridional density gradients in the west coast, changing JEBAR, which is the main forcing of poleward flow over the slope (see chapter 3).

In years of stronger IPC there is a higher transport of heat and salt that forces positive anomalies of temperature and salinity. However, the temperature and salinity anomalies may also be in anti-phase or uncorrelated with the IPC magnitude. This behavior is associated with the interannual variability of the local air-sea fluxes.

We explained the IPC, salinity and temperature anomalies in four different winters that were already described in the previous studies as anomalous:

- The winter of 1995/1996 was identified as a having a strong IPC event because of its warm SST signal in both western and northern coasts (Garcia-Soto, 2004; Peliz et al., 2005; Le Cann and Serpette, 2009). Llope et al. (2006) also reported salinities over the average in this winter. Our model reproduces these intense anomalies in temperature and salinity and show that they were forced by a strong IPC, with values only comparable to the ones of the winter of 1989/1990.

- The winter of 2000/2001 was identified as a strong IPC event because of its warm SST signal in both western and northern coasts (Garcia-Soto, 2004; Peliz et al., 2005; Le Cann and Serpette, 2009). However, Llope et al. (2006) observed a low salinity anomaly in this winter. We show that this year had a strong IPC that transported heat and salt northward, but due to strong precipitation, the salinity (E-P) fluxes were negative, inducing negative salinity anomalies.

- The winter of 2005/2006 was also atypical. Somavilla et al. (2009) described an event of saltier ENACW in the northern coast following a winter of cold and dry atmosphere. Our model also simulates the high salinities in this winter, in both western and northern coasts, although the intensity of the IPC is around the average. Somavilla et al. (2009) concluded that strong air-sea temperature differences resulted in strong loss of heat from the ocean to the atmosphere that induced a strong density increase near the surface. This resulted in a deeper than usual mixed layer and a vertical salt flux from the upper layer into the ENACW levels. We plot the evolution of the salinity vertical structure in Fig. 4.7 a-b (the vertical profiles correspond to horizontal averages within domains N and W; see Fig. 2.1). In the same figure, we overlay the mixed layer depth and the 27.1 isopycnal surface, as an indicator of the ENACW. The anomalous salinity event, on the years of 2005 and 2006, is visible in both northern (Fig. 4.7 a) and western (Fig. 4.7 b) coasts. In the northern coast, the model reproduces the mixed layer deepening and it reaches as deep as the 27.1 isopycnal, showing that our model reproduces the event of strong vertical salt flux observed in that year by Somavilla et al. (2009). This happened a single time in the whole 20-year time series. The salinity was also high in the western coast (Fig. 4.7 b), but the mixed layer was not particularly deep. The second largest deepening of the mixed layer in the northern coast was in the end of 1990, but it did not reach ENACW levels.

- The winter of 2006/2007 was described in Le Cann and Serpette (2009). The authors observed strong salinities in the northern coast, prior to the development of the surface intensified IPC with a surface thermal expression. Our model reproduces the anomalously high salinities and we verify that they are remnant from the strong salinity anomaly developed in the previous winter of 2005-2006.

Most of the previous studies about the IPC variability focused on one or two specific months in each winter. We observed that the sub-seasonal (month-to-month) variability can be large, and the analysis based on only one

or two months may not be representative of the northward transport of heat and salt in that winter. Also, in September and October, the IPC is usually not intensified at the surface, which means that its role in transporting heat and salt northward is not detectable in the SST satellite images. Our simulation helped in understanding the interannual variability of the IPC from 1989 to 2008. Since the boundaries of our simulation are climatological, we do not represent any effect of the large scale variability on the northwestern Iberian shelf/slope. However, we showed that our simulation is reproducing most of the observed variability, which suggests that the forcing is essentially local.

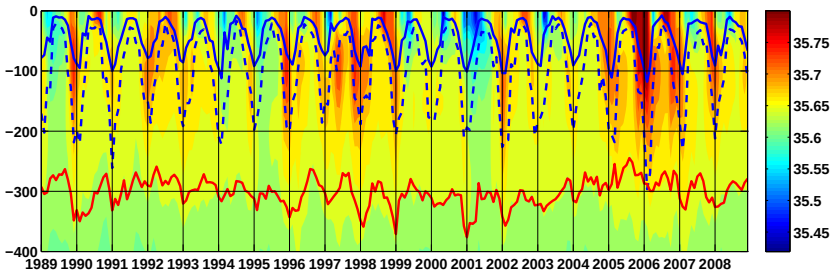

(a)

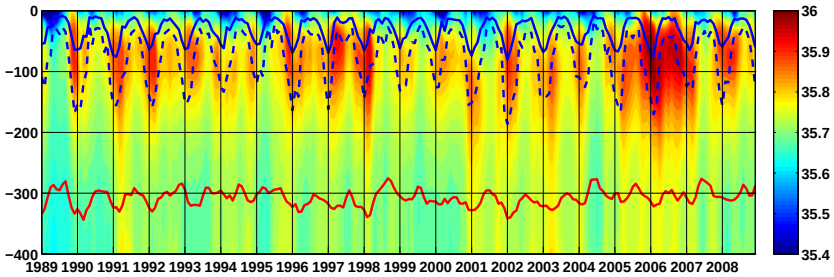

(b)

Figure 4.7: *Area averaged salinity (psu) represented in function of depth and time for the northern (domain N - Fig. 2.1) and western (domain W) coasts. Continuous blue line represents the average monthly mixed layer depth horizontally averaged in the same domain. The dashed blue line represents the absolute maximum of the mixed layer that occurred at any point of the domain and in the respective month. Red line is the depth of isopycnal 27.1, characteristic of ENACW.*

Chapter 5

Swoddies

5.1 Introduction

Eddies associated with IPC were first described in Pingree and Le Cann (1992b). The authors identified 3 anticyclonic eddies in satellite SST images, persistent and remarkably warmer offshore, that the authors named "Slope Water Oceanic eDDIES" (Swoddies). All of these 3 cases were observed in the Bay of Biscay in the winter of 1989/1990, which was characterized by a strong IPC (see chapter 4): one eddy formed to the east of Cape Ortegal (O90), and the other two near Cape Ferret (F90a,F90b). F90a was observed in-situ on the next summer and it showed an homogeneous core of water in the eddy center, a radius of approximately 40 km, and maximum velocity at 100 m depth; its presence was felt as deep as 1800 m depth. Later, other eddies were observed in the Bay of Biscay. Pingree and Le Cann (1992a) identified one in May of 1996 with unknown place of formation, although the fact that its core was colder than F90 suggests that it could have formed further north. Garcia-Soto et al. (2002), using cloud-free satellite SST images, detected various Swoddies on the southeast corner of the Bay of Biscay, in January 1990 and January 1996. Both years also correspond to periods of strong IPC.

Swoddies also form and detach from the slope on the west coast. One was observed in-situ at 41-42°N, in May of 1993, by Fiúza et al. (1998); another

was observed at 40.5-40.9°N, in February 2000, by Oliveira et al. (2004). Peliz et al. (2003b, 2005) also detected Swoddies forming on the west coast, in cloud-free satellite SST images, in January and February of 1997, February of 1998, and January of 2002.

In order to understand the mechanisms of Swoddies formation, Dubert (1998) developed an idealized model configuration of the IPC by introducing a meridional density gradient interacting with the slope. He analyzed the interaction of the current on the northern Iberian coast, past a cape similar to Cape Ortegal. The results showed that eddies detach upstream of the cape, as a dipolar structure where Swoddies have a companion cyclone. It was also verified that bottom stress is important for the anticyclone formation, as it allows anticyclonic vorticity on the inshore side of the jet. Peliz et al. (2003b) also used an idealized model configuration, forced by meridional density gradients, but for the west coast. They verified that anticyclones form in the lee of the main topographic features; the anticyclones remain trapped for periods of 2/3 months while several cyclones develop around them, by a deep cyclogenesis process. These deep cyclones were shown to be important for the process of detachment of the Swoddies from the slope; when cyclones get strong enough, their circulation intensifies, pushing the anticyclones away from the slope.

Despite the existence of various studies about these anticyclonic eddies, few of them were observed. The studies describe observations of sporadic eddies at specific instants in time, and not much is known about their statistics, places of formation, life-time, decay and separation processes, and behavior away from the slope. In this study, these problems are addressed by studying the population of eddies in our 20 year model simulation, identified using an automatic eddy detection algorithm. The next section presents the methods used for the detection of eddies. Section 3 describes general characteristics of their population. Section 4 presents the results about the Swoddies: it starts with a comparison with observations, followed by an analysis, at the synoptic scales, of the Swoddies formation in the winter of 1989/1990, and finishes

with a general analysis of the Swoddies population. Finally, in section 5, the results are discussed.

5.2 Methods

5.2.1 Eddy Tracking Algorithm

It was used one automatic algorithm for eddy detection and tracking, developed by Nencioli et al. (2010). The algorithm detects eddies by analyzing the geometry of a 2D velocity vector field at a given depth level. It uses a series of constrains that detect the presence of the eddy by searching for its effect on the distortion of the velocity field. The method was developed to analyze eddy activity from high resolution model simulations and was used in previous studies (Dong et al., 2012; Aguiar et al., 2013; Peliz et al., 2012).

5.2.2 Eddy tracking at 100 and 250 m depths

Given the fact that previous studies indicate that Swoddies have maximum velocity signatures at 100 m depth we conducted a first eddy tracking exercise at this depth. Conversely, to capture the cyclones formed by the squeezing of the deeper layers, another tracking was done at 250 m depth. From all of the detected eddies, we selected the ones that were tracked for a minimum of 2 consecutive time steps (of the model output), and that were first detected near the slope, north of 40°N (region represented in Fig. 5.4), within the period from October to March. This period was chosen in order to cover the months when the IPC is strongest and surface intensified (October to January), and also the months when it weakens and when the anomalies propagate offshore (January to March).

The detected eddies are not necessarily intensified at the detection depth. For example Meddies, which are intensified at deeper levels, can have a dynamical signature near the surface (Serra et al., 2010; Aguiar et al., 2013). To identify the level at which each eddy (from the detected population) is

intensified we computed profiles of relative vorticity at each eddy's center and searched for its maximum in depth. Figure 5.1 (bottom) shows how many cyclones and anticyclones have the maximum at each depth, for the detections made at 100 and 250 m (left and right columns, respectively). In Fig. 5.1 (top), each eddy is represented as a function of the depth of maximum relative vorticity and its intensity. For detections made at both levels, eddies are intensified at a wide range of depths, from the surface till deeper than 1200 m. Different layers are distinguished, presenting eddy populations with different characteristics. These differences are analyzed in the next section.

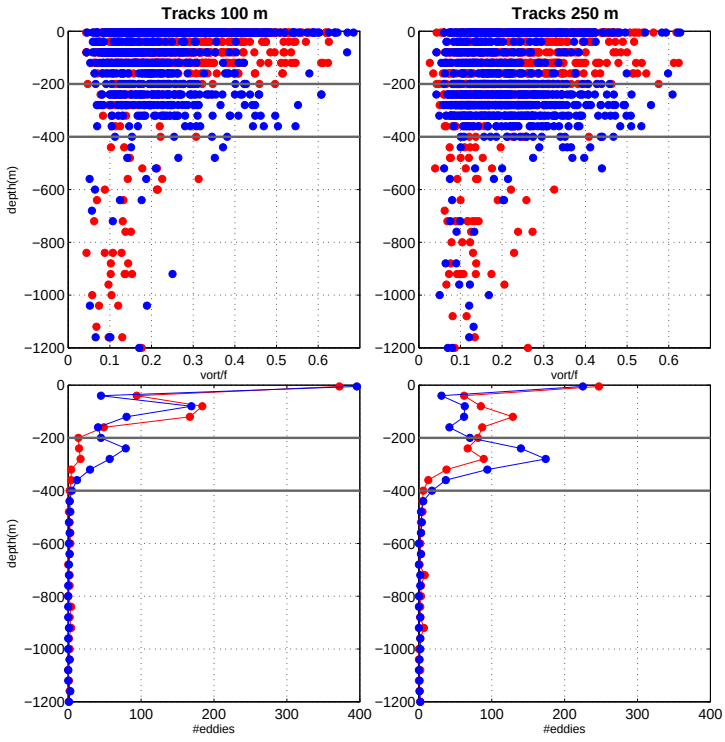

Figure 5.1: *Distribution of eddies formed at the slope area (Fig. 5.4), from October to March. Top: diagram with all the detected eddies, in function of their relative vorticity maximum and its depth. Bottom: number of eddies with maximum relative vorticity at each depth. On the left column, eddies detected at 100 m depth; on the right column, eddies detected at 250 m depth. Anticyclones are represented in red and cyclones in blue.*

5.3 Statistics of detected eddies

5.3.1 Different Eddies in Depth and the Statistics of Vorticity

As referred in the end of the last section, there are distinct layers in the vertical, with different characteristics in terms of distribution of cyclones and anticyclones. For the eddy tracking done at 100 m depth (Fig. 5.1 - left) two main layers are distinguishable: a surface layer, from the surface till around 200 m depth, which has stronger anticyclones (see the higher values of vorticity for anticyclones in this layer on Fig. 5.1 (top left)); and another layer, between 200 and 400 m depth, with more and stronger cyclones. Below 400 m depth, the number of detected eddies decreases. Even though, the cyclonic dominance seems to extend to around 600 m depth, and from 600 to 1000 m an anticyclonic dominance is observed, with more and stronger anticyclones than cyclones (this is more clear from 750 to 1000 m depth). For the tracking done at 250 m (Fig. 5.1 - right) the results are similar. The main differences are: the detection of more cyclones in the second layer; and the increase in the ratio between the number of anticyclones and cyclones, also in the second layer (the absolute number of both eddies decreases). This difference in the polarity is because in the upper layer anticyclones are stronger than cyclones, and so their signal extends to deeper levels.

We compared these results with the statistics of the relative vorticity. To get the vorticity distribution in the slope, we computed the probability density function (PDF) of the relative vorticity for all instants, all model grid points contained in the slope area (red line in Fig. 5.4), and at various levels in depth. We represent the PDFs for 120 and 280 m depth (Fig. 5.2-left). The tails of the PDF correspond to the stronger negative and positive values of vorticity, usually located at the centre of the eddies. The PDF tail for 120 m depth (blue line) shows a clear tendency for negative vorticity values, for values greater than around 0.2, although the strongest values are cyclonic. At 280 m depth there is a clear tendency for positive

vorticities. In order to get a picture of the variation of the asymmetries in the water column, we computed the vorticity skewness at various depths, and represent the vertical profile on Fig. 5.2-right. The skewness measures the asymmetry of the probability distribution. It seems there is a cyclonic dominance close to the surface, and in the top 200 m depth the dominance is anticyclonic (negative skewness). From 200 to 600 m depth it becomes cyclonic (positive skewness). Below this depth, from 600 till around 1100 m, it is again anticyclonic (negative skewness). This is in agreement with the distribution of eddies per layers described in the previous paragraph.

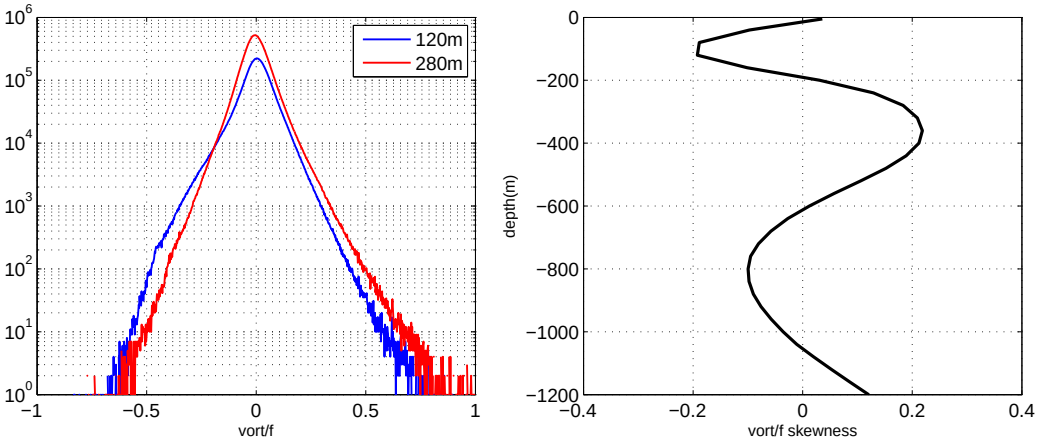

Figure 5.2: *left: Probability density function (PDF) of vorticity fields in the slope area (Fig. 5.4 in red) for 120 and 280 m depth. right: Skewness computed in the same domain, for various depths.*

The eddies detected were divided in 4 different groups: cyclones and anticyclones identified at 100 m depth, which have their relative vorticity maximum between the surface and 200 m depth; and cyclones and anticyclones identified at 250 m depth, that have their relative vorticity maximum between 200 and 400 m depth. In the next section, we describe the characteristics of these different types of eddies.

5.3.2 Characteristics of the Surface and Mid-Water Eddies

Figure 5.3 shows the seasonal cycle of the number of eddies formed on the slope separated by polarity, and layer of maximum intensity. The results show that eddies form every month. The seasonality is larger at the surface layer, with larger number of anticyclones forming in November and from January to April, and of cyclones formation from January to June and in August. The larger number of cyclones obtained in August is probably related to coastal upwelling. On the deeper layer, the amplitude of the seasonal cycle is smaller, but there seems to be more cyclones formed in July and November. In the rest of the analysis, we will only consider the eddies formed from October to March.

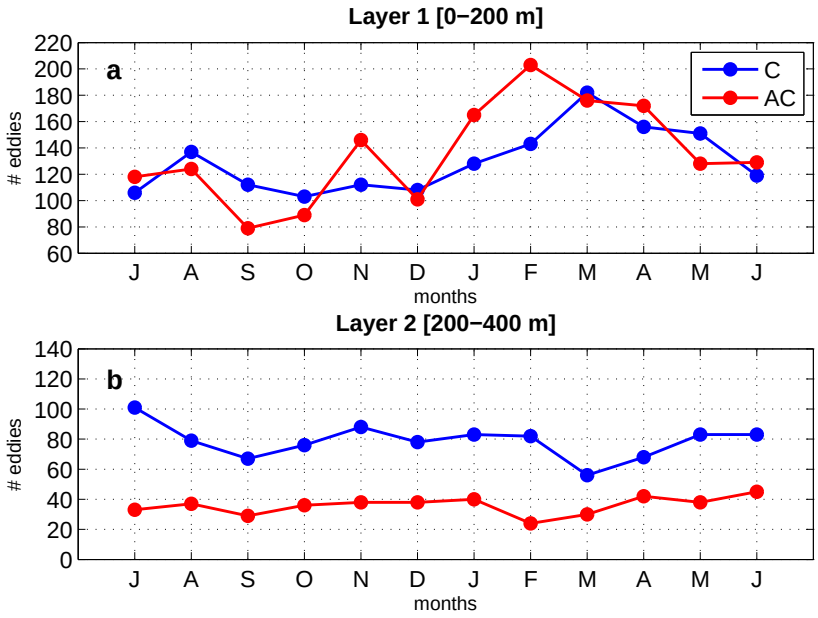

Figure 5.3: *Total number of eddies formed on the slope area, in each month (on the 20 years simulation). Top: cyclones (blue) and anticyclones (red) intensified on the surface layer (0-200 m depth). Bottom: cyclones and anticyclones intensified on the sub-surface layer (200-400 m depth).*

Figure 5.4 shows the preferential places of formation for each type of eddies. The slope is a favorite location for the formation of eddies (see higher density values over the slope in the 4 maps). Cyclones and anticyclones seem to form at distinct places, the places with higher rate of cyclones formation coincide with topographic contours veering offshore in the poleward direction, while anticyclones tend to form in places where topographic contours veer inshore. This dependence on the topographic contours suggests that topography is important in the mechanisms of eddy formation. On the surface layer, there is no clear difference on the quantity of cyclones and anticyclones formed, while on the deeper layer there are much less anticyclones. In the rest of the analysis we will only consider the eddies formed on the slope area (red line in Fig. 5.4).

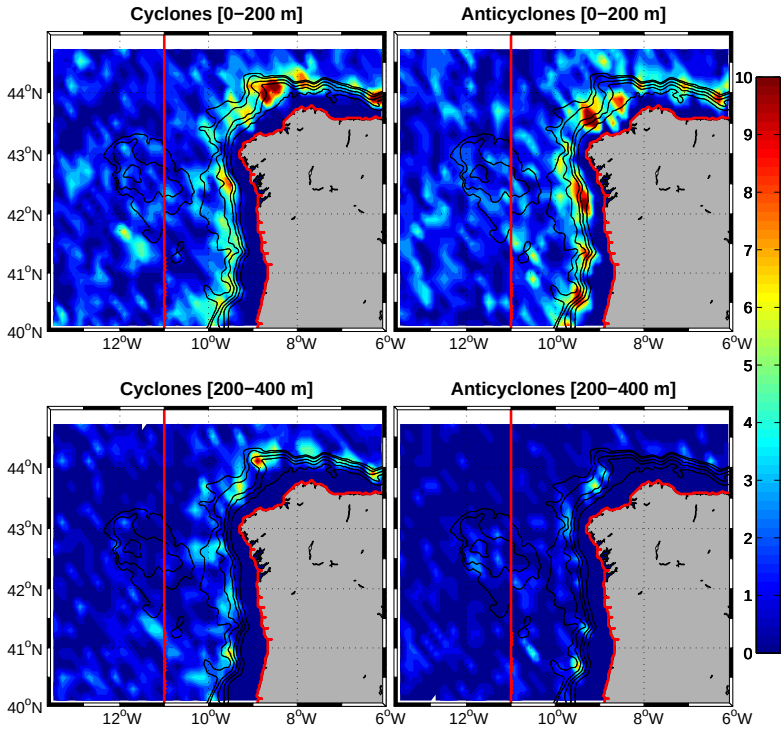

Figure 5.4: *Maps with density of eddies formation. Top: cyclones and anticyclones intensified on the surface layer (0-200 m depth). Bottom: cyclones and anticyclones intensified on the sub-surface layer (200-400 m depth).*

Keeping only the eddies that formed on the slope and from October to March, the number of identified eddies for the entire model simulation is: 880 anticyclones and 776 cyclones intensified at the top 200 m, and 206 anticyclones and 463 cyclones intensified between 200 and 400 m depth.

To analyze the average vertical structure of each type of eddies, we subdivided the eddies in the ones formed north and south of 43°N, because their characteristics are expected to be different. We obtained the central profile of salinity, temperature, and relative vorticity for each eddy, and averaged over the entire population in consideration. The results are displayed in Fig. 5.5. The number of anticyclones intensified at the surface was 396 to the south of 43°N and 484 to the north. The number of cyclones intensified at the surface was 311 to the south of 43°N and 465 to the north. There are more anticyclones intensified at the surface and they have on average higher values of relative vorticity (see Fig. 5.5 top-right). Anticyclones average maximum relative vorticity is approximately -0.2ξ/f (-0.27ξ/f) for eddies formed to the south (north) of 43°N. Cyclones average maximum relative vorticity is approximately 0.15ξ/f (0.225ξ/f) for eddies formed to the south (north) of 43°N. Regarding the eddies intensified between 200 and 400 m depth the situation is the opposite. There are more cyclones than anticyclones: the number of anticyclones was 107 to the south of 43°N and 99 to the north. Conversely, the number of cyclones was 184 to the south of 43°N and 279 to the north. The cyclones intensified at these depths are stronger than anticyclones; their average maximum relative vorticity is approximately 0.2ξ/f (0.24ξ/f) for eddies formed to the south (north) of 43°N, and the maximum is located at an average depth of 250-300 m (Fig. 5.5 bottom-right). Anticyclones average maximum relative vorticity is approximately -0.15ξ/f (-0.16ξ/f) for eddies formed to the south (north) of 43°N.

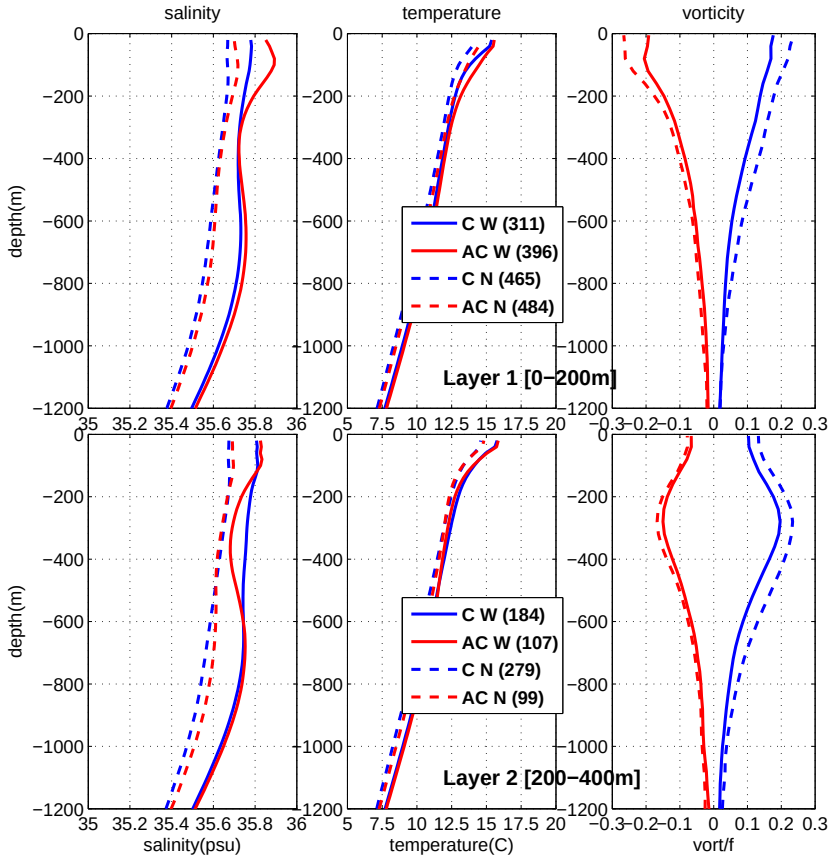

Figure 5.5: *Average vertical profiles of salinity (left column), temperature (middle column) and vorticity (right column), of different eddies populations. On the top, eddies intensified on the upper layer (0-200 m depth). On the bottom, eddies intensified on the sub-surface layer (200-400 m depth). The profiles in a continuous line represent another subdivision, of the eddies that formed on the slope area, but south of 43° N, and the dashed-line eddies that formed on the slope area, but north of 43° N.*

The surface intensified anticyclones have stronger anomalies of temperature and salinity near the surface, suggesting that they are formed by the destabilization of the IPC (the reason why they were named Swoddies). They have higher salinity values on the top 100 m of the water column, both north and south of 43°N (Fig. 5.5 (top)). Temperature increases towards the surface. Salinity and temperature values at the surface are higher on the western

coast (35.85 psu and 16°C) than on the northern coast (35.7 psu and 14°C). Nevertheless, Swoddies are on average stronger on the northern coast, with average ξ/f reaching almost 0.3, comparing to 0.2 on the west coast.

On Fig. 5.6 we show the trajectories of the eddies that were tracked continuously during at least 2 months, separated by layers and polarity. North of 41°N, the trajectories are longer and extend further offshore. Some eddies on the top 200 m (Fig. 5.6 - left) are tracked from the slope till the western boundary of the model domain. There is no clear difference in the trajectories of cyclones and anticyclones. There are some long trajectories near the northern boundary, and eddies that leave the smaller domain and enter again through the northern boundary. This is possible, because in the boundaries of the smaller grid we did not use a classical numerical sponge, which would dissipate the structures, but 2-way nesting that allows a more continuous inter-facial behavior between the grids A1 and A0 (Fig. 1.1).

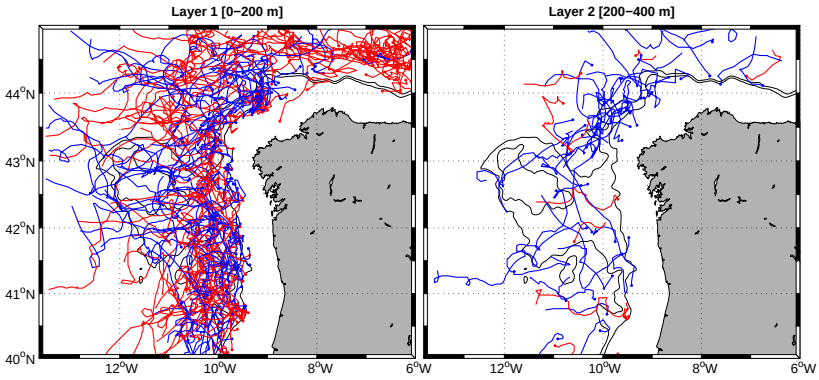

Figure 5.6: *Trajectories of eddies tracked for a minimum of 2 months. Left: cyclones (blue) and anticyclones (red) intensified on the surface layer (0-200 m depth). Right: cyclones and anticyclones intensified on the sub-surface layer (200-400 m depth).*

Further on, in the rest of this chapter we shall focus only on the intensified anticyclones (Swoddies). The IPC is intensified in the upper 200 m of the water column, so it is expected that eddies formed through its destabilization are also intensified at these levels. Moreover, as a poleward eastern

boundary current, the IPC meanders are expected to be mainly anticyclones (rather than cyclones). The results presented in this section show that the average profiles of temperature and salinity of these anticyclones show higher anomalies of salinity and temperature near the surface, when comparing to cyclones. This is consistent with previous studies and observations suggesting that these anticyclones contain IPC saltier and warmer waters in their core. These surface intensified anticyclones are hereinafter referred to as Swoddies.

5.4 Swoddies: Slope Water Eddies on the Winter Season

In this section we focus our analysis on the Swoddies. We start by comparing the model results with satellite SST, to verify if the model is reproducing the same kind of structures. We also analyze in detail the winter of 1989/1990, when various Swoddies were identified and described in the literature (Pingree and Le Cann, 1992b,a). And finally we present some statistics of the Swoddies population.

5.4.1 Comparisons with observations

To evaluate the model skill in reproducing the correct scales and types of structures that were observed, we compared the model with Pathfinder Satellite SST fields on the same days. The comparisons are displayed in figures 5.7, 5.8 and 5.9. Figure 5.7 shows 3 snapshots of the strong IPC event of the winter of 1989/1990, already referred in chapter 4. During this year various Swoddies were observed by satellite and in-situ data on the northern coast, as described in the introduction (Pingree and Le Cann, 1992b,a). Despite the turbulent nature of these processes, some of the structures that were observed are reproduced in the model in great detail and in phase. For example, on the 29^{th} of December of 1989 (top Fig. 5.7), the model shows a very similar mesoscale field with the same kind of structures as observed in

the SST on the northern coast. A perturbation developing north of Cape Ortegal (at around 7.6°W and 44.1°N) is visible both on the satellite and model SST fields. This feature is coincident with the presence of a swoddy detected by the tracking algorithm. Eastward, at around 6.8°W and 44.3°N, another perturbation is noticeable in both fields although not exactly with the same form. On January 3^{rd}, at around 10.3°W and 41.25°N, a model swoddy is clearly identifiable as a turbulent evolution of the IPC. Despite the cloud coverage, a very similar structure is discernible in the SST image of the same date. On January 3^{rd}, on the north coast and east of 8°W, warmer slope waters are visible offshore, both on the model and on satellite SST. One swoddy was identified by the tracking algorithm (centered at 7.2°W, 44.2°N), and is coincident with part of these structures. On January 13^{th}, on the northern coast, warmer slope waters are still visible offshore, and one other swoddy had formed. Offshore of the Galician Rias (9.25°W, 42.5°N) it is visible the presence of a filament of warm water, in both model and satellite, that is also associated to the presence of a swoddy.

Figure 5.8 shows two events for the winter of 1996. Again, the model seems to be reproducing the same kind of observed structures. For example, on January 28^{th}, the eddy detected northwest of Cape Ortegal has a signal in the SST, visible on both model and satellite SST. On February 17^{th}, the current became unstable and various Swoddies were detected on the model, and the SST model anomalies are comparable in scales and positions to those observed in the satellite image.

On December 14^{th} 2006 (top Fig. 5.9), the model SST shows an unstable IPC. Some days later (January 3^{rd} 2007) the current is again well developed and confined to the shelf and slope. The structure of the SST satellite field suggests the presence of Swoddies at 8°W and 44.5°N and at 11°W and 42.5°N, approximately coincident with positions of detected Swoddies in the model.

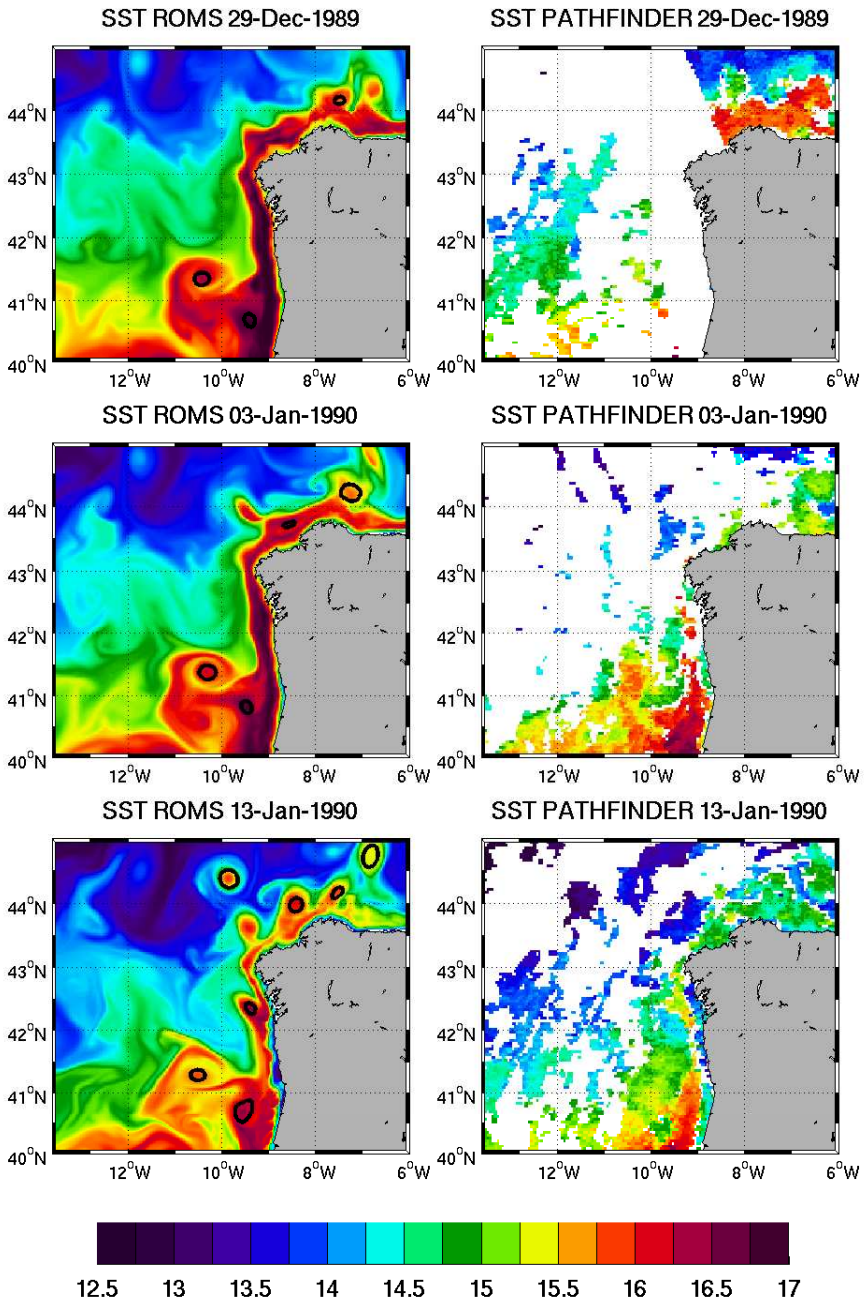

Figure 5.7: *Comparison between model and satellite SST (°C) for various days from the winter 1989/1990. The contours of the Swoddies identified with the eddy tracking are superimposed on ROMS SST fields.*

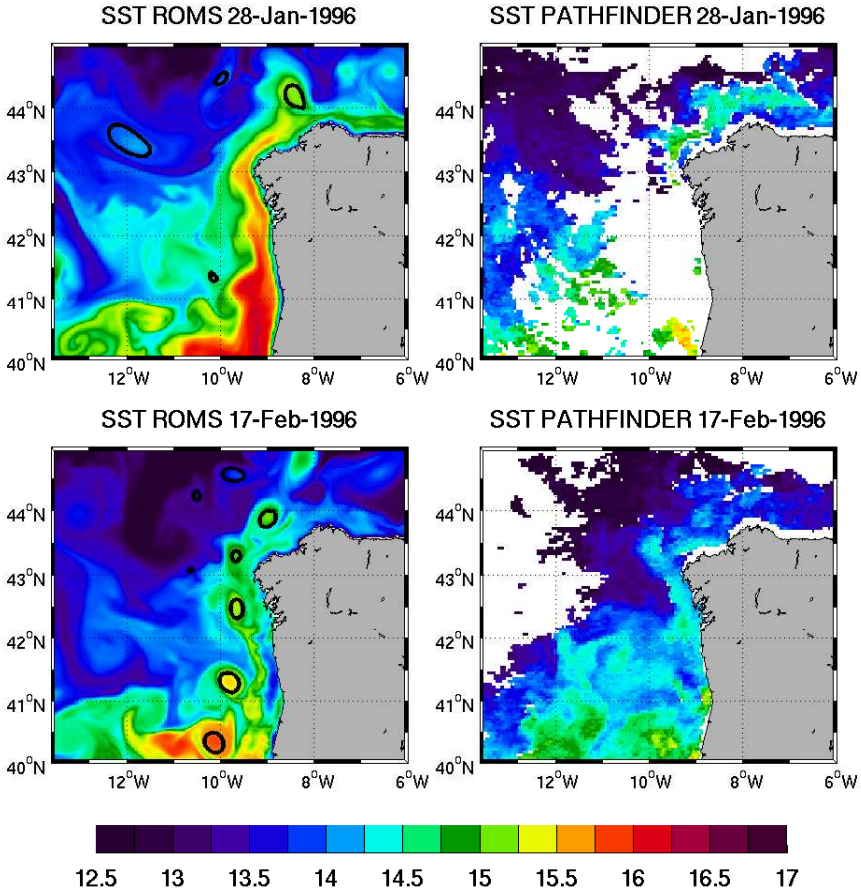

Figure 5.8: *Comparison between model and satellite SST (°C) for various days from the winter 1995/1996. The contours of the Swoddies identified with the eddy tracking are superimposed on ROMS SST fields.*

Figure 5.10 shows 3 comparisons, for March 24^{th} of 1997, January 23^{rd} and March 14^{th} of 1998. On March 24^{th} 1997, some structures are visible on both satellite and model SST fields, and some of them are associated with the presence of Swoddies detected in the model outputs. These are centered at around (9.75°W, 42.25°N), (10°W, 43.1°N), (10.9°W,41.75°N), (9.7°W,40.6°N) and (10.4°W, 41°N). The structures visible in the SST fields of the other 2 dates also show good comparison with the observations. For example, on March 14^{th} of 1998 the satellite SST suggests the presence of the Swoddies centered at (9.8°W,40.8°N), (9.6°W,41.75°N) and (10.25°W,42.5°N).

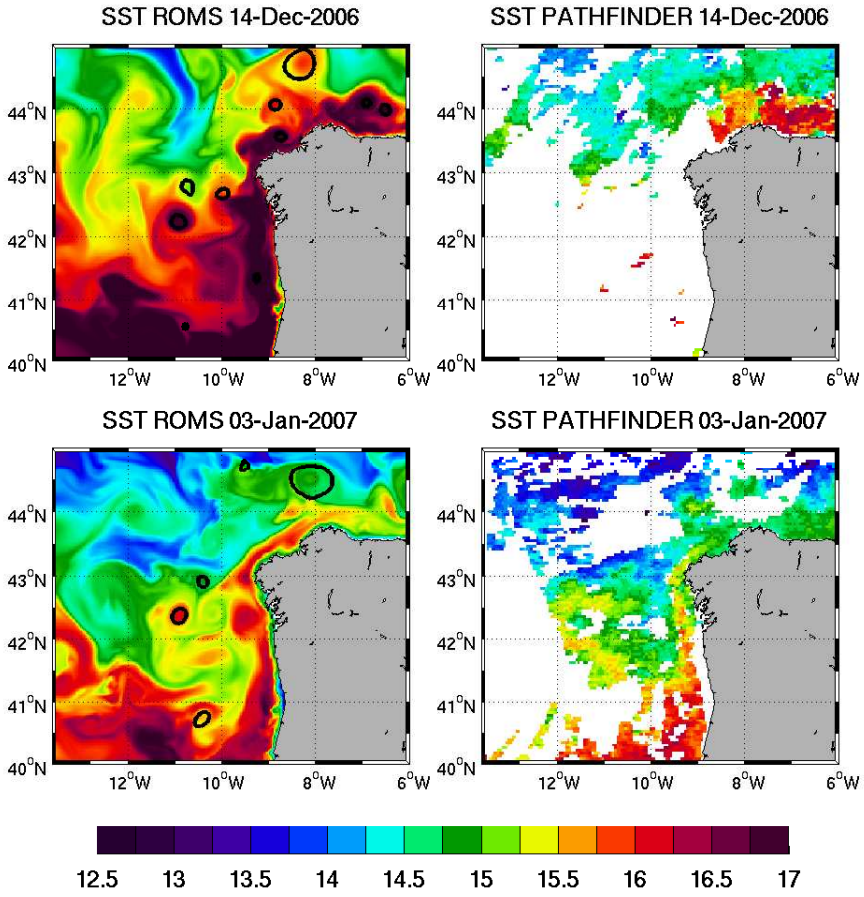

Figure 5.9: *Comparison between model and satellite SST (°C) for various days from the winter 2006/2007. The contours of the Swoddies identified with the eddy tracking are superimposed on ROMS SST fields.*

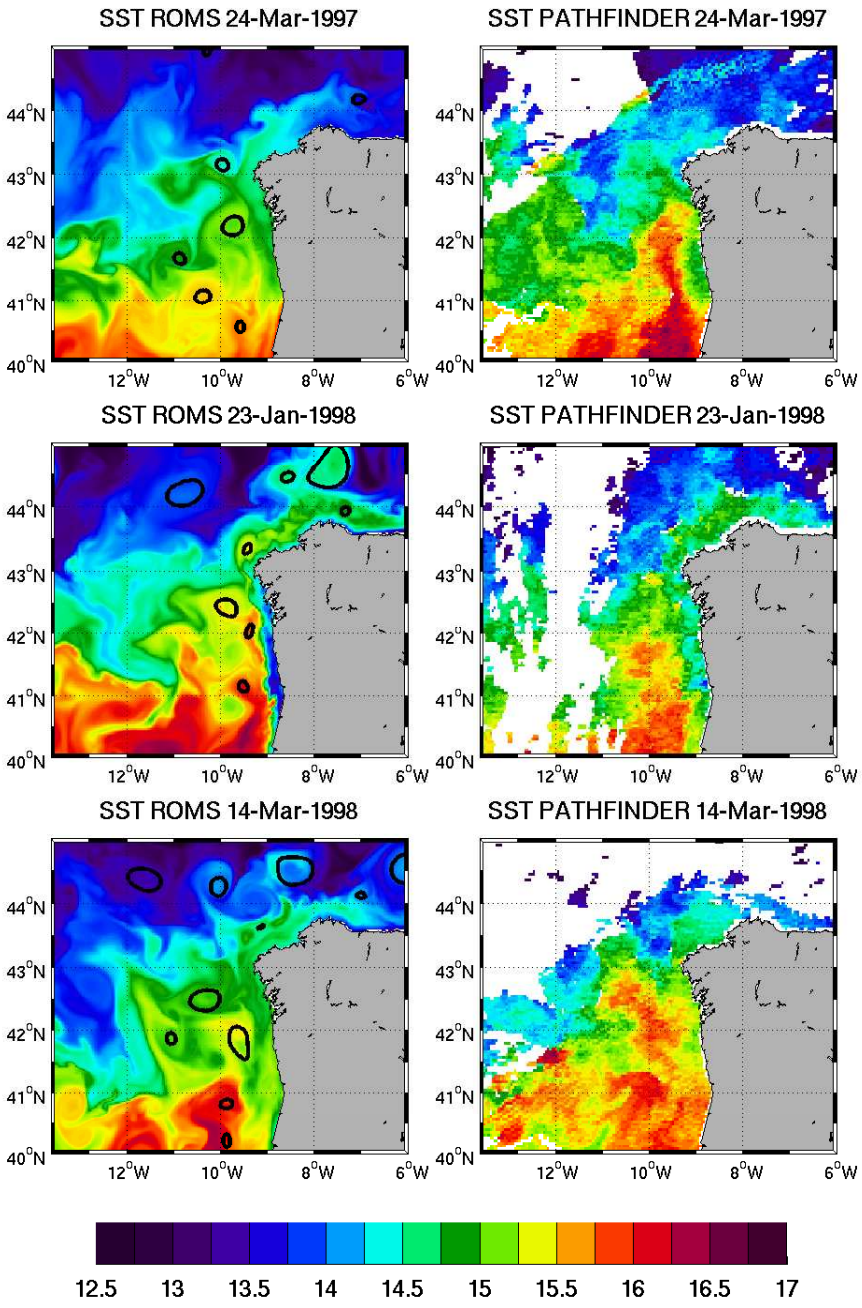

Figure 5.10: *Comparison between model and satellite SST (°C) for various days from different winters. The contours of the Swoddies identified with the eddy tracking are superimposed on ROMS SST fields.*

5.4.2 Description of the 1989/1990 strong IPC Winter

To illustrate some of the processes involved in the Swoddies formation and detachment from the coast, we plotted various fields during the winter 1989/1990 (Fig. 5.11, 5.12 and 5.13), to illustrate the dynamics of the Swoddies evolution. This year is known for its strong IPC event and various Swoddies were observed on the northern coast, both by satellite SST and by in-situ measurements. On December 19^{th}, the IPC is intense and continuous north of 41°N (Fig. 5.11 b), reaching speeds exceeding 0.4 ms^{-1}. The current has a strong signal in the SST (Fig. 5.11 d), and it has negative (positive) vorticity on the inshore (offshore) flank of the current (Fig. 5.11 a). This occurred under an event of strong southwesterly winds (the wind stress field is represented on Fig. 5.11 c and the time series of wind and wind stress on Fig. 5.14). Southerly winds were persistent in December 1989, but became particularly intense after the December 10^{th} (Fig. 5.14 a,b,c). After December 10^{th}, the southwesterly winds intensify and reach maximum intensity around December 16^{th} (see Fig.5.14 a,b,c). After December 20^{th}, the winds calmed down. The intensity of the wind stress is significantly lower by December 24^{th} (Fig. 5.11 g and 5.14 a,b,c). The structure of the current on December 24^{th} is wavier than on the 19^{th} (Fig. 5.11 h,f) suggesting the beginning of destabilization, although no new eddies were formed. On the northern coast, the flow separated from the slope downstream of Cape Ortegal (Fig. 5.11 f), leaving a signature on the SST field (Fig. 5.11 h). On December 29^{th}, the intensity of the averaged wind reduced even more (Fig. 5.11 k and 5.14 a,b,c) and the instabilities of the IPC increased (Fig. 5.11 i,j,l). On January 8^{th}, the instabilities grew even more, and some eddies were formed (Fig. 5.12 a-d). A large eddy is developing on the northern coast, west of Cape Ortegal, in phase and at the same place as the eddy O90 described by Pingree and Le Cann (1992b) (also identified by its signal on the SST, see Fig. 5.7). On January 18^{th}, 5 anticyclones identified by the eddy detection algorithm (Swoddies) are shedding from the slope (Fig. 5.12 e-h). These anticyclones carry IPC warmer and saltier waters offshore. On January 18^{th}, the algo-

rithm also identified various depth-intensified cyclones on the same day (thin blue lines). After January 18^{th}, southerly winds intensified again (see Fig. 5.14 a,b,c) and the current re-establishes (see February 7^{th} fields on Fig. 5.12 i,l). O90 grew by absorbing smaller eddies that developed near Cape Ortegal (see Fig. 5.12 h,l). After February 7^{th}, the wind intensity relaxed again, inverting to calm northerlies on February 13^{th} (see wind on Fig. 5.14 a,b,c). During this relaxation period, some additional Swoddies detached from the slope (Fig. 5.13 a-d). Once again, there are depth-intensified cyclones near the detached anticyclones. From February 17^{th} to March 4^{th}, the two anticyclones positioned near 43°N merged into a bigger anticyclone visible on March 4^{th} fields, centered at 43.3°N and 10.8°W (Fig. 5.13 d,h - or the other fields). This anticyclone propagates westward together with two companion cyclones, located southwestward and southeastward of the anticyclone, and centered at around 43°N (Fig. 5.13 - March 4^{th} and 9^{th}). By this time, the anticyclone O90 grew even bigger, by merging with smaller anticyclones generated near Cape Ortegal. The eddy detection algorithm underestimates the size of the eddies, especially of O90, where the detected radius is 3 times smaller than the effective radius of the eddy (see Fig. 5.13 February 17^{th} or March 4^{th}).

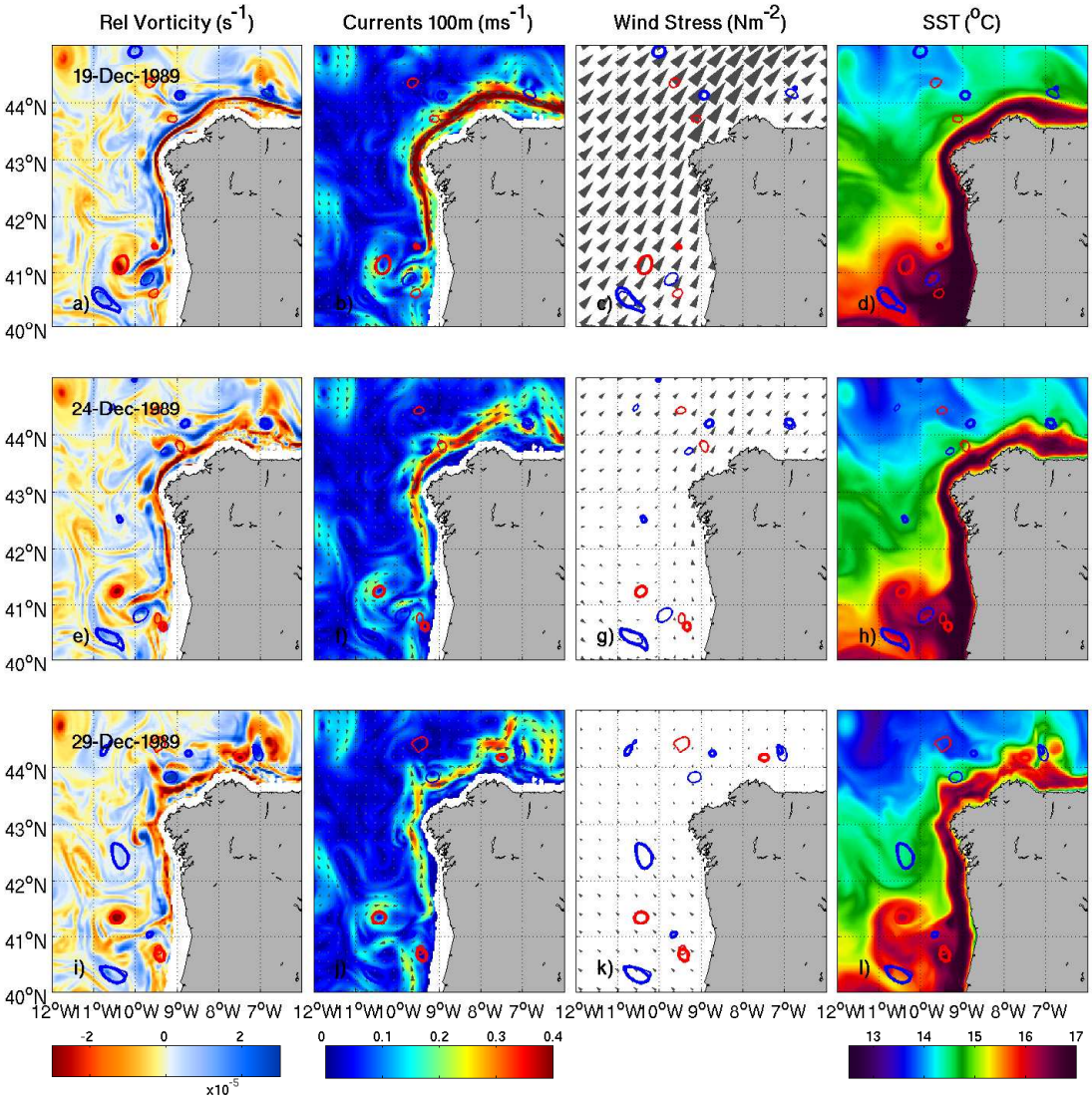

Figure 5.11: *Swoddies in the winter of 1989/1990. The rows represent different days. First column: relative vorticity at 100 m depth; Second column: currents vector field and speed at 100 m depth; Third column; wind stress curl vector field; Fourth column: SST. Surface intensified anticyclones (Swoddies) and cyclones, are identified, respectively, with thick red and blue lines. Anticyclones and cyclones intensified in depth are represented with a thin line, and also in red and blue.*

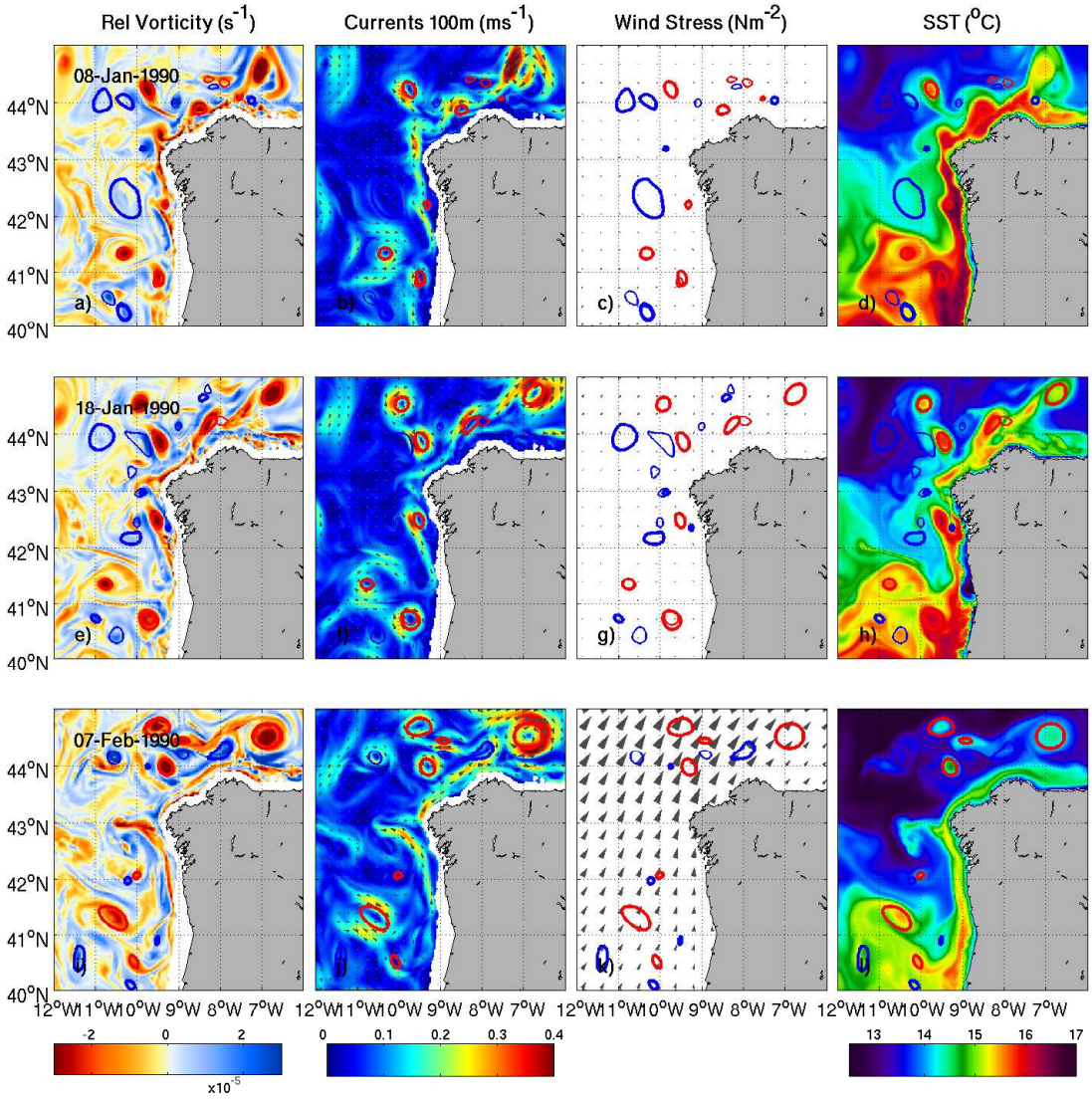

Figure 5.12: *Swoddies in the winter of 1989/1990. The rows represent different days. First column: relative vorticity at 100 m depth; Second column: currents vector field and speed at 100 m depth; Third column; wind stress curl vector field; Fourth column: SST. Surface intensified anticyclones (Swoddies) and cyclones, are identified, respectively, with thick red and blue lines. Anticyclones and cyclones intensified in depth are represented with a thin line, and also in red and blue.*

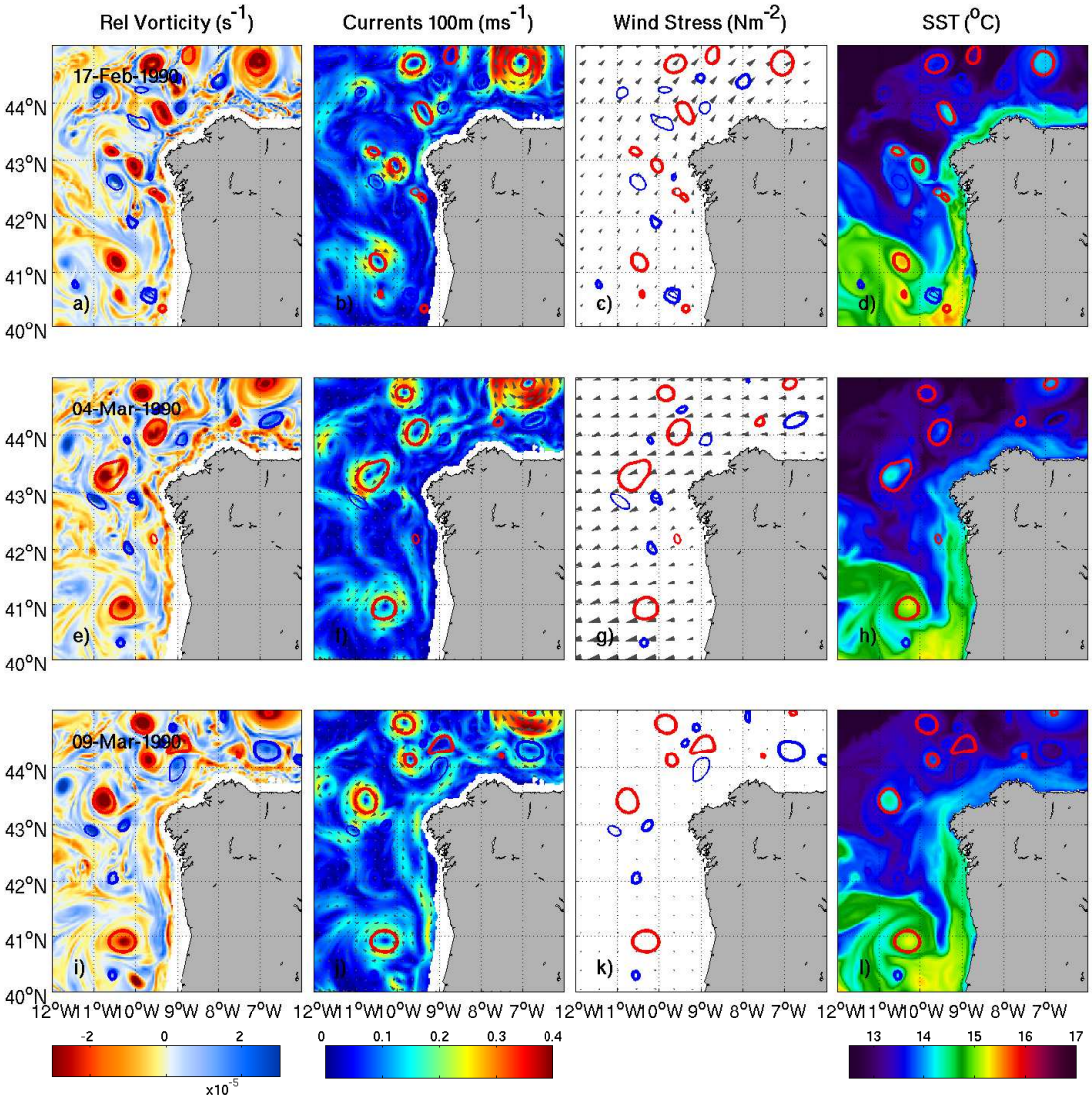

Figure 5.13: *Swoddies in the winter of 1989/1990. The rows represent different days. First column: relative vorticity at 100 m depth; Second column: currents vector field and speed at 100 m depth; Third column; wind stress curl vector field; Fourth column: SST. Surface intensified anticyclones (Swoddies) and cyclones, are identified, respectively, with thick red and blue lines. Anticyclones and cyclones intensified in depth are represented with a thin line, and also in red and blue.*

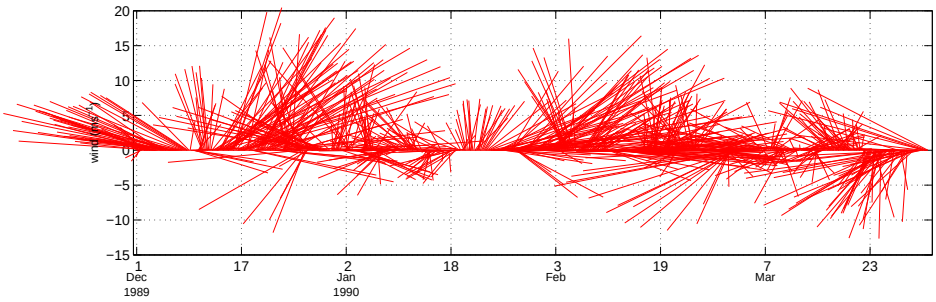

(a)

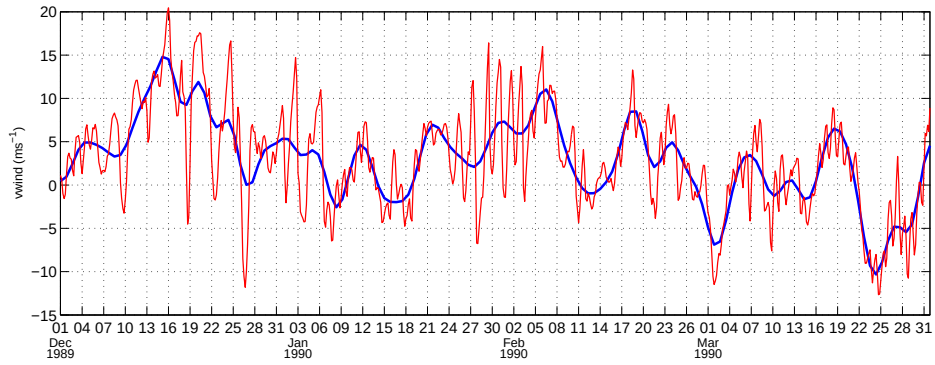

(b)

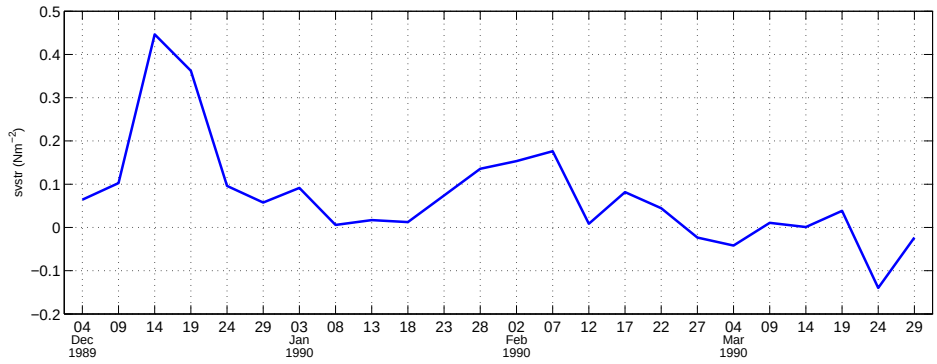

(c)

Figure 5.14: *Evolution in time of the area averaged wind (averaged in domain W - Fig. 2.1). a) wind vectors; b) meridional component of the wind (red) and filtered the scales below 5 days (blue); c) 5 days average meridional wind stress from model outputs and coincident with model fields.*

5.4.3 Swoddies birth-rate time series

The correspondence between observed and modeled Swoddies suggests that the atmospheric forcing variability is important for their formation. Figure 5.15 shows comparisons between time series of the number of Swoddies formed on the slope area (red box in Fig. 5.4), the meridional component of the wind stress, and the net meridional transport. The net meridional transport was computed in the upper 200 m of domain W (Fig. 2.1), across various zonal sections inside domain W, and then averaged, to avoid the influence of local eddies or filaments. The meridional transport shows a strong variability at the synoptic scales (Fig. 5.15 b); and it seems to have a high dependence on the wind (see Fig. 5.15 c - where both series were normalized, to make the visual comparison easier). The correlation between the two series is of 61% (statistically significant at 1% level).

Although Swoddies are continuously forming near the slope, sometimes, various form simultaneously (Fig. 5.15 d), as in January 18^{th} 1990 (Fig. 5.12 e-h). These moments are usually either coincident or occur just after periods of relaxation of southerly winds (Fig. 5.15 d and a - the vertical cyan lines identify the instants when at least 3 Swoddies were formed).

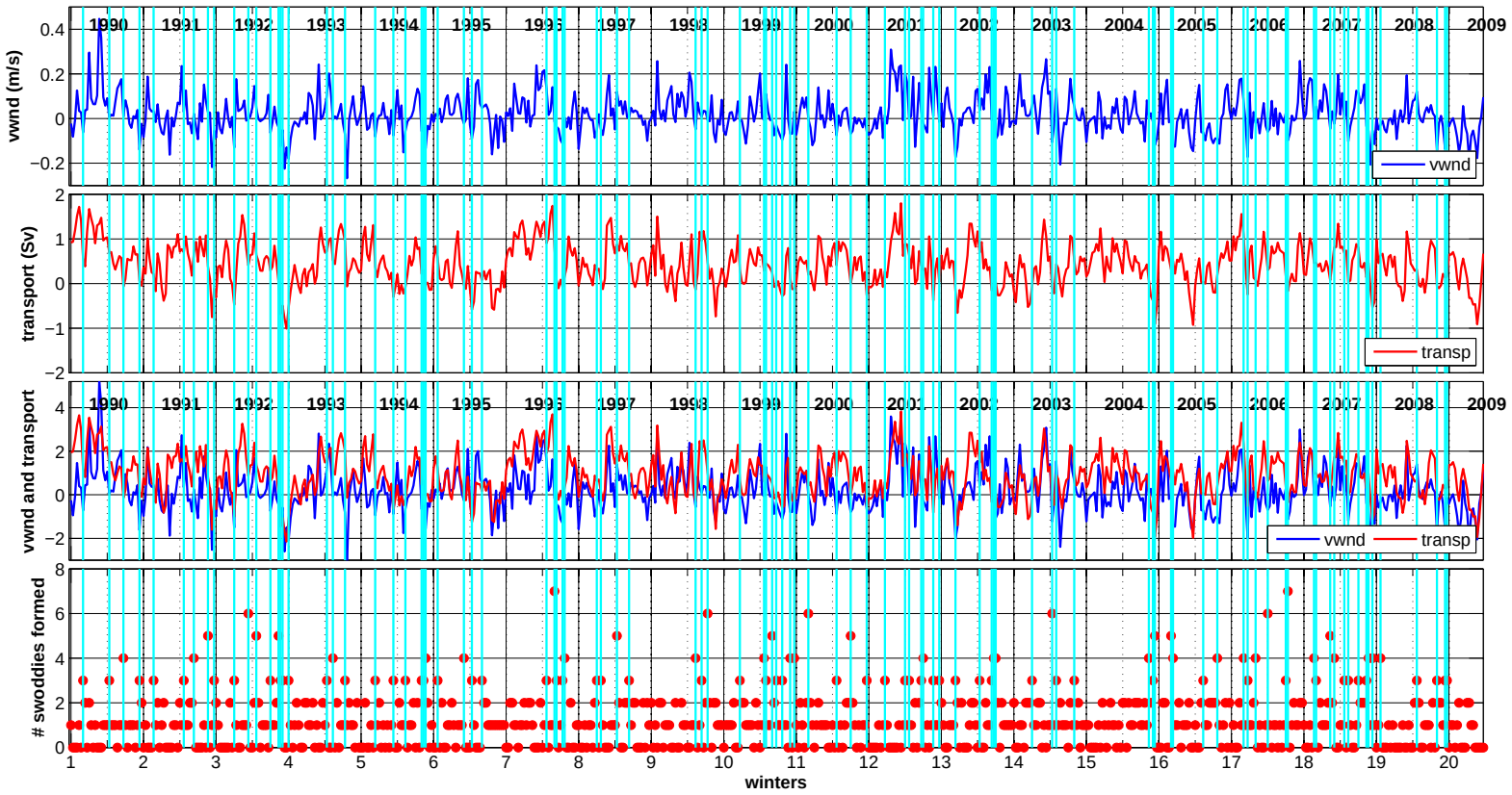

Figure 5.15: *Time series of: (a) meridional component of the wind averaged in domain N (see Fig. 2.1); (b) average net meridional transport, in the upper 200 m and in domain W; (c) time series from plots a) and b), each one divided by its standard deviation; (d) number of Swoddies born at each time record.*

5.4.4 Evolution of Swoddies in time

Two Swoddies were selected, which have been tracked for long periods, to describe the evolution of the vertical structure in time. One was formed on the northern coast and the other on the western coast, and their trajectories are plotted in Fig. 5.16.

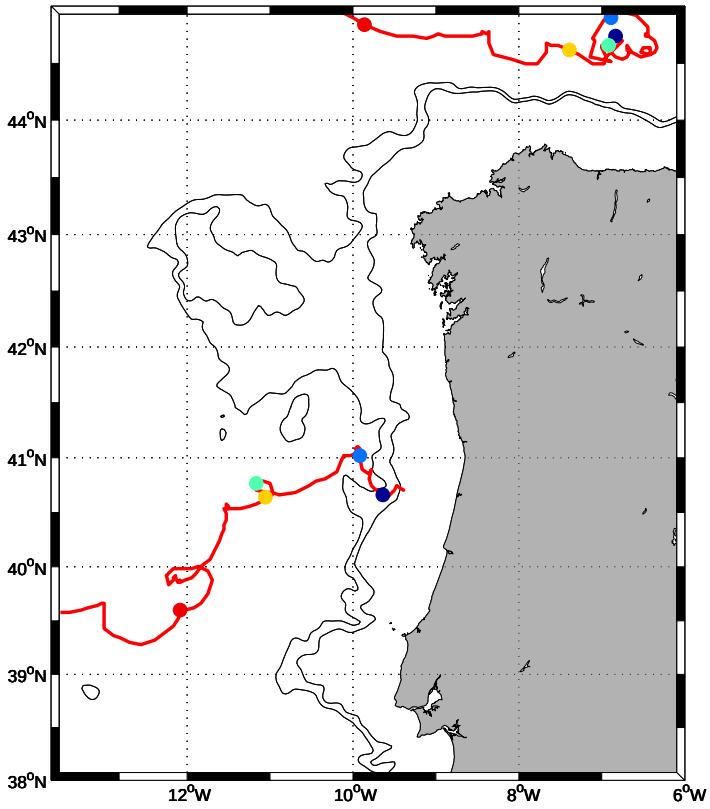

Figure 5.16: *Trajectories of 2 Swoddies that were tracked for longer than a year. The dark blue dots indicate each swoddy formation site. Each dot represents the dates of the zonal sections represented in figures 5.17 and 5.18. The chronological color sequence for each eddy is: dark blue, sea blue, cyan, yellow, red.*

The north coast swoddy corresponds to the model O90, which formation is documented in Fig. 5.11, 5.12 and 5.13. This eddy was first identified by the tracking algorithm on January 13^{th} 1990, few days after a perturbation started developing east of Cape Ortegal, and was followed till January

8^{th} of 1991 when it left the smaller domain through the northern boundary. Figure 5.17 shows the vertical structure of the eddy for 5 different instants in time, indicated in the trajectory plot (Fig. 5.16). On January 13^{th} (Fig. 5.17, January 13^{th}), when the eddy was first detected, it had a diameter of around 60 km. Two months later, on March 4^{th} (Fig. 5.17, March 4^{th}), the eddy increased in size, because it merged with smaller anticyclones that also formed near Cape Ortegal (Fig. 5.11, 5.12 and 5.13), and has a diameter of approximately 100 km. By this time the mixed layer reached deeper, homogenizing the eddy core (Fig. 5.17, March 4^{th}). The mixing is deeper inside the eddy than outside, due to its high salinity values which induce critical static stability soon after cooling. After March, the surface re-stratifies with the summer warming, and by July and August the eddy core is isolated from the surface, hidden by the warmer and saltier surface waters (Fig. 5.17, July 7^{th} and August 11^{th}). The salinity reached higher values at the eddy location. On December 24^{th} of 1990, almost one year after the formation, the mixed layer reached deeper levels again, homogenizing the eddy core again, from the surface to around 200 m depth (Fig. 5.17, December 24^{th}). Fifteen days later, by January 8^{th} of 1991, this swoddy left the smaller model domain through the northern boundary (Fig. 5.16). Figure 5.19 (O90 in red) shows the profiles of temperature, salinity and relative vorticity, averaged in the first month of tracking of this eddy. The relative vorticity maximum is at the surface and its value is around $0.52\xi/f$. Although this eddy formed in the same place and time as the observed O90, their trajectories are completely different, and the real O90 propagated westwards much faster: it was tracked till August 1990, when it was located near 12°W, while the modeled O90 was still near 7.5°W on the same month.

The west coast swoddy was tracked from January 8^{th} 2002 to July 12^{th} 2003. It was generated on the slope, at around 40.7°N and propagated south-eastward, leaving the domain through the western boundary, at the latitude of 39.6°N, and one year and a half later (Fig. 5.16). This swoddy has lower values of relative vorticity than the northern one. Its average relative

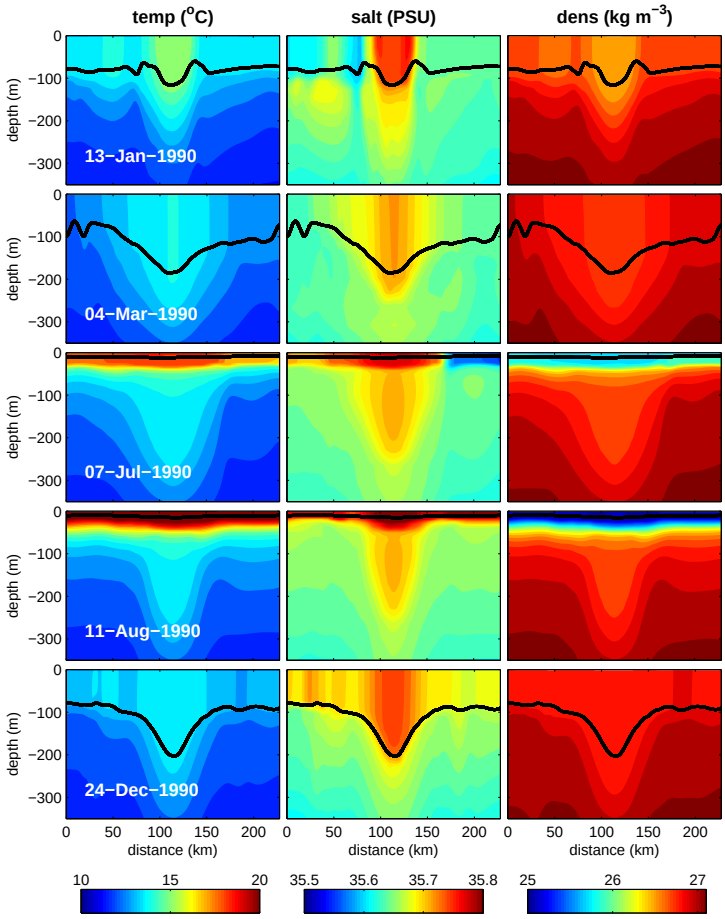

Figure 5.17: *Zonal sections of temperature (left column), salinity (middle column) and density (right column), for different dates. The sections cross the center of the eddy. This Swoddy trajectory is represented in Fig. 5.16, the one that formed on the northern coast. Corresponds to the observed O90.*

vorticity in the first month is also maximum at the surface, but it is around $0.35\xi/f$ (Fig. 5.19 - W02 in green). We show the evolution of its structure in Fig. 5.18. The evolution is not much different from the northern swoddy. On January 28^{th}, it is still close to the slope, and has a diameter of around 50 km (Fig. 5.18, January 28^{th}). On March 14^{th} the diameter almost doubled, the mixed layer deepened, and the eddy core was well mixed. As for O90, vertical convection is stronger inside the eddy, than outside. By June 17^{th}, there is

already a surface re-stratification (and by August 1^{st}), and the eddy core is hidden below the surface. On March 24^{th} of 2003, the density structure is much weakened, showing that the Swoddy is slowing down its rotation. Four months later it leaves the smaller model domain through the western boundary.

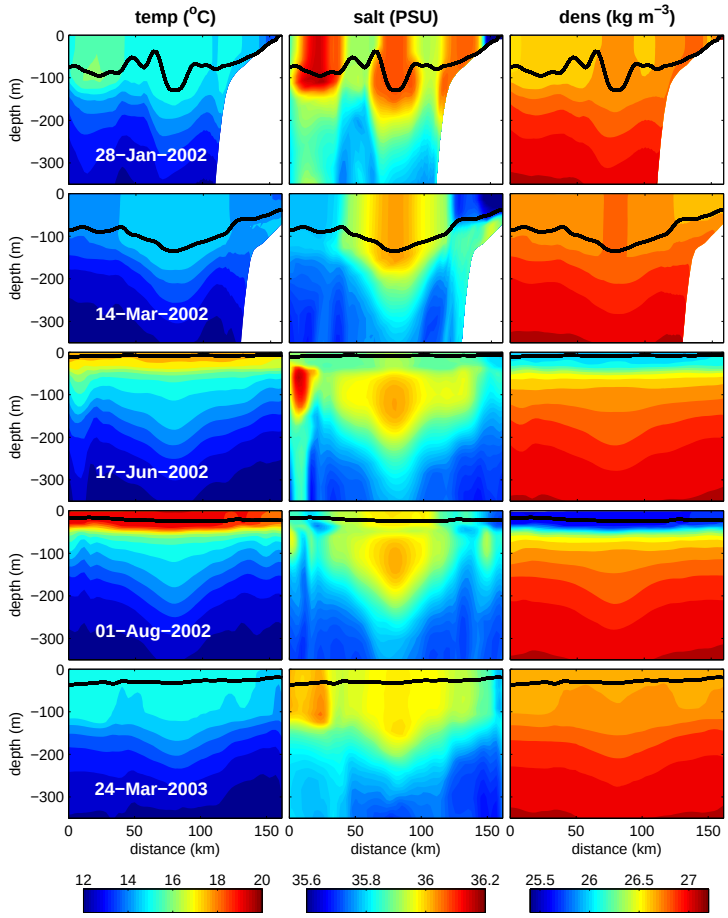

Figure 5.18: *Zonal sections of temperature (left column), salinity (middle column) and density (right column), for different dates. The sections cross the center of the eddy. This Swoddy trajectory is represented in Fig. 5.16, the one that formed on the western coast.*

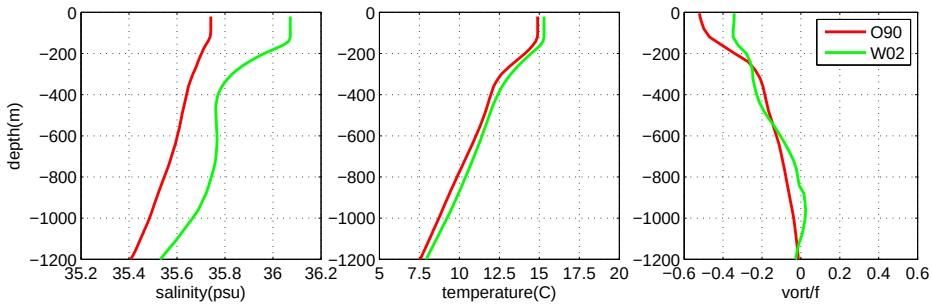

Figure 5.19: *Eddies first month average profiles of salinity (left), temperature (center) and vorticity (right) for the 2 eddies represented in Figures 5.16, 5.17 and 5.18.*

5.4.5 Swoddies sizes

Figure 5.20 shows the distribution of the median radii of the Swoddies. The different plots show the distributions for eddies formed south and north of 43°N (on the left and right columns). On the top row we show the distribution for all eddies tracked for at least 2 consecutive time steps. On the bottom row we plot eddies that were tracked for a minimum of 2 months. There are more eddies being formed at smaller scales, and on both northern and western domains the favorite radius of formation is 9 km (Fig. 5.20 - top). The histograms for the eddies that lived longer (Fig. 5.20 - bottom), show a shift to larger radii, suggesting that the smaller eddies formed at smaller scales do not exist for too long. Probably, the small eddies interact and merge originating larger scale structures. We computed the averaged eddy kinetic energy (EKE) spectrum (Fig. 5.21) for the model output, north of 40°N and west of 9.4°W, to get a rectangular domain without land. We find that the intersection between the k^{-3} and $k^{-\frac{5}{3}}$ slopes occurs at the wavelength of 18 km, which corresponds to the scale of higher energy input, and which is consistent with the large number of eddies formed with median 9 km radius. The largest Swoddies formed and tracked at the western coast have radii of 28-29 km (Fig. 5.20 - left), while the largest on the northern coast reach 33-35 km (Fig. 5.20 - right). It is known that this eddy detecting algorithm

underestimates the radius (Nencioli et al., 2010), so it is probable that the eddies are in generally bigger than the scales we present here. In particular the biggest eddies which are more easily underestimated as shown for the case of O90 in Fig. 5.13.

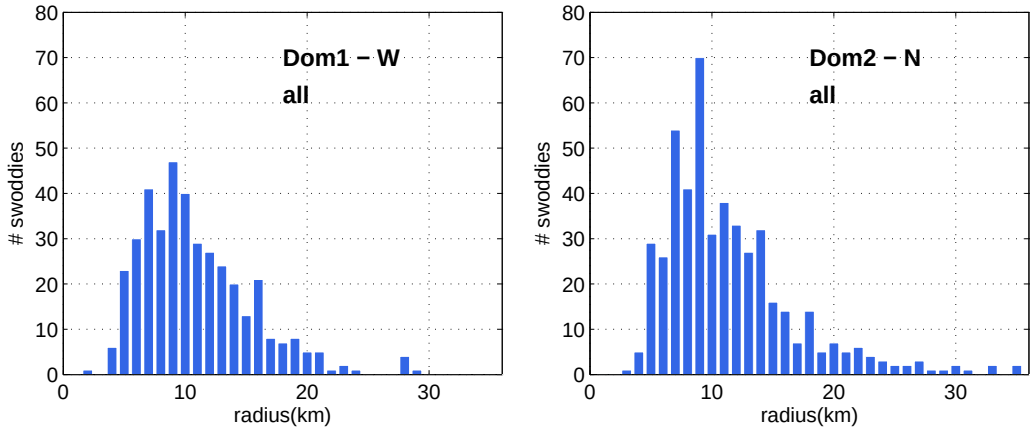

(a)

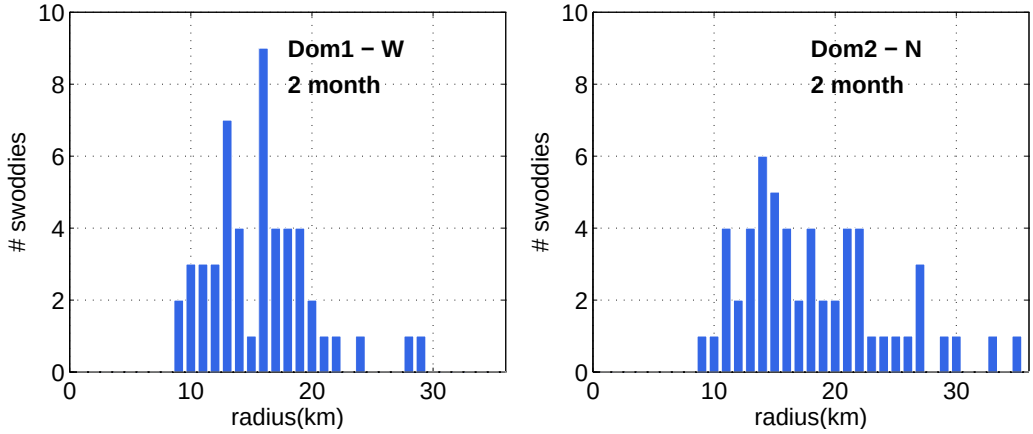

(b)

Figure 5.20: *Histograms of eddies radius. Top: all eddies born at the slope area, from October to March. Bottom: all eddies born at the slope area, from October to March, that were tracked for a minimum of 2 months. Left: formed south of 43° N. Right: formed north of 43° N.*

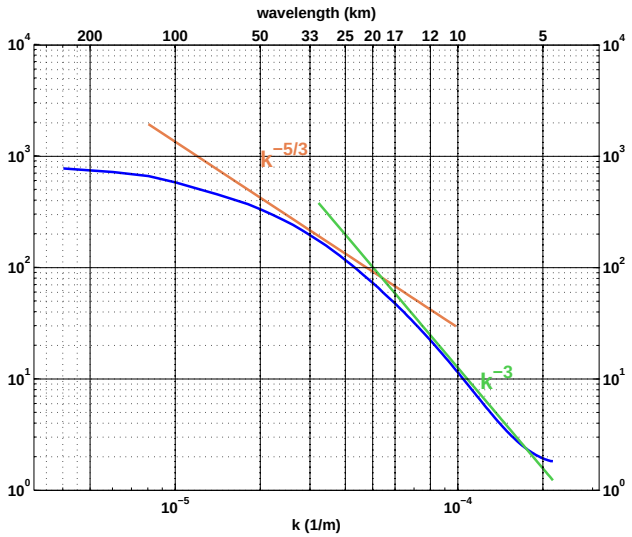

Figure 5.21: *Power spectrum of the EKE for the region confined between 40-44.5° N and 13-9.4° W.*

5.5 Discussion and Conclusions

This chapter makes a first approach to the eddy field and eddy statistics of the North Western Iberian Margin with a particular focus on Swoddies resulting from the the destabilization of the IPC. It is the first time that an analysis of the Swoddies is done in a 20-year high resolution ocean simulation. The eddies that contain the IPC waters are usually anticyclones formed in the slope and dynamically intensified in the top 200 m of the water column. We used an eddy tracking algorithm (Nencioli et al., 2010) to identify and track the eddies that formed in the winter, in the slope, in our model simulation. Most of the information previously known about these eddies was obtained by analysis of satellite SST images that are frequently affected by cloud cover in the winter, or by in-situ observations of sporadic eddies. The model reproduces the formation of some of the Swoddies at the same time and place, and with similar sizes as observed in satellite SST.

Regarding the places of eddies formation, our results show that topography is important. Eddies form mainly near topographic features: cyclones

form mainly where topographic contours veer offshore, in the poleward direction; anticyclones tend to form in places where topographic contours veer inshore. This is in agreement with previous studies of Dubert (1998) and Peliz et al. (2003b) that showed in idealized model configurations representing the IPC, that Swoddies form mainly downstream of topographic accidents. Regarding the instants of formation, we verified that there is a relationship with the wind variability. Periods when a number of Swoddies (more than 3) form, at the same time, in different places along the slope, are usually coincident with the relaxation of southerly winds. We also verified that the meridional transport over the slope and shelf in the winter (net meridional transport on domain W - Fig. 2.1), which is dominated by the IPC, presents a large synoptic variability. The transport variability at the synoptic scales is mainly forced by the variability of the meridional component of the wind (the correlation between both time series is 61%). A sudden decrease in the intensity of the IPC, results in the development of instabilities and formation of eddies. In the strong IPC winter of 1989/1990, there were two instants when various eddies were formed, both coincident with the relaxation of southerly winds.

The shedding of Swoddies from the slope was described on two different occasions, and on both, it was accompanied by the shedding of deeper layer cyclones. This process of deep cyclogenesis was already described in Peliz et al. (2003b) that describes the destabilization of the IPC by a process of baroclinic instability. In the same study it was also demonstrated the importance of the deep cyclones for the separation of the Swoddies from the slope and their propagation offshore. We verified that in our model a number of deep cyclones are also produced at the Swoddies shedding times, and we observed clear signs of interaction between Swoddies and deep cyclones. One example is presented in Fig. 5.13 in March 1990, where two cyclones propagate westward together with a surface anticyclone (swoddy). As the eddies interact between each other, their trajectory is mostly a result of mutually induced movements, between close enough eddies, centered at the same vertical level or at different levels. As Peliz et al. (2003b) showed, deep

cyclones are important in pushing surface anticyclones offshore; and Carton et al. (2013) showed in analytical and numerical studies that a deep Meddy can also interact with a surface anticyclone, and this interaction can explain the U-shape trajectory of the surface anticyclone F90, observed by Pingree and Le Cann (1992b). These complex interactions between eddies, at the same or at different depths, explains why the model does not reproduce the trajectories of the Swoddies, although it is able to reproduce their instants and places of formation. For example, the real O90 was observed to propagate from 7°W to 12°W (Pingree and Le Cann, 1992b), while the one formed in the model only propagated to 7.5°W in the same amount of time.

The favorite radius for eddy formation is 9 km, on both northern and western coasts. The results suggest that eddies form at these scales, but they rapidly interact with each other originating larger eddies. The ones that are tracked for longer periods are usually larger. The EKE spectrum is in agreement with these scales. According to the geostrophic turbulence theory there is an inverse energy cascade, from smaller to larger scales (Kolmogorov $-\frac{5}{3}$ spectrum), while enstrophy cascade is direct, from larger to smaller scales (-3 spectrum) (Mcwilliams, 2006; Vallis, 2006). We searched for the wavelength for which the tangent to the spectrum is the power law $k^{-\frac{5}{3}}$, and the wavelength for which the tangent is the power law is k^{-3}. The intersection between both lines gives the scales of energy input, which in this case is a wavelength of 18 km that corresponds to eddies of 9 km radius.

The Swoddies that were observed in the Bay of Biscay (Pingree and Le Cann, 1992b,a) had larger radii than the values we obtain in general. As was shown in the case of O90, the eddy detection algorithm underestimates the true radius of the eddy, and this happens especially for the larger eddies. Even though, analyzing our eddy population it is clear that eddies as large as O90 are exceptional, and they result from the merging of various smaller eddies with the same polarity or possibly from exceptional periods of standing meandering. Serpette et al. (2006) in an analysis of drifters in this region, also report the observation of eddies with smaller sizes than the ones

observed in the Bay of Biscay.

We also verified that Swoddies can survive winter deep convection that homogenizes their core. Convection is deeper inside the eddy than outside, suggesting that Swoddies can have an important role in ventilating central waters. It is also noteworthy the fact that one swoddy was tracked for a period of 1.5 years, especially remarkable since models tend to be over dissipative.

Conclusions

This thesis studies the IPC, its seasonal cycle, and interannual variability.

Regarding the average seasonal cycle, it was shown that there is an almost permanent average alongshore current over the slope, divided in 3 different cores. The Iberian Poleward Current (IPC), occupying the top 250 m, the Upper Slope Countercurrent (USCC), equatorward and centered at around 400 m depth and the Iberian Poleward Slope Undercurrent (IPSU), that extends from 600 m to 1200 m depth. The IPC starts developing near the shelf break at around 200 m depth, already during the summer, when the shelf and upper slope are occupied by the southward flowing upwelling jet. In December and January, the IPC intensifies and its core migrates to the surface, becoming a surface intensified jet. From February to May, the current weakens and part of it propagates offshore.

Vorticity balances over the slope confirm that JEBAR is the most important term forcing the IPC, but as advection terms become important, the northward density flux diminishes the meridional density gradients, resulting in a decrease of JEBAR at the core of the IPC. Due to this effect, its contribution is higher in summer than in winter. In December and January, there is an important contribution for the IPC from the positive wind stress (southerly winds) over the slope.

The results confirmed that the IPC undergoes a strong interannual variability. It was found that from November to January, the IPC magnitude depends mostly on the intensity of the southerly winds. It was also verified that this is not true in September, when the intensity of the northward

transport is related to larger scale wind stress curl. The latter affects the meridional density gradients in the west coast, changing JEBAR, which is the main forcing of poleward flow over the slope in September. Years of strong IPC result in higher transport of heat and salt, leading to positive anomalies of temperature and salinity. However, local air-sea fluxes are also important and can counteract the effect of advection. It was also observed that the sub-seasonal variability can be large, and the analysis based on only one or two months may not be representative of the northward transport of heat and salt on the entire winter season.

Regarding the formation of Swoddies, it was found that there is a relation between the eddies formed at each instant and the wind variability. Usually the time periods when various Swoddies are formed simultaneously correspond to periods of relaxation of southerly winds, which also coincide with periods of relaxation of the IPC. The IPC shows strong variability at the synoptic scales, responding in large part to the wind variability. It was also verified, as suggested in previous studies, that Swoddies usually form downstream of major topographic features, where topographic contours veer inshore in the poleward direction; and that their formation is usually accompanied by the formation of deep cyclones, that have an important role in the shedding of the Swoddies from the slope.

Since the boundaries of the simulation are climatological, it is not represented any effect of the large scale variability on the northwestern Iberian shelf/slope regions. However, it was shown that this simulation is reproducing a large part of the observed interannual and synoptic variability, which suggests that the forcing of this system variability is essentially local.

This thesis contributes to the understanding of the ocean circulation in the Northwestern Iberian region by answering some of the questions left open by previous studies. However, the picture is not yet complete and several other questions remain unanswered:

- What is the effective role of the Swoddies in the transport of heat and salt to the open ocean? Are they responsible for the higher salinity values

observed in the ENACW?

- What is the mean circulation south of our region of focus? The IPC seems to extend further south and to be connected with the Gulf of Cadiz, but the average circulation in the southwestern Iberia region is not fully understood.

- On the southwestern part, the currents at the surface seem to be strongly influenced by the currents at depth, for example Meddies have a strong signal at the surface currents (Serra et al., 2010). Also, at the latitudes of Cape Roca it seems that the Mediterranean Undercurrent has a strong effect on the surface IPC (Nolasco et al., 2013). These studies suggest that, at these latitudes, there is a stronger connection between the currents at the surface and at deeper levels. Does this give origin to barotropic eddies containing Mediterranean water at deeper levels and ENACWst near the surface? What are the main characteristics of these eddies?

- It was shown that the IPC can destabilize few days after the relaxation of southerly winds, giving origin to eddies that transport the IPC waters offshore. However the details of the destabilization and eddy generation were not explored. Further studies are required, in order to understand why the destabilization occurs timely after the relaxation, and the characteristics of the eddy field that is produced and its evolution.

- The IPC forcing can be more localized or stronger at some latitudes, leading to the development of coastal waves. What is the role of Coastal Trapped Waves in transporting the signal of the IPC northward and eastward on the northern coast?

- Finally, the biological consequences of these processes remain to be explored. In what sense can this affect larval retention in the winter? Winters of strong average southerly winds were expected to favor retention, but our results suggest that short wind relaxation periods can probably result in a dramatic decrease of the retention rates.

References

Aguiar, A., Peliz, A., Carton, X., 2013. A census of Meddies in a long-term high-resolution simulation. Progress in Oceanography 116, 80–94.

Ambar, I., 1985. Seis meses de medições de correntes, temperatura e salinidade na vertente continental portuguesa a 40°N. Tech. rep., Dep. Fisica, Centro de Geofísica, Universidade de Lisboa.

Ambar, I., Fiúza, A., 1994. Some features of the portugal current system: a poleward slope undercurrent, an upwelling-related summer southward flow and an autumn-winter poleward coastal surface current. In: Proceedings of the Second International Conference on Air-Sea Interaction and on Meteorology and Oceanography of the Coastal Zone. pp. 286–287.

Antonov, J., Locarnini, R., Boyer, T., Mishonov, A., Garcia, H., 2006. World Ocean Atlas 2005 Volume 2: Salinity. U.S. Government Printing Office, Washington, D.C.

Beckmann, A., Haidvogel, D. B., 1993. Numerical Simulation of Flow around a Tall Isolated Seamount. Part I: Problem Formulation and Model Accuracy. Journal of Physical Oceanography 23, 1736–1753.

Cabrillo, R. S., González-Pola, C., Ruíz-Vilarreal, M., Montero, A. L., 2011. Mixed layer depth (MLD) variability in the southern Bay of Biscay. Deepening of winter MLDs concurrent with generalized upper water warming trends? Ocean Dynamics 61, 1215–1235.

Carton, X., Le Cann, B., Serpette, A., Dubert, J., 2013. Interactions of surface and deep anticyclonic eddies in the Bay of Biscay. Journal of Marine Systems 110, 45–59.

Casey, K., Brandon, T., Cornillon, P., Evans, R., 2010. The past, present and future of the avhrr pathfinder sst program. In: Barale, V., Gower, J., Alberotanza, L. (Eds.), Oceanography from Space: Revisited. Springer Netherlands, pp. 273–287.

Chainho, P., Costa, J., Chaves, M., Lane, M., Dauer, D., Costa, M., 2006. Seasonal and spatial patterns of distribution of subtidal benthic invertebrate communities in the Mondego River, Portugal - a poikilohaline estuary. Hydrobiologia 74, 555–559.

Colas, F., McWilliams, J. C., Capet, X., Kurian, J., 2012. Heat balance and eddies in the Peru-Chile current system. Climate Dynamics 39, 509–529.

Couvelard, X., Marchesiello, P., Gordeau, L., Lefevre, J., 2008. Barotropic Zonal Jets Induced by Islands in the Southwest Pacific. Journal of Physical Oceanography 38, 2185–2204.

da Silva, A., Young, A. C., Levitus, S., 1994. Atlas of surface marine data 1994, volume 1: Algorithms and procedures. NOAA Atlas NESDIS 6, U.S. Department of Commerce, Washington, D.C.

Daniault, N., Mazé, J., Arhan, M., 1994. Circulation and mixing of mediterranean water west of the iberian peninsula. Deep-Sea Research 41 (11/12), 1685–1714.

Debreu, L., Marchesiello, P., Penven, P., Gambon, G., 2012. Two-way nesting in split-explicit ocean models: algorithms, implementation and validation. Ocean Modelling 49-50, 1–21.

Dong, C., Lin, X., Liu, Y., Nencioli, F., Chao, Y., Guan, Y., Chen, D., Dickey, T., McWilliams, J., 2012. Three-dimensional oceanic eddy analysis

in the Southern California Bight from a numerical product. Journal of Geophysical Research 117, 1–17.

Dubert, J., 1998. Dynamique du Système de Courants vers le Pôle au Voisinage de la Pente Continentale à l'Ouest et au Nord de la Péninsule Ibérique. Ph.D. thesis, University of Bretagne Occidentale, available from the Department of Physics, University of Aveiro, Portugal.

Fairall, C., Bradley, E., Rogers, D., Edson, J., Young, G., 1996. Bulk parameterization of air-sea fluxes for Tropical Ocean - Global Atmosphere Coupled-Ocean Atmosphere Response Experiment. Journal of Geophysical Research 101, 3747–3764.

Fiúza, A., Hamman, M., Ambar, I., Díaz del Río, G., González, N., Cabanas, J., 1998. Water masses and their circulation off western iberia during may 1993. Deep-Sea Research I 45, 1127–1160.

Friocourt, Y., Blanke, B., Drijfhout, S., Speich, S., 2008a. On the Dynamics of the Slope Current System along the West European Margin. Part II: Analytical Calculations and Numerical Simulations with Seasonal Forcing. Journal of Physical Oceanography 38, 2619–2638.

Friocourt, Y., Drijfhout, S., Blanke, B., 2008b. On the Dynamics of the Slope Current System along the West European Margin. Part I: Analytical Calculations and Numerical Simulations with Steady-State Forcing. Journal of Physical Oceanography 38, 2597–2618.

Friocourt, Y., Levier, B., Speich, S., Blanke, B. Drijfhout, S., 2007. A regional numerical ocean model of the circulation in the Bay of Biscay. Journal of Geophysical Research 112, C09008.

Frouin, R., Fiúza, A., Ambar, I., Boyd, T., 1990. Observations of a poleward surface current off the coasts of Portugal and Spain during winter. Journal of Geophysical Research 95 (C1), 679–691.

Garcia-Soto, C., 2004. 'Prestige' oil spill and Navidad flow. Journal of the Marine Biological Association of the United Kingdom 94, 293–300.

Garcia-Soto, C., Pingree, R., 2011. Atlantic Multidecadal Oscillation (AMO) and sea surface temperature in the Bay of Biscay and adjacent regions. Journal of the Marine Biological Association of the United Kingdom 92, 213–234.

Garcia-Soto, C., Pingree, R., Valdés, L., 2002. Navidad development in the southern bay of biscay: Climate change and swoddy structure from remote sensing and in situ measurements. Journal of Geophysical Research 107, 28, doi:10.1029/2001JC001012.

Guo, X., Hukuda, H., Miyazawa, Y., Yamagata, T., 2003. A Triply Nested Ocean Model for Simulating the Kuroshio - Roles of Horizontal Resolution on JEBAR. Journal of Physical Oceanography 33, 146–169.

Haynes, R., Barton, E., Pilling, I., 1993. Development, persistence, and variability of upwelling filaments off the Atlantic coast of the Iberian Peninsula. Journal of Geophysical Research 98 (C12), 22681–22692.

Hedstrom, K. S., 2009. Technical manual for a coupled sea-ice/ocean circulation model (version 3). Technical report, Artic Region Supercomputing Center, University of Alaska Faibanks.

Holland, W. R., 1973. Baroclinic and Topographic Influences on the Transport in the Western Boundary Currents. Geophysical Fluid Dynamics 4, 187–210.

Huthnance, J., 1984. Slope currents and jebar. Journal of Physical Oceanography 14, 795–810.

Large, W. G., Mcwilliams, J. C., Doney, S. C., 1994. Oceanic vertical mixing: A review and a model with a nonlocal boundary layer parameterization. Reviews of Geophysics 32 (4), 363–403.

Le Cann, B., Serpette, A., 2009. Intense warm and saline upper ocean inflow in the southern Bay of Biscay in autumn-winter 2006-2007. Continental Shelf Research 29, 1014–1025.

Le Hénaff, M., Roublou, L., Bouffard, J., 2011. Characterizing the Navidad current interannual variability using coastal altimetry. Ocean Dynamics 61, 425–437.

Lee, S., Pelegri, J. L., Kroll, J., 2001. Slope Control in Western Boundary Currents. Journal of Physical Oceanography 31, 3349–3360.

Liu, W. T., Katsaros, K. B., Businger, J. A., 1979. Bulk Parameterization of Air-Sea Exchanges of Heat and Water Vapor Including the Molecular Constrains at the Interface. Journal of Atmospheric Sciences 36, 1722–1735.

Llope, M., Anadón, R., Viesca, L., Quevedo, M., González-Quirós, R., Stenseth, N., 2006. Hydrography of the southern Bay of Biscay shelf-break region: Integrating the multiscale physical variability over the period 1993-2003. Journal of Geophysical Research 111, C09021.

Locarnini, R., Mishonov, A., Antonov, J., Boyer, T., Garcia, H., 2006. World Ocean Atlas 2005 Volume 1: Temperature. U.S. Government Printing Office, Washington, D.C.

Marchesiello, P., McWilliams, J. C., Shchepetkin, A., 2001. Open boundary conditions for long-term integration of regional oceanic models. Ocean Modelling 3 (1), 20.

Marsh, T., Dale, M., 2002. The UK floods of 2000-2001: A hydrometeorological appraisal. Water and Environment Journal 16, 180–188.

Martins, C., Hamann, M., Fiúza, A., 2002. Surface circulation in the eastern north atlantic, from drifters and altimetry. Journal of Geophysical Research 107 (C12), 3217, doi:10.1029/2000JC000345.

Mcwilliams, J., 2006. Fundamentals of Geophysical Fluid Dynamics. Cambridge University Press.

Mertz, G., Wright, D. G., 1992. Interpretations of the JEBAR Term. Journal of Physical Oceanography 22, 301–305.

Nencioli, F., Dong, C., Dickey, T., Washburn, L., McWilliams, J., 2010. A vector geometry based eddy detection algorithm and its application to high-resolution numerical model products and high-frequency radar surface velocities in the Southern California Bight. Journal of Atmospheric and Oceanic Technology 27, 564–579.

Neves, F., 2010. Dynamics and hydrology of the tagus estuary: results from in situ observations. Ph.D. thesis, Universidade de Lisboa.

Nolasco, R., Pires, A., Cordeiro, N., Le Cann, B., Dubert, J., 2013. A high-resolution modeling study of the Western Iberian Margin mean and seasonal upper ocean circulation. Ocean Dynamics 63, 1041–1062.

Oliveira, P., Peliz, A., Dubert, J., Rosa, T., Santos, A., 2004. Winter geostrophic currents and eddies in the western Iberia coastal transition zone. Deep Sea Research I 51, 367–381.

Otero, P., Ruiz-Villarreal, M., Peliz, A., Cabanas, J., Jun. 2010. Climatology and reconstruction of runoff time series in northwest Iberia: influence in the shelf buoyancy budget off Ría de Vigo. Scientia Marina 74 (2), 247–266.

Peliz, A., Boutov, D., Cardoso, R., Delgado, J., Soares, P., 2012. The Gulf of Cadiz-Alboran Sea sub-basin: Model setup, exchange and seasonal variability. Ocean Modelling 61, 49–67.

Peliz, A., Boutov, D., Teles-Machado, A., 2013. The Alboran sea mesoscale in a long term high resolution simulation: Statistical analysis. Ocean Modelling 72, 32–52.

Peliz, A., Dubert, J., Haidvogel, D., 2003a. Subinertial response of a density driven eastern boundary poleward current to wind forcing. Journal of Physical Oceanography 33, 1633–1650.

Peliz, A., Dubert, J., Haidvogel, D., Le Cann, B., 2003b. Generation and unstable evolution of a density-driven eastern poleward current. Journal of Geophysical Research 108, 3268, doi:10.1029/2002JC001443.

Peliz, A., Dubert, J., Marchesiello, P., Teles-Machado, A., 2007. Surface circulation in the Gulf of Cadiz: Model and mean flow structure. Journal of Geophysical Research (Oceans) 112, C11015.

Peliz, A., Dubert, J., Santos, A., Oliveira, P., Le Cann, B., 2005. Winter upper ocean circulation in the Western Iberian Basin - Fronts, Eddies and Poleward Flows: an overview. Deep Sea Research I 52, 621–646.

Peliz, A., Rosa, T. L., Santos, A. M. P., Pissarra, J. L., 2002. Fronts, jets, and counter flows in the western iberian upwelling system. Journal of Marine Systems 35, 61–77.

Penven, P., Debreu, L., Marchesiello, P., McWilliams, J., 2006. Evaluation and application of the ROMS 1-way embedding procedure to the central california upwelling system. Ocean Modelling 12, 157–187.

Penven, P., Marchesiello, P., Debreu, L., Lefevre, J., 2008. Software tools for pre- and post-processing of oceanic regional simulations. Environmental Modelling & Software 23 (5), 660 – 662.

Pingree, R., Le Cann, B., 1990. Structure, strength and seasonality of the slope currents in the bay of biscay region. Journal of the Marine Biology Association of U.K. 70, 857–885.

Pingree, R., Le Cann, B., 1992a. Anticyclonic eddy X91 in the southern bay of biscay, may 1991 to february 1992. Journal of Geophysical Research 97, 14353–14367.

Pingree, R., Le Cann, B., 1992b. Three anticyclonic slope water oceanic eddies (swoddies) in the southern bay of biscay in 1990. Deep-Sea Research I 39, 1147–1175.

Prieto, E., González-Pola, C., Lavín, A., Sánchez, R., Ruiz-Villarreal, M., 2013. Seasonality of intermediate waters hydrography west of the Iberian Peninsula from an 8 yr semiannual time series of an oceanographic section. Ocean Science 9, 411–429.

Relvas, P., Barton, E., 2002. Mesoscale patterns in the Cape São Vicente (Iberian Peninsula) upwelling region. Journal of Geophysical Research 107, 3164, doi:10.1029/2000JC000456.

Sanz, J. L., Acosta, J., Esteras, M., Herranz, P., Palomo, C., Sandoval., N., 1991. Prospección geofísica del Estrecho de Gibraltar (Resultados del programa Hércules 1980-1983). Publicaciones especiales del Instituto Español de Oceanografía, Instituto Español de Oceanografía.

Serpette, A., Le Cann, B., Colas, F., 2006. Lagrangian circulation of the North Atlantic Central Water over the abyssal plain and continental slopes of the Bay of Biscay: description of selected mesoscale features. Scientia Marina 70, 27–42.

Serra, N., Ambar, I., Boutov, D., 2010. Surface expression of Mediterranean Water dipoles and their contribution to the shelf/slope - open ocean exchange. Ocean Science 6, 191–209.

Shchepetkin, A. F., McWilliams, J. C., March 2003. A method for computing horizontal pressure-gradient force in an oceanic model with a non-aligned vertical coordinate. Journal of Geophysical Research - Oceans 108 (C3), 3090.

Shchepetkin, A. F., McWilliams, J. C., 2005. The regional oceanic modeling system (ROMS): a split-explicit, free-surface, topography-following-coordinate oceanic model. Ocean Modelling 9, 347–404.

Smith, W., Sandwell, D., 1997. Global sea floor topography from satellite altimetry and ship depth soundings. Science 277 (5334), 1956 – 1962.

Soares, P., Cardoso, R., Miranda, P., Medeiros, J., Belo-Pereira, M., Espirito-Santo, F., 2012. WRF high resolution dynamical downscaling of ERA-Interim for Portugal. Climate Dynamics 110.

Somavilla, R., González-Pola, C., Rodriguez, C., Josey, S. A., Sánchez, R. F., Lavín, A., 2009. Large changes in the hydrographic structure of the Bay of Biscay after the extreme mixing of winter 2005. Journal of Geophysical Research 114, 1–14.

Taylor, A., 2001. Summarizing multiple aspects of model performance in a single diagram. Journal of Geophysical Research 106, 7183–7192.

Torres, R., Barton, E., 2006. Onset and development of the Iberian poleward flow along the Galician coast. Continental Shelf Research 26, 1134–1153.

Vallis, G., 2006. Atmospheric and Oceanic Fluid Dynamics - Fundamentals and Large-Scale Circulation. Cambridge University Press.

Wilkin, J. L., 2006. The Summertime Heat Budget and Circulation of Southeast New England Shelf Waters. Journal of Physical Oceanography 36, 1997–2011.